BRNO UNIVERSITY OF TECHNOLOGY

VYSOKÉ UČENÍ TECHNICKÉ V BRNĚ

FACULTY OF ELECTRICAL ENGINEERING AND COMMUNICATION

FAKULTA ELEKTROTECHNIKY
A KOMUNIKAČNÍCH TECHNOLOGIÍ

DEPARTMENT OF ELECTRICAL POWER ENGINEERING

ÚSTAV ELEKTROENERGETIKY

ACCIDENT TOLERANT FUEL SIMULATION LOADED IN ADVANCED NUCLEAR REACTOR DURING SEVERE ACCIDENT CONDITIONS

SIMULACE ACCIDENT TOLERANT FUEL V POKROČILÉM JADERNÉM REAKTORU BĚHEM TĚŽKÉ HAVARIE

MASTER'S THESIS

DIPLOMOVÁ PRÁCE

AUTHOR AUTOR PRÁCE	Bc. Lukáš Hamřík
SUPERVISOR VEDOUCÍ PRÁCE	Ing. Peter Mičian

BRNO 2024

BRNO UNIVERSITY OF TECHNOLOGY
FACULTY OF ELECTRICAL ENGINEERING AND COMMUNICATION

Master's Thesis

Master's study program **Electrical Power Engineering**

Department of Electrical Power Engineering

Student: Bc. Lukáš Hamřík ***ID:*** 211108

Year of study: 2 ***Academic year:*** 2023/24

TITLE OF THESIS:

Accident Tolerant Fuel simulation loaded in advanced nuclear reactor during severe accident conditions

INSTRUCTION:

1. Review the current status of Accident Tolerant Fuel or Advanced Technology Fuel.
2. Get familiar with the possibilities of using these fuels in simulation software, especially focusing on the MELCOR software.
3. Describe the implementation of ATF fuels in MELCOR software.
4. Perform simulations of ATF fuels in an advanced nuclear reactor model during a severe accident.

RECOMMENDED LITERATURE:

recommended literature according to the instructions of the thesis supervisor

Date of project specification: 5.2.2024 ***Deadline for submission:*** 20.5.2024

Supervisor: Ing. Peter Mičian

prof. Ing. Petr Toman, Ph.D.
Chair of study program board

WARNING:

The author of the Master's Thesis claims that by creating this thesis he/she did not infringe the rights of third persons and the personal and/or property rights of third persons were not subjected to derogatory treatment. The author is fully aware of the legal consequences of an infringement of provisions as per Section 11 and following of Act No 121/2000 Coll. on copyright and rights related to copyright and on amendments to some other laws (the Copyright Act) in the wording of subsequent directives including the possible criminal consequences as resulting from provisions of Part 2, Chapter VI, Article 4 of Criminal Code 40/2009 Coll.

ABSTRACT

This diploma thesis introduces accident tolerant fuels that are considered to be a next step in increase of safety margins of nuclear power plants. In the beginning, the weaknesses of the currently operated fuel system are exposed. Accident-tolerant fuel options and their categories are described in their stages of development and faced issues before their deployment. The APR1400 plant with its accident mitigation systems is mentioned, the plant model is used to assess the impact of advanced cladding materials in a plant undergoing severe accident. The MELCOR code, capable of simulations of severe accident phenomena, is briefly introduced with its capabilities. The implementation of advanced cladding materials to MELCOR is described, altogether with simulated scenarios. In the end, the results obtained from the simulations are discussed.

KEYWORDS

Nuclear Fuel, Accident tolerant fuel, APR1400, Safety Analysis, Severe Accident, MELCOR

ABSTRAKT

Tato diplomová práce se zaměřuje na paliva se zvýšenou tolerancí vůči haváriím, jež jsou považována za další krok ke zvyšování bezpečnosti provozu jaderných elektráren. Zpočátku jsou odhaleny slabiny v současnosti provozovaného palivového systému. Jsou popsány možnosti pokročilých paliv a jejich kategorizace, v návaznosti na jejich stav vývoje a problémy, kterým čelí před svým nasazením. Je zmíněna elektrárna APR1400 se svými systémy pro zmírnění následků havárie. Model APR1400 je využit k posouzení vlivu pokročilých materiálů pokrytí při těžké havárii. Stručně jsou představeny možnosti a schopnosti kódu MELCOR, který je schopen simulovat danou problematiku těžkých havárií. Je popsána implementace pokročilých materiálů pokrytí do programu MELCOR, společně se simulovanými scénáři. Na závěr jsou diskutovány výsledky získané ze simulací.

KLÍČOVÁ SLOVA

Jaderné palivo, Palivo se zvýšenou odolností vůči haváriím, APR1400, Bezpečnostní analýzy, Těžká havárie, MELCOR

ROZŠÍŘENÝ ABSTRAKT

Obavy z možných jaderných havárií s rozsáhlými důsledky pro okolí jsou jedním z faktorů zásadně ovlivňující jadernou energetiku i přestože riziko havárií s rozsáhlými důsledky je nízké. Po havárii ve Fukušimě v roce 2011 došlo ke zvýšení pozornosti právě vůči pokročilým palivům se zvýšenou tolerancí vůči nehodám, které by měly zvýšit bezpečnostní rezervy provozovaných i budoucích elektráren. Tím by mělo dojít i ke snížení rizik při těžkých haváriích, při kterých dochází k tavení aktivní zóny a případnému uvolnění radioaktivních látek do okolí.

Pokrytí paliva je důležitým prvkem palivových souborů, sloužící k ochraně paliva před prostředím chladiva a zároveň i jako jedna z bariér před únikem štěpných produktů při provozních a havariních stavech. Pokrytí slouží i jako mechanická podpora pro palivové peletky uvnitř palivových proutků. V dnešní době výhradně užívané zirkoniové slitiny mají omezené schopnosti zvládat havarijní stavy. Pokročilé typy pokrytí uvažují využití materiálů vykazujících nadstandartní vlastnosti při havarijních podmínkách jako jsou vylepšená kinetika oxidace či množství uvolněného vodíku v důsledku oxidace.

V současnosti rozlišujeme tři kategorie pokročilých paliv: paliva s vysokou tepelnou vodivostí, pokročilé materiály pokrytí a ochranné vrstvy pokrytí. Výzkum pokročilých materiálů pokrytí významně postoupil, avšak stále nejsou plně známy vlastnosti a chování materiálů po dlouhodobém vystavení vysokoenergetickému záření, či kinetika oxidace v prostředí s přítomností páry a vzduchu.

V rámci této práce byly vybrány dva pokročilé materiály pokrytí, slitina FeCrAl a keramický karbid křemíku. Chování těchto materiálů bylo ověřeno pomocí simulačního softwaru MELCOR, který umožňuje analýzu chování modelu jaderného zařízení při těžkých haváriích s tavením paliva. Jako modelové elektrárny bylo využito pokročilého jaderného reaktoru APR1400, který je dostupný na Ústavu elektroenergetiky FEKT VUT v Brně. Ne všechny materiálové vlastnosti jsou dostupné nebo známé, proto byly estimovány na základě vlastností podobných materiálů. V důsledku těchto estimací nemusí výsledky přímo odpovídat, ovšem mohou poskytnout s určitým odstupem odhad jak by se dané materiály mohly chovat v simulovaných scénářích. V rámci práce byly simulovány tři scénáře: nehoda se ztrátou chladiva, ztráta veškerého napájení a snénář se ztrátou vnějšího napájení a záložních střídavých zdrojů. Všechny scénaře byly nastaveny tak, aby došlo ke stoprocentnímu poškození aktivní zóny a následné penetraci reaktorové nádoby roztaveným koriem.

Ve všech scénařích došlo k výraznému snížení produkce vodíku a oxidačního tepla při využití pokročilých materiálu pokrytí díky jejich pomalejší oxidační kinetice. Nehoda se ztrátou chladiva byla využita pro studii citlivosti v návaznosti na složení vytvořených oxidů na povrchu slitiny FeCrAl při oxidaci parou. Složení oxidů ovlivňuje množství vyprodukovaného tepla a vodíku při oxidaci a zásadním

způsobem i ovlivňuje čas do selhání pokrytí. Při oxidaci FeCrAl slitiny by mělo docházet k formování vrstev jednotlivých oxidů, tyto fyzikální procesy není možné v MELCORu přímo napodobit, jelikož MELCOR uvažuje formování tzv. generického oxidu, jež se skládá ze všech jednotlivých oxidů. V návaznosti na tuto skutečnost by mohla být ovlivněna přesnost simulací a získaných výsledků.

Ve scénáři se ztrátou veškerého napájení došlo k zásadnímu navýšení času do selhání pokrytí při využití karbidu křemíku ze 2,5 na 9 hodin oproti zirkoniové slitině. Při blackoutu se ztrátou vnějšího napájení a záložních střídavých zdrojů došlo k prodloužení tohoto času ze 12 hodin u zirkoniové slitiny na 19,3 hodin u karbidu křemíku. V těchto scénařích je možné pozorovat zásádní vliv tepelné vodivosti a vysokého bodu tání právě u karbidu křemíku.

Oba simulováné materiály mají potenciál zvýšit bezpečností rezervy co se týče jejich oxidačni kinetiky a produkovaného množství vodíku. Nižší teplota tání FeCrAl slitiny má za následek dřivější selhání pokrytí, ačkoliv oxidy tvořené na povrchu mají zásadní vliv na toto selhání. Tvorba oxidů hliníku a chromu na povrchu těchto slitin je jedním z hlavním ochranných mechanismů, proto je i jejich další výzkum velmi žadoucí, a to pro plné pochopení mechanismu této ochrany a jejich vlivu na degradaci materiálů a chování při těžkých haváriích. Karbid křemíku demonstruje vysokou tepelnou vodivost a teplotu tání při zvládání těžké havárie. Design, který byl v rámci této práce uvažován jako jednolitý bude mít nezanedbatelný vliv na chování v průběhu simulací. Design těchto pokrytí musí být pečlivě zvážen tak, aby zůstaly zachovány tepelné vlastnosti karbidu křemíku, ale zároveň musí řešit problém s hydrotermální korozí a křehkostí materiálu vůči mechanickému namáhání.

HAMŘÍK, Lukáš. *Accident Tolerant Fuel simulation loaded in advanced nuclear reactor during severe accident conditions*. Brno: Brno University of Technology, Faculty of Electrical Engineering and Communication, Department of Electrical Power Engineering, 2024, 131 p. Master's Thesis. Advised by Ing. Peter Mičian

Author's Declaration

Author:	Bc. Lukáš Hamřík
Author's ID:	211108
Paper type:	Master's Thesis
Academic year:	2023/24
Topic:	Accident Tolerant Fuel simulation loaded in advanced nuclear reactor during severe accident conditions

I declare that I have written this paper independently, under the guidance of the advisor and using exclusively the technical references and other sources of information cited in the paper and listed in the comprehensive bibliography at the end of the paper.

As the author, I furthermore declare that, with respect to the creation of this paper, I have not infringed any copyright or violated anyone's personal and/or ownership rights. In this context, I am fully aware of the consequences of breaking Regulation § 11 of the Copyright Act No. 121/2000 Coll. of the Czech Republic, as amended, and of any breach of rights related to intellectual property or introduced within amendments to relevant Acts such as the Intellectual Property Act or the Criminal Code, Act No. 40/2009 Coll. of the Czech Republic, Section 2, Head VI, Part 4.

Brno ....

author's signature*

ACKNOWLEDGEMENT

I would like to thank my thesis supervisor Ing. Peter Mičian, for his professional guidance, consultation, patience, and suggestions for the thesis. In addition, I would like to thank doc. Ing. Karel Katovský Ph.D. for the opportunity to study abroad at KINGS in the Republic of Korea, where I obtained the necessary knowledge in accident analyses of nuclear power plants, which I had used in this thesis.

Contents

List of Figures **17**

List of Tables **19**

Introduction **21**

1 Nuclear fuel **23**

1.1 Uranium Dioxide . . . 25
1.2 Zirconium-based alloy cladding . . . 26
1.3 Advanced zirconium alloys . . . 27
1.4 Mechanical deformations . . . 32

2 Accident tolerant fuels **37**

2.1 Categorisation of Accident tolerant fuels . . . 37
2.2 New fuel materials . . . 38
  2.2.1 Uranium Diboride . . . 38
  2.2.2 Uranium Tetraboride . . . 40
  2.2.3 Uranium Nitride . . . 41
  2.2.4 Uranium Silicide . . . 41
2.3 Alternative cladding materials . . . 42
  2.3.1 FeCrAl . . . 43
  2.3.2 Silicon Carbide - SiC . . . 46
  2.3.3 Titanium Silicon Carbide - Ti_3SiC_2 . . . 49
  2.3.4 Comparison of Zirconium-based alloys with proposed materials 51
2.4 Protection coatings . . . 54
  2.4.1 FeCrAl coatings . . . 54
  2.4.2 Cr coating . . . 55
  2.4.3 Nitride protection coatings . . . 57
  2.4.4 Carbide protection coatings . . . 59
  2.4.5 MAX phase protection coatings . . . 60

3 APR1400 - Advanced Power Reactor **63**

3.1 Plant description . . . 64
3.2 Plant safety under accident conditions . . . 66
  3.2.1 Severe accident management . . . 67

4 Design Basis Accidents, Beyond Design Basis and Design Extension Conditions 69
4.1 Large Break - Loss Of Coolant Accident 71
4.2 Station Blackout 72

5 Nuclear safety analysis 75
5.1 Deterministic safety analysis - DSA 75
5.2 Probabilistic risk assessment - PRA 76
5.3 MELCOR 77

6 Simulation in MELCOR 79
6.1 Scenarios 79
6.2 Plant model 81
6.3 Advanced cladding materials implementation 83
6.3.1 Silicon Carbide 83
6.3.1.1 Oxide properties 85
6.3.2 FeCrAl 85
6.3.2.1 Oxide properties 88
6.3.3 FeCrAl with adjusted geometry 89
6.3.4 Sensitivity study on oxide formation 93

7 Simulation evaluation 95
7.1 Unmitigated LB LOCA 95
7.2 Unmitigated LB LOCA - Sensitivity study 100
7.3 Station blackout 103
7.3.1 Station blackout - total loss of power 103
7.3.2 Station blackout - loss of AC power 107

Conclusion 111

Bibliography 113

Symbols and abbreviations 127

List of Figures

1.1 PLUS7 Nuclear Fuel Assembly [1] 23
1.2 Fuel rod description in axial and radial cross sections [2] 24
1.3 Mass gain of Zr-based alloys in air at various temperatures [10] 30
1.4 Mass gain of Zr-based alloys in steam at various temperatures [17] . . 31
1.5 Strain in time due to constantly applied stress [18] 32
1.6 Creep rupture of cladding tube [19] 33
1.7 Temperature profile along the radial direction of the fuel rod [20] . . 34
1.8 Fuel pellets cracking at low burn-up [21] 34
1.9 Fuel rod deformation - bambooing [22] 35
2.1 Spark Plasma Sintering [25] 39
2.2 Heat capacity c_p dependency on temperature T 52
2.3 Thermal conductivity k_t dependency on temperature T 53
2.4 Thermal expansion coefficient α dependency on temperature T 53
2.5 FeCrAl/Mo/Zr complex microstructure [59] 55
2.6 SEM images of the microstructure of Cr coated Zr alloy after high temperature steam oxidation at 1200 °C for 0,5 h (a), 1 h (b), 2 h (c), 4 h (d), and at 1300 °C for 0,5 h (e) and 1 h (f) [66] 56
2.7 SEM scan of TiN that underwent heavy particle irradiation - RIS [76] 59
2.8 SEM scan Ti_2AlC/TiC coating after oxidation at 800 °C in steam for 250 minutes [82] 60
3.1 APR1400 plant - schematic overview of reactor coolant system and engineered safety features [84] 63
3.2 Reactor pressure vessel [83] 65
3.3 Steam generator [83] 65
3.4 In-vessel corium retention [85] 67
4.1 Impact of plant design envelope and plant states [88] 70
4.2 FLEX enhances Defence-in-Depth [91] 73
6.1 APR1400 plant nodalization - retrieved from [94] 81
6.2 Core and lower plenum nodalization - retrieved from [94] 82
6.3 Adjusted geometry of fuel rod with FeCrAl cladding; top - original dimensions, bottom - adjusted dimensions; dimensions are not proportional, in mm 92
7.1 CORE water level - unmitigated LB LOCA 95
7.2 Cladding temperature in cell 213 - unmitigated LB LOCA 96
7.3 Total cumulative heat and hydrogen produced due to in-vessel oxidation of components - unmitigated LB LOCA 97
7.4 CORE damage - unmitigated LB LOCA 98

7.5 Total cumulative heat and hydrogen produced due to in-vessel oxidation of components - unmitigated LB LOCA - sensitivity study 100
7.6 Cladding temperature in cell 213 - unmitigated LB LOCA - sensitivity study 101
7.7 CORE water level - SBO - total loss of power 103
7.8 Cladding temperature in cell 213 - SBO - total loss of power 104
7.9 Total cumulative heat and hydrogen produced due to in-vessel oxidation of components - SBO - total loss of power 105
7.10 CORE damage - SBO - total loss of power 105
7.11 CORE water level - SBO - loss of AC power 107
7.12 Cladding temperature in cell 213 - SBO - loss of AC power 108
7.13 Total cumulative heat and hydrogen produced due to in-vessel oxidation of components - SBO - loss of AC power 109
7.14 CORE damage - SBO - loss of AC power 109

List of Tables

1.1 Main alloying elements of advanced zirconium alloys and Zircaloy-4 . 28
2.1 Main alloying elements of selected FeCrAl alloys [38] 44
4.1 Safety limits for the principal design criteria of LWR [87] 69
6.1 Density of elements and weight percentage composition of C35M alloy 85
6.2 Molar weight and weight percentage composition of C35M alloy . . . 86
6.3 Weight percentage composition of oxides considered for sensitivity study 93
7.1 Results of unmitigated LB LOCA 99
7.2 Results of unmitigated LB LOCA - sensitivity study 1/2 102
7.3 Results of unmitigated LB LOCA - sensitivity study 2/2 102
7.4 Results of SBO - total loss of power 106
7.5 Results of SBO - loss of AC power 110

Introduction

Concerns about possible nuclear accidents with extensive effects outside the plant have always been one of the factors that have an impact on nuclear energy, even when the risk is low. Therefore, the development of advanced fuel designs is underway; these new designs could greatly improve the safety margins of plants in operation as well as newly build ones. Accident tolerant fuels represent a new step in nuclear safety, as they exhibit enhanced protection against severe accidents, reducing the potential for core damage and dangerous release of radioactive substances from the plant.

Fuel cladding is a crucial part of fuel assembly to protect fuel pellets against the coolant environment and chemistry and also serves as one of the barriers against radioactive release during normal operation and accident plant states. The cladding provides structural support for the fuel pellets inside the rod. The reason for the introduction of materials with enhanced protection is that zirconium-based alloys have limited capabilities to cope with conditions in the plant that are undergoing the accident scenario. Advanced cladding designs consider the usage of advanced materials and coatings that show superior properties under accident conditions, such as high thermal stability, enhanced oxidation kinetics, and improved hydrogen release and retention.

In this thesis, the main issues of the currently operating uranium dioxide - zirconium cladding fuel system are exposed. This thesis aims to provide an overview of accident tolerant fuels, their current stage of development, introduce and assess their properties. Afterwards, it focuses on the assessment of their performance in simulations. APR1400 plant and its model are described with its features that are designed for accident mitigation. The improvements in plant response by implementing advanced cladding materials during the accident scenario are verified using the MELCOR code, which is capable of analysing the phenomena of severe accidents. MELCOR was developed to perform safety analyses for light water reactor technology plants. The code can calculate the physical and chemical processes that occur during the accident, allowing assessment and verification of the behaviour of the system, including fuel melting or the interaction of molten corium. Selected advanced cladding materials were implemented into the MELCOR code and their performance has been assessed in three scenarios, each with different expected plant responses.

1 Nuclear fuel

Nuclear fuel is used in nuclear reactors to maintain a nuclear chain reaction. Fuel is loaded into the reactor in the form of fuel assemblies. The assemblies are made up of structures such as spacer grids, lower and upper guide structures, and fuel rods, shown in fig. 1.1 for the nuclear fuel PLUS7 produced by KEPCO Nuclear Fuel (KNF). The shape of the assembly is hexagonal for Russian and soviet types or square for Western reactor types. The height and number of fuel assemblies depend on the power and type of reactor.

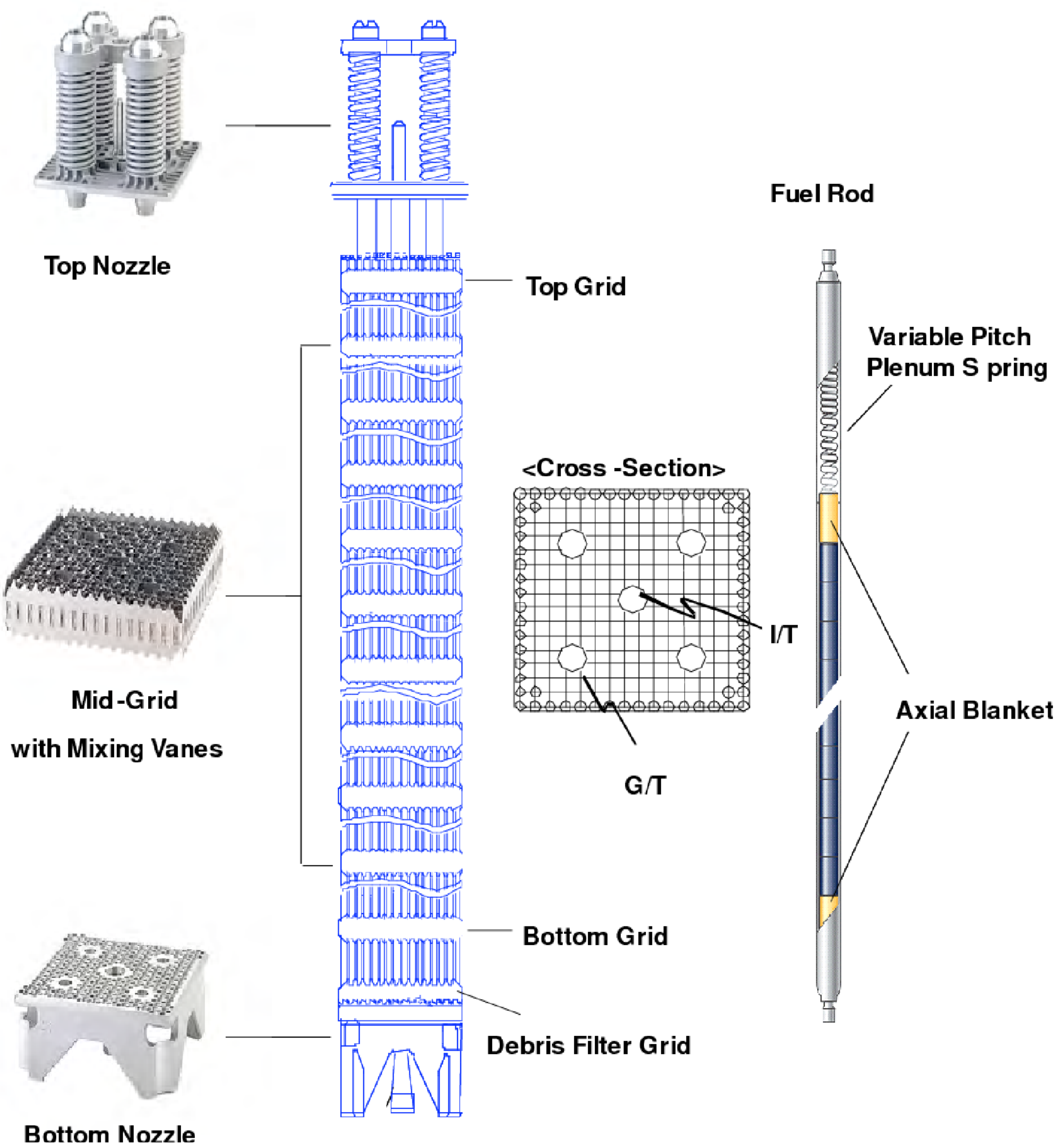
Top Nozzle
Fuel Rod
Top Grid
Variable Pitch Plenum S pring
<Cross -Section>
I/T
Mid-Grid with Mixing Vanes
Axial Blanket
G/T
Bottom Grid
Debris Filter Grid
Bottom Nozzle

Fig. 1.1: PLUS7 Nuclear Fuel Assembly [1]

The fuel rod consists of the cladding tube, typically nowadays made out of zirconium alloys, inert gas gap - helium, fuel stack - fuel pellets, end caps, and the plenum part on top, where the spring is located, shown in fig. 1.2 for both axial and radial cross sections.

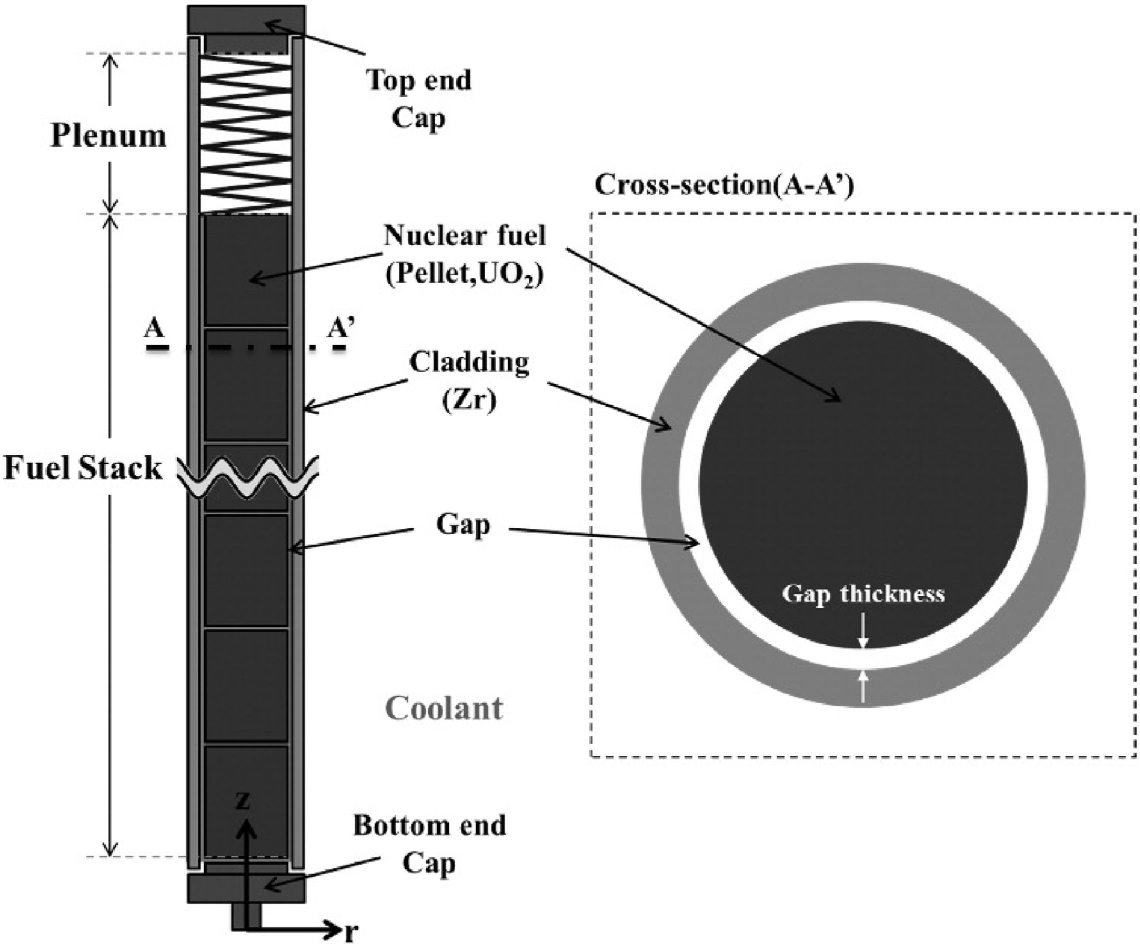
Top end Cap
Plenum
Cross-section(A-A')
Nuclear fuel (Pellet,UO_2)
A
A'
Cladding (Zr)
Fuel Stack
Gap
Gap thickness
Coolant
z
Bottom end Cap
r

Fig. 1.2: Fuel rod description in axial and radial cross sections [2]

Fuel pellets contain fissile material, most common are Uranium ^{235}U and Plutonium ^{239}Pu. Fuel pellets may be made of natural uranium and used in CANDU (Canada Deuterium Uranium) type reactors or have to be made out of uranium with higher ^{235}U isotope concentrations. Higher levels of isotopic concentration are achieved by the enrichment process. After enrichment, the uranium is converted from solid form to gaseous form and is afterwards chemically converted to uranium dioxide powder. The powder is pressed into the requested shape and measurements and sintered at high temperatures. Typical light water reactors (LWRs) use pellets enriched to various isotopic concentrations. Newer reactor types have been adopted to run on a partially or fully loaded core with Mixed Oxide fuel (MOX), which is made from previously used reprocessed fuel and contains ^{239}Pu.

The gap between the fuel pellets and the cladding tube serves many important roles. The first is a heat transfer path from fuel to cladding. The thickness of the gap has a direct influence on the gap conductivity; The thickness is affected by various factors, such as pressure, temperature, material coefficients, etc. The second is that the gap provides space for fission gases, which are released into the fuel rod during fuel burn-up. The third is that the gap provides space for the thermal expansion of the fuel during the operation; the thermal expansion coefficients are different for the cladding and for the pellet, and as the fuel reaches higher temperatures, its expansion may put stresses on the cladding from inside if there is no gap.

Cladding tubes, as mentioned before, are made mainly of zirconium alloys; In some reactor types, low alloy stainless steels can be used. Focusing on the LWR types, multiple alloys have been developed, the most common are Zircaloy-2, Zircaloy-4, M5©, E110, and ZIRLO™. Zirconium-based alloys have unique properties. They maintain mechanical properties at high temperatures. They are highly resistant to corrosive environments at elevated temperatures. Have a very low neutron absorption cross section, thus having a low impact on reactor neutronics. Lastly, they have good resistance and stability when exposed to radiation. Despite their favourable properties, these alloys have a dangerous problem. They are pretty vulnerable to oxidation by steam, as this reaction produces hydrogen in several stages when zirconium is exposed to steam [3].

1.1 Uranium Dioxide

Uranium is the most widely used fuel in modern nuclear reactors, multiple forms may be used (metallic, alloy, oxide, nitride or carbide). The commonly used form is Uranium Dioxide (UO_2) at various enrichment levels ranging from 3 to 5 % of the isotope ^{235}U [4]. The black ceramic material obtained from the conversion and sintering process has a high strength and can retain the gaseous and other radioactive products produced during the fuel burn-up [5]. Data about thermodynamic and transport properties for both solid and liquid states have been a subject of review by scientists. There are still some unknown material behaviours of UO_2 and their effects on the properties of the material, which are still under investigation, especially at elevated temperatures and oxidising environments [6]. The oxygen-metal ratio is the parameter of highest importance for the oxide fuel and determines how the fuel will behave in the core if loaded. Any deviations from the typical stoichiometric composition $UO_{2.00}$ have an impact on the fuel properties, eg. thermal diffusivity, conductivity, melting point, and chemical interactions with the cladding, consequentially affecting the fuel burn-up. Research (4) is oriented on the differences in properties based on the deviation from stoichiometric composition. The results show that the thermal diffusivity and conductivity decrease as the deviation increases, up to about 50 % for $UO_{2.033}$ compared to the stoichiometric UO_2. The equation of thermal conductivity dependent on stoichiometric coefficient and temperature for solid state is in eq. (1.1) for 95 % dense UO_2 pellet.

$$\begin{aligned} k_T = & \frac{1}{\left(4{,}627 + 0{,}55 \cdot x^{\frac{1}{2}}\right) \cdot 10^{-2} + \left(2{,}120 + 3{,}3 \cdot x\right) \cdot 10^{-4} \cdot T} \\ & + \frac{6400 \cdot 1000^{\frac{5}{2}}}{T^{\frac{5}{2}}} \cdot \exp - \frac{16350}{T}, \end{aligned} \tag{1.1}$$

where k_T is thermal conductivity (W/m.K), x is the deviation from stoichiometric coefficient (1.2), and T (K) is temperature.

$$x = \frac{O}{U} - 2, \tag{1.2}$$

where the ratio $\frac{O}{U}$ is the ratio of stoichiometric coefficients in the compound of oxygen and uranium respectively [7]. The density of UO2 at 273 K is 10,97 kg/m^3. The density value is generally reflected for 100 % dense fuel, without porosities or trapped gases. Commercial fuels are mainly within 94 - 96 % dense UO2 in a non-irradiated state. The density of fuel changes depending on temperature, burn-up level, and build-up of fission products in the fuel matrix. Maximum fuel density typically occurs between 5000 to 15000 MWd/MT burn-up; afterwards, the fuel density decreases as the burn-up increases, as the fuel swells because of the production of fission products. Temperature dependence of density could be calculated by eq. (1.3).

$$\rho\left(T\right) = 8860 - 0.9285 \cdot \left(T - 3120\right), \tag{1.3}$$

where ρ is density and T (K) is temperature [8]. The melting point of UO_2 is 3120 K. And it was determined at atmospheric pressure [9].

1.2 Zirconium-based alloy cladding

Zirconium alloys are used in the chemical and nuclear industry due to their superior mechanical and corrosion properties under normal operation conditions and have low neutron absorption cross-section. At elevated temperatures, over 1000 K, during hypothetical scenarios, oxidation is accelerated and degradation progresses faster. The typical atmosphere during the accident scenario is steam. Zirconium alloys are subjected to steam oxidation, in eq. (1.4). During this phenomenon, hydrogen and a substantial amount of heat are produced, the amount of both depends on the temperature, increasing as the temperature increases [10].

$$Zr + 2H_2O \rightarrow ZrO_2 + 2H_2 + HEAT \tag{1.4}$$

Considering the non-alloyed zirconium, at the initial stages of production by the van Arkel process, the poor corrosion resistance accounted to the stray impurities in the material. However, later it was found that purity improvements have not eliminated the issue. The oxidation rate of zirconium varies significantly depending on the grain orientation during the growth of thin oxide films. As oxidation progresses and the layer thickens, the oxidation growth rate on each grain differs and applies severe stresses to the grain boundaries, leading to cracking and separation of the oxide. As the oxide layer cracks and separates, the grains are not coated by this layer, and the grain is further oxidised. Locations with thick oxide layers were observed on grains that have low oxidation rates. Ridges of similarly cracked thick layers formed along the grains' boundaries, separating these slowly oxidising grains. In the oxygen atmosphere, these defects had only a little impact on the rate of oxidation, even though they led to a linear growth rate. In a high-temperature high-pressure environment of steam, the differences in the oxidation rate resulted in flaking of the oxide. In high-temperature water, such an effect led to the breaking-off of the oxide.

These issues were resolved by alloying zirconium with transition metals such as chromium, iron, and nickel, which are insoluble in the zirconium matrix and appear as particles of intermetallic phases. Tin is alloyed to neglect the effects of nitrogen impurities [11]. The alloys formed were named Zircaloy-2 and Zircaloy-4 and had a more uniform thick oxide layer that was not subjected to early flaking and breaking-off. The intermetallic phase particles have caused an accelerated growth of slowly oxidising grains, resulting in a more uniform layer, with less locally stressed regions on the grain boundaries [12]. But alloying of this kind did not eliminate regional corrosion effects in high-pressure and high-temperature steam [13].

1.3 Advanced zirconium alloys

Nowadays, zirconium alloys with Niobium (Nb) alloying are used. The most notable for use in pressurised water reactors (PWR) are Zr-1Nb alloy M5© developed by AREVA and Zr-1Nb-1Sn alloy ZIRLO™ by Westinghouse. The composition of the cladding alloys is shown in tab. 1.1. The M5© alloy is used for fuel rod cladding and structure components (grids and guide tubes) in all AREVA PWR reactor designs. It contains negligible tin (Sn) alloying, the microstructure is fully re-crystallized annealed and has controlled contents level of oxygen, iron, and sulphur. Compared to Zircaloy-4, the alloy has significantly improved in-core corrosion resistance and

Tab. 1.1: Main alloying elements of advanced zirconium alloys and Zircaloy-4

Alloying element in wt.%	Zircaloy-4	M5©	ZIRLO™
Niobium (Nb)	-	1	1
Tin (Sn)	1,5	0,01	1
Iron (Fe)	0,2	0,05	0,11
Chromium (Cr)	0,1	0,015	<0,11

hydrogen pick-up rates. Induced irradiation swelling and creep behaviour are reduced and allowed to be better controlled. The properties of M5© allow for higher burn-up and up-rates, and thus the alloy is suitable for load-following operation and allows for a longer period between refuelling. The density of M5© is in most simulation codes estimated at 6500 kg.m^{-3}, and is based on the modelling approach used by Framatome in the COPERNIC code. The melting temperature is assumed to be 2133.15 K or 2128.15 K, depending on the level of conservatism of the actual analysis and the analysis code used. Mostly, the lower value of melting temperature would be chosen. ZIRLO™ is low tin (Sb) and niobium (Nb) alloyed, and the microstructure is cold-worked and annealed to stress relief [14]. The thermal conductivity correlation may be applied as the correlation for Zircaloy, and it is believed that it could be applied for Zircaloy-2, Zircaloy-4, ZIRLO™ and as well for M5©. The following equation (1.5) is for the thermal conductivity of Zircaloy below temperatures of 2098 K.

$$k_t = 7,51 + 2,09 \cdot 10^{-2} \cdot T - 1,45 \cdot 10^{-5} \cdot T^2 + 7,67 \cdot 10^{-9} \cdot T^3, \tag{1.5}$$

where k_t is thermal conductivity (W/m.K), T (K) is the temperature[15]. Above a temperature of 2098 K, a single value of 36 W/m.K is assumed. The report approved by the United States Nuclear Regulatory Commission (US NRC) of AREVA considers the eq. (1.6) for the RELAP5 code and is deemed adequate [16].

$$k_t = 8,6383 \cdot \exp(0,0007 \cdot T), \tag{1.6}$$

The correlation for heat capacity is based on experimental data from and is applicable again for Zircaloy-2, Zircaloy-4, ZIRLO™ and as M5©. As dependency is complex and a single correlation is not adequate, the multiple equation approach is applied in various temperature ranges and is shown in equations (1.7) to (1.12).

$$
\begin{aligned}
c_p &= 0,1147 \cdot T + 252,55 & T &< 960,122\text{K}, & (1.7)\\
&= 1,9014 \cdot T - 1463,1 & 960,122\text{K} \leq T &< 1017,6\text{K}, & (1.8)\\
&= 0,5527 \cdot T - 90,68 & 1017,6\text{K} \leq T &< 1107,8\text{K}, & (1.9)\\
&= 1,5837 \cdot T - 1232 & 1107,8\text{K} \leq T &< 1153,1\text{K}, & (1.10)\\
&= -1,8617 \cdot T + 2740,9 & 1153,1\text{K} \leq T &< 1278,2\text{K}, & (1.11)\\
&= 356 & T &\geq 1278,2\text{K}, & (1.12)
\end{aligned}
$$

where c_p is specific heat at constant pressure (J/kg.K) at temperature T (K) [15].

The alloys have optimised oxidation kinetics and corrosion behaviour under operational conditions and were also tested by manufacturers under conditions of loss of coolant (LOCA) and reactivity initiated (RIA) accidents. Although data on oxidation behaviour under accident scenarios are limited, most research is focused on oxidation in a steam environment. It is not possible to neglect the impact of air, which may appear in the reactor coolant after the shutdown with an open reactor coolant system (RCS). The second possible scenario is air oxidation of the outer core regions after the failure of a reactor pressure vessel (RPV) in the late phase of severe accidents. The release of heat during air oxidation is higher by 80 % compared to the steam environment, having a greater impact on the accident scenario. As a result of the nitrogen in the air, oxidation of this kind is faster as a result of the formation of nitrides.

The initial kinetics in air of Zircaloy-4, M5© and ZIRLO™ is parabolic, after which, a transition to much faster linear kinetics occurs. After the transition, the formation of a very porous non-protecting oxide layer happens, allowing air diffusion at oxide-metal boundaries. The pre-transition phase is comparable to that of all alloys; however, after the transition, the kinetics varies, mainly at the time of transition. M5© alloy shows the lowest vulnerability to breakaway, thus having the lowest long-term oxidation up to 1000 °C. ZIRLO™ is vulnerable to nitrogen and has the fastest oxidation kinetics in most temperature ranges in the breakaway regime. Even up to 500 % mass gains were recorded below 1300 K. No transition occurs at higher temperatures, and only small changes in oxidation kinetics were observed. The results on isothermal oxidation in air are shown in fig. 1.3 [10].

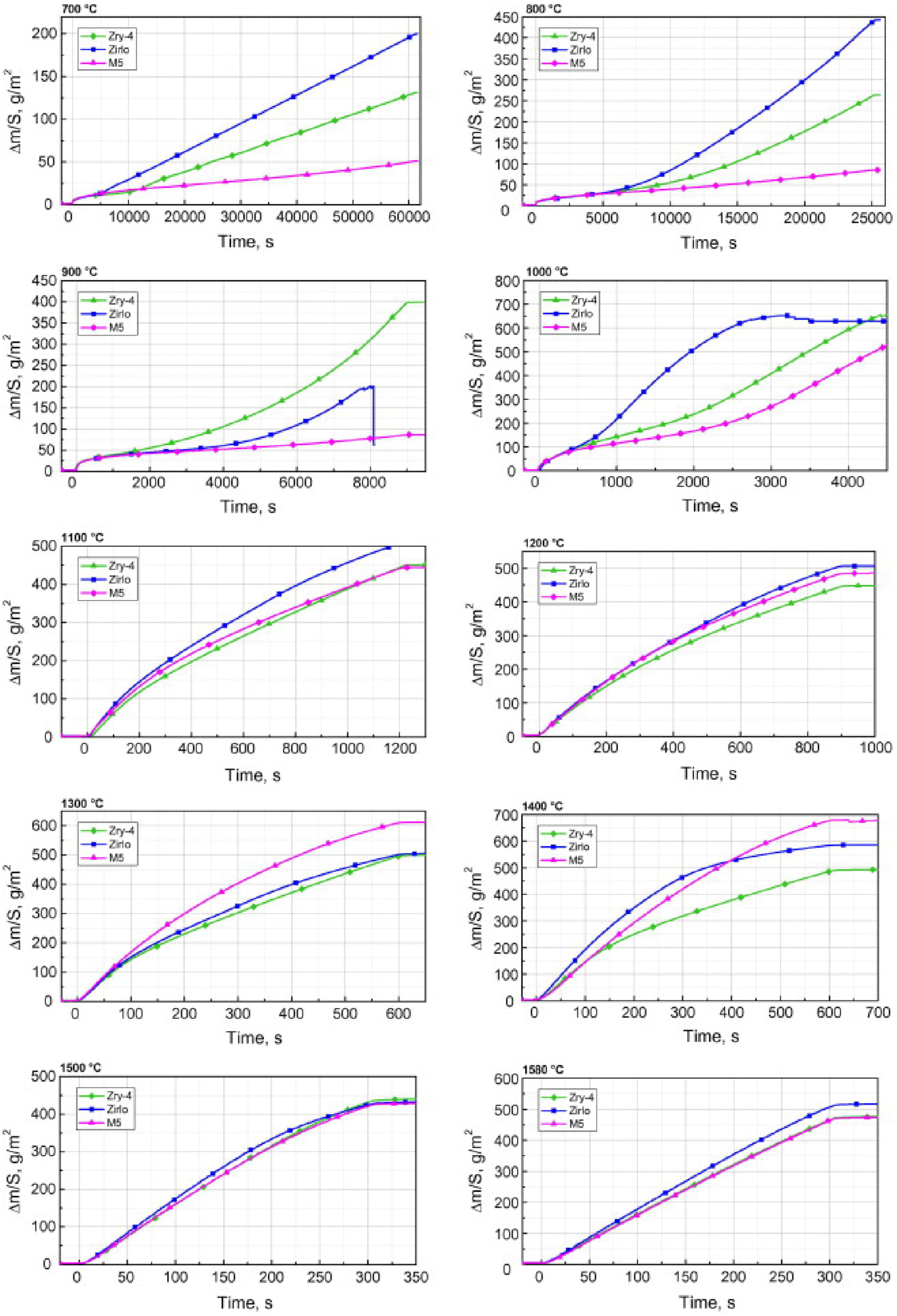

Fig. 1.3: Mass gain of Zr-based alloys in air at various temperatures [10]

In the steam environment, the oxidation kinetics is rather more complex for all alloys up to 1000 °C. The alloys show different rates of oxidation at various temperatures; for example, ZIRLO™ has the highest oxidation rate at the lowest temperatures and the oxidation rate is one of the slowest at temperatures of 1100 and 1200 °C. ZIRLO™ behaves more similarly to Zircaloy-4 at lower temperatures, as the breakaway plays a crucial role in kinetics, and at higher temperatures it behaves correspondingly to the alloy M5©. The oxidation kinetics at various temperatures are shown in fig. 1.4 [17].

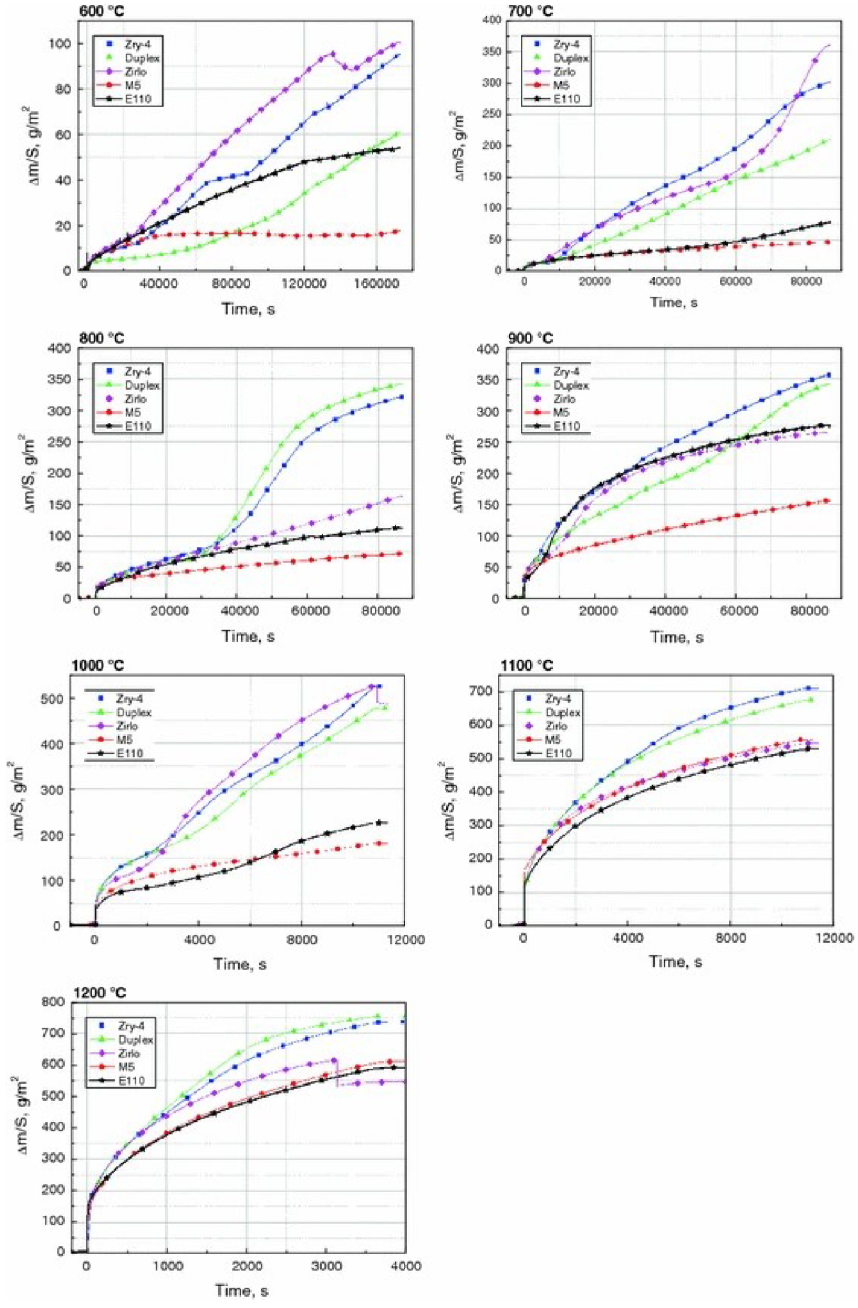

Fig. 1.4: Mass gain of Zr-based alloys in steam at various temperatures [17]

1.4 Mechanical deformations

Fuel materials are under operational conditions and in storage exposed to complex thermomechanical stresses, resulting in multiple forms of deformation such as swelling, creep, fuel pellet-cladding interaction (PCI) and cracking. The mechanical responses of the fuel are affected by the heterogeneous microstructure and are also dependent on the operating temperature and mechanical loading. During operation, fuel chemical composition and the microstructure are strongly affected by temperature gradients, irradiation, transmutation, and fission product build-up. These processes impact the fuel chemistry (electron excitation affecting the chemical bonds, transmutation affecting the composition), thermomechanical properties (irradiation creep, fuel cracking), and the fuel microstructure (induced atomic displacements by fission products and neutrons, irradiation changing and damaging the microstructure).

Creep is defined as slow irreversible deformation by stresses, the value of such stresses is below the yield strength and may be of various causes like mechanical, thermal, or irradiation. It is not a plastic deformation, as that is an instant process. Thermal and irradiation creep result in dimensional changes of the fuel element, pellet, and lead to severe deformation or rupture of the fuel rods and may lead to abnormalities in the reactor core or even accidents. This issue can even occur during long-time storage due to the increase in fission gas products; for example, the pressure in the fuel rod loaded with UO_2 can increase by 1 MPa in 100 years. This shows that the temperature range and the time frame to consider are rather large; that is why creep has to be appropriately addressed. As creep is a long-term process, the progression can be divided into three stages: the primary creep is a typical high-amplitude plastic deformation at the initial moment while the strain gradually decreases afterward, the secondary stage is where the strain rate is linear, the tertiary stage is characteristic by the rapid increase in strain rate, resulting in strong material degradation and leads to its failure, in fig. 1.5.

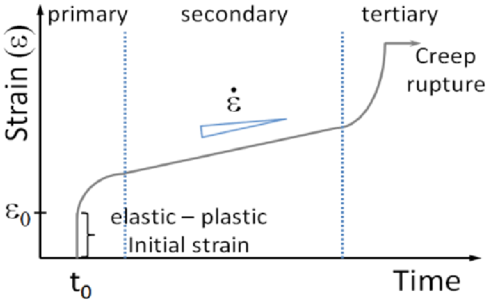

Fig. 1.5: Strain in time due to constantly applied stress [18]

The creep is influenced by multiple factors. The stoichiometry of UO_2 has an impact on the creep activation energy. Excess oxygen atoms dramatically increase the plastic deformation of UO_2 and thus increase the creep rate. Another impact may be from the grain size; it is believed that as they are larger, the creep rate increases, but any relevant mechanisms are yet to be determined. The density also has an impact as the porosity rate increases and the pellet becomes less dense. The effects of pore shapes and porosity self-healing must be quantified. Several researches have shown that creep appears even at lower temperatures under irradiation, and some have shown that the creep decreases as the irradiation by heavy ions increases. Research even though older ones on spent fuel show that creep rate increases with increasing burn-up. Fission products, as isolated defects, reduce fuel creep. The creep and the resulting rupture are also applicable to the cladding tubes, as shown in fig. 1.8.

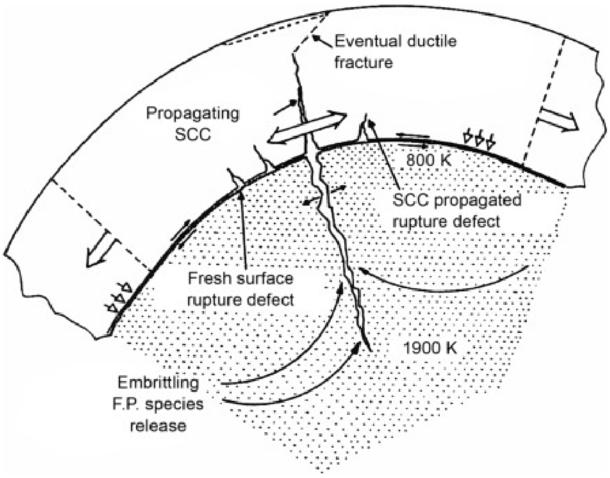
Eventual ductile fracture
Propagating SCC
800 K
SCC propagated rupture defect
Fresh surface rupture defect
1900 K
Embrittling F.P. species release

Fig. 1.6: Creep rupture of cladding tube [19]

Calculations, assumptions and estimations of dimensional changes are important to predict the behaviour and mechanical performance during irradiation. Swelling is caused mainly by the alternation of heavy-metal atoms by fission product atoms. Most of the fission products are of solid phase, and their impact on swelling is negligible; however, the gaseous fission products such as Krypton and Xenon have to be considered on their own. They usually merge into bubbles within the fuel pellets, because their solubility is very low, resulting in a significant contribution to fuel pellet swelling. The swelling of the fuel pellets and its results are shown in 1.9.

If the nuclear fuel cracks, the fission products could be released from the fuel matrix, the second impact is on thermal conductivity under all operating conditions and long-term storage. Developed cracks increase the surface area, thus increasing the rate of release of fission products, affecting the thermal conductivity conditions.

The cracking of the fuel is caused mainly by severe stresses in the fuel pellet due to a large radial temperature gradient (hundreds of Kelvin per centimetre), shown in fig. 1.7, between the centre line of the fuel pellet and the outer edge.

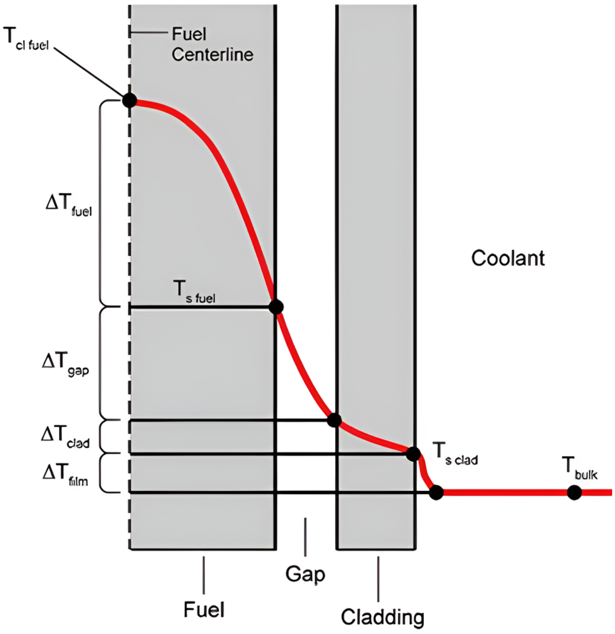
$T_{cl\ fuel}$
Fuel Centerline
ΔT_{fuel}
$T_{s\ fuel}$
Coolant
ΔT_{gap}
ΔT_{clad}
ΔT_{film}
$T_{s\ clad}$
T_{bulk}
Gap
Fuel
Cladding

Fig. 1.7: Temperature profile along the radial direction of the fuel rod [20]

Such elevated gradients are caused by a sudden increase in fuel rod power. Cracking develops before any significant swelling or creep can occur. Cracks may occur in both the axial and radial directions of the axis. Pellets may fragment into smaller parts due to cracking under nominal operation. During the transient scenarios, another set of cracks may appear, further damaging the fuel pellet. The tensile stresses are induced by the parabolic temperature gradient mostly in the outer region, and the fuel is more brittle there. In the inner region, the stresses are compressive. The severity of fuel cracks is shown in fig. 1.8.

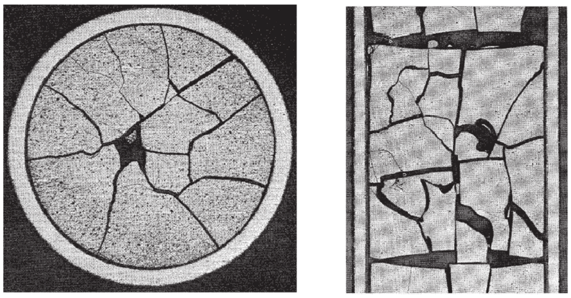

Fig. 1.8: Fuel pellets cracking at low burn-up [21]

The gas gap in the fuel rod offers space for radial thermal expansion and fuel pellet swelling during operation. Pellet cladding interaction (PCI) is a common fuel failure mechanism induced by fission products and related corrosion cracking of the cladding (SCC). The cladding is subjected to differential pressures between the coolant and the gas, compressing the cladding. The gap closes as the burn-up increases, the cladding creeps, and the fuel pellets swell as a result of the fission products. The pellets are slowly taking the shape of an hourglass. The first contact with the cladding with fuel pellets is located at the pellet-pellet interface, since the gap is the smallest there. The cladding tube will deform in response to the stresses put on the tube by the pellets, eventually copying the shape of swollen pellets - resulting in primary ridges. This phenomenon is referred to as bambooing. If power ramps occur as there are already primary ridges, the stresses caused by increased power may induce secondary ridges. The bambooing process is shown in fig. 1.9 [18].

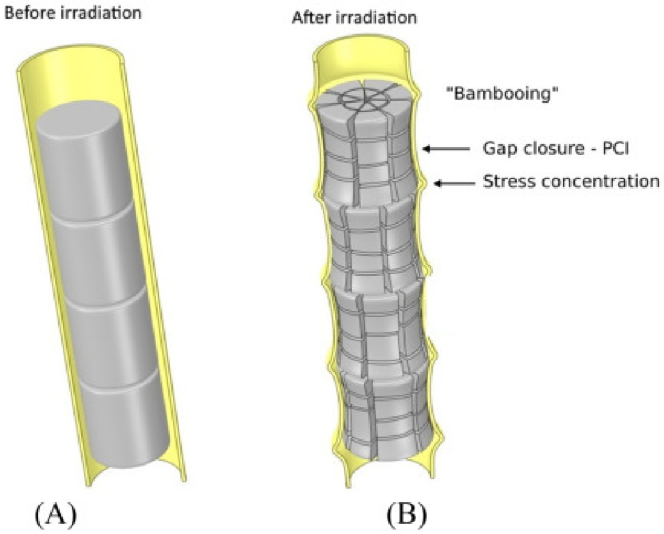

Fig. 1.9: Fuel rod deformation - bambooing [22]

2 Accident tolerant fuels

Accident tolerant fuels or Advanced technology fuels are currently the main area of focus for research and development in the area of nuclear industry, particularly for the development and advancement of light water reactors. Since the events in the Three Mile Island and Fukushima-Daichi nuclear power plants, research is focused on how to prevent these kinds of events in the future, mainly by incorporating passive and active safety features that can mitigate design basis accidents, postulated events or events which can have an impact on the nuclear power plant from outside. The probability that these events occur may be low but is never a zero.

Fuel is protected by a cladding from contact with water and steam. Steam and air oxidation of the cladding may happen while producing hydrogen. The accumulation of hydrogen in the primary circuit and containment can lead to hydrogen explosion and fatal consequences, such as the breach of the containment and the release of radioactive materials in the atmosphere. Next, of the fatal consequences can be fuel meltdown, and the creation of corium, which contains molten core and structure materials, fuel and steel melted in one complex structure, which has a form named an uncool-able shape. As the name suggests, this structure cannot be properly cooled by coolant because the surface area is too low to properly cool it down.

To prevent or mitigate the consequences, accident tolerant fuels were developed in many forms, such as totally new fuels, or by modifications to current fuel types by alternating the cladding materials and introducing coatings for the cladding to limit hydrogen generation. Due to the extreme conditions which they can face in nuclear reactors, these materials must have low thermal expansion coefficients, high thermal conductivity, high melting point, and high mechanical and chemical resistances; those are only the ones of many properties needed for considering, incorporating, and using those materials in accident tolerant fuels. These materials can be in the form of pure metals (Niobium, Molybdenum, Chromium), alloys (Iron, Nickel, Molybdenum based alloys), nitrides (Titanium, Chromium nitrides) or carbides (Zirconium, Silicon, Titanium carbides) for cladding or coating, or fuel pellets can be made of different compounds like uranium diboride UB_2 and uranium tetraboride UB_4, today almost only uranium dioxide UO_2 is used. Fuel pellets can even be coated separately in several protection layers on their own and can come down in various shapes, like DISO, TRISO or QUADRISO fuels.

2.1 Categorisation of Accident tolerant fuels

During decades of research and development of accident tolerant fuels, many approaches were designed, each with its advantages and disadvantages. The main concerns were focused on how to protect, limit, or even completely replace zirconium-based alloys (Zircaloy 2, Zircaloy 4, M5) that are nowadays used as cladding materials for nuclear fuel [3].

There are studies and experiments to limit the use of zirconium-based alloys as cladding materials or to coat them with protection layers. Research is not focused only on the development of better materials for cladding or protective coating layers; in addition, researchers are focused on high thermal conductivity fuels and composites to provide alternatives to UO_2 based fuel, commonly used nowadays.

Replacing or creating composites with UO_2 can lead to better fuel economics, such as a longer operating duration between refuelling, due to the higher uranium density in these compounds and still having high melting point temperatures and high resistance to oxidation. The main issue of UO_2 is its poor thermal conductivity. Thermal conductivity is an important property of fuel material, as it defines the centre-line temperature of fuel. Fukushima-Daichi accident has helped to promote the importance of enhanced thermal conductivity of fuel in reactors that are undergoing accident scenarios.

2.2 New fuel materials

In [23] two ways of creating new forms of fuel are proposed. One of the exceptional ways to completely redesign current fuel types is the introduction of new uranium-based compounds to replace UO_2, such as uranium nitride UN, uranium borides UB, or uranium silicides USi. Many studies focus on compounds based on uranium and boride such as UB_2 and UB_4. The second possible option is to create composite materials from the compounds mentioned before and UO_2. Those compounds have higher thermal conductivity than only pure UO_2. More possible alternatives are being investigated, not just boride-uranium composites, namely, the uranium nitride and the uranium silicide.

2.2.1 Uranium Diboride

Is a refractory ceramic material with better thermal properties than UO_2. According to [24] it has a higher uranium density $11,68$ g.cm^{-3} compared to $9,67$ g.cm^{-3} of UO_2. Has a much higher thermal conductivity, resulting in a lower temperature difference and a flatter temperature profile between the centre line and edge of the fuel pellet during normal operating conditions. These properties allow for the reduction of temperature-driven release of fission products, reduction in internal stress in fuel pellets due to thermal expansion, reduction of thermal energy accumulation, and a significant increase in thermal margin to centre-line melting. The higher density allows for loading the core of a nuclear reactor with more fissile material for a given core layout, thus prolonging the period for refuelling the reactor with new, fresh fuel.

Boron ^{10}B is known for its high thermal neutron absorption coefficient, it is used for the control of reactivity in nuclear reactors in the form of soluble boric acid or in the form of burnable absorbers. However, boron ^{11}B has a low thermal neutron absorption coefficient. Therefore, by adjusting the ratio of these, it is possible to create an integrated burnable absorber directly incorporated into fuel pellets. This solution offers better control of the burn-up cycle, while increasing thermal conductivity compared to other burnable absorber options and maintaining a high melting point [23]. In this study, it was used to create a composite with UO_2 with different percentages of weight fractions.

One possible way, still in the experimental stage, of making UB_2 is by utilising carbo / borothermic reduction synthesis, which has already been used for the synthesis of diboride ceramics on an industrial scale, eg. Zirconium diboride, which is isostructural with UB_2. The advantages of such a process are that it avoids uranium metal fabrication and melting. Synthesis was initiated by mixing powders of UO_2, B_4C and carbon in the planetary mill, carbon powder was made of nuclear grade graphite. The mixture was then pressed to create a pellet and heat-treated in a vacuum furnace. This pellet was semi-sintered but was brittle [24].

Equation (2.1) shows the reaction during the heat treating process.

$$2UO_2 + B_4C + 3C \rightarrow 2UB_2 + 4CO \tag{2.1}$$

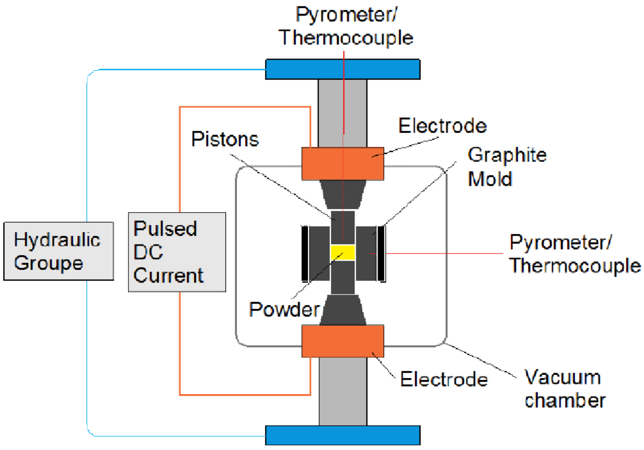

Fig. 2.1: Spark Plasma Sintering [25]

However, the majority of studies are based on possible material simulations since there are difficulties in synthesizing the materials and issues in creating dense fuel pellets. Recently, Spark Plasma Sintering (SPS) technology, schematically in fig. 2.1, was used to create such pellets that were used to measure thermophysical properties and the carbo/borothermic reduction synthesis method was used to synthesise UB_2 from UO_2 [26]. SPS technology uses axial pressure, low voltage, and high currents, generally in a simplified manner, it can be described as a modification of hot pressing, but the furnace is replaced with a mold, containing the material and is heated by the current flowing through the mold and eventually the material.

2.2.2 Uranium Tetraboride

Uranium Tetraboride is a refractory ceramic material with a high melting temperature of about 2500 K, higher than that of UB_2. Material density of $9,64$ g.cm^{-3} is about as similar to that of UO_2 [27].

Thermal conductivity is higher than that of UO_2 and lower than that of UB_2, leading to a worse temperature profile with larger temperature differences between the centre line and the edges of the fuel pellet compared to UB_2. Similarly, as with UB_2 by adjusting the ratio of ^{10}B and ^{11}B, it is possible to make an effective burnable absorber integrated into fuel [23].

As for the [23], the evaluated material is a composite of UO_2 and UB_4(UO_2-UB_4), with multiple weight fractions of boride phases. Manufacturing such a composite material is still a challenge, especially in larger quantities. For laboratory use, it was achieved to obtain it in small quantities via spark plasma sintering to evaluate its thermal properties.

Synthesis of UB_4 is possible utilising Solid-State Metathesis Reactions. The biggest advantage of this method is that it does not require high temperatures, the reaction undergoes at a temperature of about 850 degrees Celsius. The key to synthesising this material at low temperatures is to identify suitable precursors that will form ceramic material with the required properties. Equation (2.2) shows the reaction of precursors that after a heating of one day at 850 degrees Celsius in vacuum-sealed quartz tubes form UB_4. After one day, the tubes were opened and the formed materials were washed in water because $MgCl_2$ is soluble in water, it dissolves. Using powder X-ray diffraction, the final product diffraction pattern was compared with the calculated pattern [28].

$$2UCl_4 + 2MgB_4 \rightarrow UB_4 + 2MgCl_2 \tag{2.2}$$

Likewise, as for the UB_2, it is possible to use Carbo/borothermic reduction synthesis to obtain UB_4 [29].

2.2.3 Uranium Nitride

Is one of the most promising accident tolerant fuel materials, due to its outstanding material properties in comparison with UO_2 and MOX. It offers good thermal conductivity, high melting point, and low thermal expansion while having higher fissile material density and compatibility with other coolants like liquid metals or gases, so, it is possible to use this material not just in light-water cooled reactors of PWR and BWR types, but even in generation IV reactors e.g. sodium-cooled fast reactor or high-temperature gas-cooled reactor. The higher density of the fissile material allows more material to be loaded into the core of the same size, UN contains about 40% more fissile material for the same fuel enrichment as UO_2, allowing a longer fuel cycle, higher production of fissile isotopes, which leads to higher conversion ratios and possibly to higher fuel burn-up.

A disadvantage of this material is its instability and oxidation in environments containing water; the issue can be resolved by incorporating protective dopants, such as chromium, zirconium, or aluminium; the incorporation of such materials can greatly improve the resistance to oxidation [30]. Another issue is that ^{14}N has a high neutron absorption cross section, to avoid this, enrichment by ^{15} N is needed. The phenomenon of $^{14}N(n,p)$ ^{14}C reaction is also addressed by this process [31].

Mononitride uranium fuel is possible to manufacture by carbo/borothermic reduction, but despite advancements in this method, it still requires expensive infrastructure, and the material produced by such method contains high carbon and oxygen content, often resulting in contamination by impurities. Alternatively, the sol-gel method can be used. Other experimental methods such as reacting uranium carbide (UC) or uranium tetrafluoride (UF_4) with ammonia have been proposed. Although there are alternatives, synthetic routes using UO_2 or metallic uranium are feasible and well developed to be used on an industrial scale. Although extensive research has been conducted in this area, UN synthesis still poses a challenge, while bonding and reactivity between uranium and nitrogen remain largely unexplored [32].

2.2.4 Uranium Silicide

Is a candidate for the replacement of UO_2 based fuels for light water reactors, due to its high thermal conductivity, thus a reduction in centre line temperature and energy accumulation, and higher uranium density, allowing for power up or longer cycles of fuel, while maintaining enrichment levels. A disadvantage is the lower melting point temperature compared to UO_2.

The advantage of commonly used UO_2 is its thermodynamic stability at operating temperatures typical of LWR. The effects of the chemistry of LWR coolants during testing showed years of stability, further highlighting the inability of this coolant in the temperature range between 300-400℃ to oxidise or have any degradation effects on fuel pellets. Decades of operation of LWRs show the ability of UO_2 to withstand cladding failures without severe consequences. However, similar types of experiments have to be done for U_3Si_2 based fuel, to be able to compare these fuel types, further study is needed, although in some studies the coolant temperature did not exceed 200℃ and reported slight reactions only after 4 days of exposure [33][34].

The study [34] investigates the effects of coolant at elevated temperatures of about 300℃ and pressure of 100 bars on the material. A fuel pellet sample was prepared from pure metal powders using powder metallurgy, followed by pressing and sintering, achieving a theoretical density of 94- 96%. The sample was tested via static autoclave testing, to simulate the conditions in the LWR, the fuel pellet being exposed in case of cladding failure. When the desired temperature of the coolant was reached, a test was run for 48 hours. The results of the experiment showed minimal visual differences in comparison to those in the as-fabricated state and no weight difference could be determined.

2.3 Alternative cladding materials

The fuel cladding tube is a highly stressed part of the fuel rod, due to the high temperature of the fuel inside and the high pressure of the coolant and its properties outside. During normal operation, when the core cooling is sufficient, the cladding should be able to withstand such conditions. However, the temperature difference between the inner and outer edges can pose a certain level of risk, mainly due to the thermal expansion coefficient; expansion can cause unwanted stresses in the tube and can lead to deformations like twisting or bending, and even to cladding tube rupture and then to a radioactive material leak, corrosion of fuel pellets, etc. Cladding materials must have exceptional chemical and oxidation resistance to withstand elevated temperatures and the corrosiveness of the coolant environment.

Nowadays, mainly zirconium-based alloys are used because of their good corrosion and chemical resistance properties in a wide range of temperatures. The advantage of zirconium-based alloys is their low neutron absorption cross section in the thermal spectrum. The biggest disadvantage of these alloys is that zirconium reacts with steam while producing hydrogen and excess heat, and this reaction is accelerated when the temperature rises. Such a reaction is especially dangerous in a reactor that is in an accident scenario with a loss of coolant or a sudden depressurisation of the reactor coolant system.

In 2011, the Fukushima-Daichi LWR accident accelerated research programmes focused on material-based technologies, offering increased accident tolerance during abnormal operating conditions and accident scenarios. Key properties of new material technologies include enhanced reaction kinetics with steam, reduction in hydrogen production, improved cladding properties, and retention of fission products, while still having acceptable behaviour and material properties for performance under normal operation [35].

2.3.1 FeCrAl

Iron-chromium-aluminium alloys are currently in an experimental phase and are being investigated as an option for monolithic ATF cladding for light-water reactors. FeCrAl alloys are representatives of advanced alloys resistant to oxidation with chromium contents between 10 to 22 wt% and aluminium contents between 4 to 8 wt%. Alloys with chromium and aluminium content within these ranges are known to have improved oxidation resistance to steam at elevated temperatures in comparison to zirconium alloys.

Research and development of FeCrAl cladding alloys has been pioneered by Oak Ridge National Laboratory (ORNL) in the United States and is focused on wide areas, focusing on accident scenario testing, irradiation screening, safety analysis, possible fabrication methods and related studies, and integral testing, such as water loop testing. Such activities allow for the creation of a vast database of materials which provides valuable insight and scientific basis for alloy selection and production for commercial development. The goal is to deploy selected alloys as part of a Lead Fuel Rod in a Lead Test Assembly, this goal focuses primarily on the development and maturation of the cladding material while the fuel type remains unchanged, the commercial standard UO_2.

Currently, there are two generations of FeCrAl alloys, the first generation alloys were simple alloys, based typically only on Fe, Cr, Al, and Yttrium for improved oxidation resistance, for example, Kanthal APMT, Alkrothal. These alloys were not optimised for use in nuclear power applications, but their testing and evaluation set the basis for development and a close approximation of the possible composition of more complex second-generation alloys. Generation II alloys can be easily distinguished from generation I alloys, as they have optimised chemistry and microstructure. These optimised alloys have lower contents of chromium (10-13 wt%) and aluminium (4-6 wt%) and can be referred to as lean alloys, and they often have minor alloying contents of niobium and molybdenum to improve alloy overall strength at normal operating conditions. The improved strength allows for a reduction of the thickness of a cladding tube, thus reducing the neutronic penalty of

FeCrAl alloys, which is higher than that for Zr-based alloys.

Although extensive research is ongoing about how the contents and ratios of alloyed materials like Cr or Al affect material properties, not only in the non-irradiated state but even in the irradiated state. More research is needed to understand how materials behave under stress conditions, especially in the irradiated state, and to counteract and resolve issues that arise [35].

Chromium content significantly affects oxidation resistance at high temperatures by supporting the stability of Al_2O_3 oxide layer for the steam and hot water environment, but increased content of the element enhances the potential for embrittlement [36]. The aluminium content also increases resistance to oxidation through the formation of protective Al_2O_3 layer in the steam environment, however, with a higher aluminium content, the difficulty of fabricating the cladding increases [37].

The following tab. 2.1 shows the alloying content of two different FeCrAl alloys, Kanthal APMT as the representative of the first generation and the C35M alloy developed by ORNL as the representative of second generation. The difference in alloying contents is the result of significant steps in material research to improve the material properties while decreasing Cr and Al contents to improve the manufacturing possibilities. Research [39] by ORNL have resulted in given empiricial correlations for specific heat, thermal conductivity, thermal expansion coefficient and many more. Because the materials are ferritic, the magnetic contribution to the specific heat is not negligible and must be accounted for. The correlations have to be given in two separate equations to reflect the transition from ferromagnetic to paramagnetic phases; these correlations are given for temperatures below and above the Curie temperature. Curie temperature for Kanthal APMT is 852 K and for C35M is 870 K. The correlations for the specific heat of Kanthal APMT are in

Tab. 2.1: Main alloying elements of selected FeCrAl alloys [38]

Alloying element (in %)	Kanthal APMT	ORNL C35M
Iron	67,62 - 71,5	80,15
Chromium	20,5 - 23,5	13
Aluminium	5	4,5
Molybdenum	3	2
Manganese	up to 0,4	-
Silicium	up to 0,7	0,2
Carbon	0,08	-
Yttrium	-	0,15

eq. (2.3) and (2.4).

$$c_p = 2,54 \cdot T + \left(-4,311 \cdot 10^{-3}\right) \cdot T^2 + 2,982 \cdot 10^{-6} \cdot T^3 \qquad T \leq T_C, \tag{2.3}$$

$$\begin{split} c_p = 2,54 \cdot T + \left(-4,311 \cdot 10^{-3}\right) \cdot T^2 + 2,982 \cdot 10^{-6} \cdot T^3 + \\ + \frac{-5,71 \cdot 10^3}{T} + (-50,38) \cdot \ln\left(\frac{|T - T_C|}{T_C}\right) \qquad T > T_C, \end{split} \tag{2.4}$$

where c_p is specific heat (J/kg.K) at temperature T(K). Similarly, for C35M, the specific heat correlations are given in eq. (2.5) and (2.6).

$$c_p = 2,43 \cdot T + \left(-4,002 \cdot 10^{-3}\right) \cdot T^2 + 2,72 \cdot 10^{-6} \cdot T^3 \qquad T \leq T_C, \tag{2.5}$$

$$\begin{split} c_p = 1,946 \cdot T + \left(-2,002 \cdot 10^{-3}\right) \cdot T^2 + 0,698 \cdot 10^{-6} \cdot T^3 + \\ + \frac{-1,652 \cdot 10^3}{T} + (-53,93) \cdot \ln\left(\frac{|T - T_C|}{T_C}\right) \qquad T > T_C, \end{split} \tag{2.6}$$

where c_p is specific heat (J/kg.K) at temperature T(K). The correlation for thermal conductivity could be specified as a second-degree polynomial. The correlation for Kanthal APMT is in equation (2.7) and for C35M is in eq. (2.8).

$$k_t = \left(-7,223 \cdot 10^{-7}\right) \cdot T^2 + \left(-1,563 \cdot 10^{-2}\right) \cdot T + 6,569, \tag{2.7}$$

$$k_t = \left(-19,86 \cdot 10^{-7}\right) \cdot T^2 + \left(-1,537 \cdot 10^{-2}\right) \cdot T + 8,502, \tag{2.8}$$

where k_t is thermal conductivity (W/m.K), T is temperature (K). The results given from the above correlations show no specifically significant trends different from those of other high-Cr ferritic steels, and that the thermal conductivity increased with increasing temperature in the measured range of temperatures close to a monotonic increase. Studies found that the thermal expansion coefficient is not different in the rolling and transverse directions by a huge margin; thus, the measured values could be represented as mean values from both directions. At lower temperatures below 1000 K, the differences in coefficients depend on the materialistic composition of the alloys, differences becoming marginal with increasing values above 1400 K. The correlations are given by the third degree polynomial and for Kanthal APMT is in eq. (2.9) and for C35M in eq. (2.10) respectively.

$$\alpha = \left(1,771 \cdot 10^{-10}\right) \cdot T^3 + \left(9,558 \cdot 10^{-7}\right) \cdot T^2 + \left(1,937 \cdot 10^{-3}\right) \cdot T + 10,27, \tag{2.9}$$

$$\alpha = \left(9,095 \cdot 10^{-10}\right) \cdot T^3 + \left(-17,46 \cdot 10^{-7}\right) \cdot T^2 + \left(4,53 \cdot 10^{-3}\right) \cdot T + 9,81, \tag{2.10}$$

where α is coefficient of thermal expansion (10^{-6}/K), T is temperature (K). FeCrAl alloys generally form a dense layer of Al_2O_3 protective layer, such layer provides advantages like chemical stability in a water environment and slow growth. For example, for the FeCrAl alloy from generation I, particularly the Kanthal APMT, the temperature at which the oxide layer starts to form is about 700 °C. There is no point at which the oxidation begins to accelerate, as the oxidation kinetics of FeCrAl alloys follow a similar parabolic oxidation rate as zirconium-based alloys [40].

2.3.2 Silicon Carbide - SiC

Silicon carbide is a refractory ceramic material with established usage in many areas of industry, especially in environments of highly corrosive nature and in which parts have to withstand high temperatures. SiC and its composites have material properties better than those of zirconium alloys, particularly smaller neutron absorption cross section, chemical inertness, ability to withstand higher fuel burn-ups and higher temperatures, exceptional radiation resistance, lack of progressive irradiation growth, low induced activation decay heat, and show permanent stability in nuclear waste. Some critical feasibility studies are missing until progression to introduction, such as for hydrothermal corrosion, potential fission gas loss retention (cracking of material under normal operation conditions) and development of fuel performance modelling capability [41].

Two classes for potential use are proposed for SiC cladding designs, those are full ceramics in duplex (composite-monolith) or triplex (monolith-composite-monolith) structures and metal-assisted ceramics also in duplex (metal-composite) and triplex (composite-metal-composite) structures. Because the material is not in use, as it is in development, no standards have been introduced for the design or manufacturing of cladding.

Study [40] is focused on continuous SiC fibre reinforced composites with fully crystalline SiC material of nuclear grade, namely Hi-Nicalon Type S and Tyranno SA3. Fibres have similar mechanical properties, but different thermal performance.

In general, the steps in manufacturing SiC cladding tubes are as follows: SiC fibres are used to make a tube by different methods, mainly by winding and braiding, an interphase layer is then added through the CVD method, the next step is to add SiC matrix by chemical vapour infiltration, and for the last step, the environment barrier coating may be added. Each step of the process creates a part that has a different specific function. Fibres provide the best mechanical performance in an axial direction, so the volume of fibres and the way of building the composite layer have an effect on the final behaviour and performance of such made cladding. Braiding in 2 or 3 directions became popular due to its better resistance to damage.

Although SiC composites have great mechanical properties and high damage tolerance, enough bounding strength between added layers is needed, such bounding is provided by the interphase layer, and parameters of the layer such as thickness will affect the cladding behaviour.

The chemical vapour infiltration method seems to be the most stable and relatively mature technology for manufacturing long enough thin SiC tubes without many impurities on a larger scale. However, for large-scale production and for use in LWR applications, a facility needs to be built.

During normal operation in LWR, the SiC oxidation reaction occurs, independently of the water chemistry, of the free Si in the Sic matrix and progresses as follows:

$$Si + 2H_2O \rightarrow SiO_2 + 2H_2 \tag{2.11}$$

$$SiC + 2H_2O \rightarrow SiO_2 + CH_4 \tag{2.12}$$

At high temperatures and under high-pressure water, SiO_2 is unstable and dissolves into the water by the following reaction [42][43]:

$$SiO_2 + 2H_2O \rightarrow Si(OH_4) \tag{2.13}$$

If dissolved oxygen is present in the coolant at high pressure and temperature, reaction (2.14) can occur, the presence of lithium can further accelerate the corrosion [44].

$$SiC + 2O_2 + 2H_2O \rightarrow Si(OH_4) + CO_2 \tag{2.14}$$

The main oxidation agent for SiC at high temperatures is steam, oxidation of SiC by steam is a two-step process, the first step (2.15) is a silica formation on the surface of the material and is followed by its volatilization by (2.16) [45].

$$SiC + 3H_2O \rightarrow SiO_2 + 3H_2 + CO \tag{2.15}$$

$$SiO_2 + 2H_2O \rightarrow Si(OH_4) \tag{2.16}$$

Report [46] reported that UO_2 and silicon carbide underwent chemical reaction at temperatures above 1377 °C by (2.17).

$$2SiC + UO_2 \rightarrow USi_2 + 2CO \tag{2.17}$$

Thermal conductivity along the matrix thickness is a key parameter for transfer of heat generated in fuel to the coolant, higher conductivity results in a lower temperature of the fuel rod and smaller temperature gradient. Neutron irradiation influences thermal conductivity; however, there is no reliable data on the thermal conductivity of irradiated SiC tubes, and currently available data have been measured from plate specimens. Thermal conductivity correlation of CVI matrix SiC cladding with Nicalon fibres has been established in [47].

$$k_{clad} = k_{sat} \cdot \left(\frac{(d + d_0)}{d_{sat}} \right)^{-0,4}, \tag{2.18}$$

where k_{clad} is thermal conductivity; k_{sat} is thermal conductivity when the neutron fluence reaches saturation DPA, regardless of temperature set as 20 W/m.K; d is cumulative cladding neutron irradiation influence, set as 1 DPA; d_{sat} is saturation neutron influence, set as 1 DPA in [47]; d_0 is defined as:

$$d_0 = d_{sat} \cdot \left(\frac{k_{sat}}{k_T} \right)^{2,5}, \tag{2.19}$$

where k_t is the thermal conductivity of the SiC cladding tube at a particular temperature and is be specified as:

$$k_t = 8 \cdot 10^{-6} \cdot T_{clad}^2 - 0,02 \cdot T_{clad} + (k_{rt} + 26,4), \tag{2.20}$$

where k_{rt} is the thermal conductivity of the SiC at 300 K. This experiment used more of a conservative approach and in comparison with limited available data, even with estimated saturation DPA and saturation temperature, many researchers agreed with this model. In [48] saturation conductivity was experimentally determined as 10 W/m.K and was later used for the definition of thermal resistivity in ORNL report [41] of SiC cladding in an irradiated state. However, this property is material structure dependent and is not accurate, to be used in general, as it is related to structure, layer composition, etc.

As the presence of carbon interphase in SiC is negligible, the specific heat can be assumed to be that of monolithic SiC with high purity. The effects of irradiation on this parameter are also negligible; it is possible to use correlation for the specific heat from [41]:

$$c_p = 925,65 + 0,3772 \cdot T - 7,9259 \cdot 10^{-5} \cdot T^2 - \frac{3,1946 \cdot 10^7}{T^2}, \tag{2.21}$$

where c_p is specific heat (J/kg.K) at temperature T(K).

The thermal expansion coefficient is another important parameter as it defines the thermal expansion of the material, the higher the coefficient, the higher the circumferential stress of the cladding and the greater the gap between the fuel pellets and the cladding tube, thus significantly reducing the thermal performance of the fuel rod as the heat transfer from the fuel pellet to the cladding will be reduced by the increased thermal resistivity of a thicker gap.

Report [49] concluded that the thermal expansion coefficient of SiC composites is only weakly dependent on temperature and that SiC composites made from different fibre types and by different architecture methods have no significant differences and can be generally assumed as $3 \cdot 10^{-6}$ 1/K. The correlation for the thermal expansion coefficient for the SiC cladding tube is generally assumed to be the same as that for the SiC plate material with comparable microstructure and can be obtained by eq. (2.22).

$$\alpha = 0,7765 + 1,435 \cdot 10^{-2} \cdot T - 1,2209 \cdot 10^{-5} \cdot T^2 + 3,8289 \cdot 10^{-9} \cdot T^3, \qquad (2.22)$$

where α is coefficient of thermal expansion (10^{-6}/K) , T is temperature (K). SiC matrix is the first layer in contact with coolant if no environmental protective coating has been applied to the surface. According to [45] SiC is subject to dissolution phenomena under environmental conditions, similar to those found in light water reactors. Oxidation behaviour begins at the grain boundary and progresses through the surface, grains become thinner, and then they detach from the surface. A study [50] proved that such a phenomenon occurs regardless of the SiC manufacturing process. Factors affecting the corrosion process are neutron irradiation, the pH of the coolant, and the electrochemical potential, but the most important is the dissolved oxygen in the coolant. Dissolution of SiC in the coolant could cause many issues and possible consequences. Loss of cladding matrix in the long term could expose the interphase or fibre layer of the composite and lead to structural influence, namely degradation of mechanical properties. Further studies of this phenomenon are required, mainly to understand the kinetics and progression of the oxidation process, because the knowledge in this area is still limited.

2.3.3 Titanium Silicon Carbide - Ti_3SiC_2

It is a kind of material, commonly referred to as MAX phase material, which are thermodynamically stable nanolaminates. MAX phase materials combine properties of metallic and ceramic phases and have enhanced hardness, resistance to oxidation, and stability at high temperatures. Metallic phases have higher thermal conductivity and resistance to thermal shocks. Resulting in good oxidation resistance, high melting point, and high thermal conductivity in the case of thermal properties. As for mechanical properties, those materials have relatively low density, good thermal shock resistance, high elastic modulus, and damage toleration. Additionally, such material could be easily processed using machining, simplifying the production of parts in the desired shapes and sizes. One of the most described is Ti_3SiC_2, and is considered a candidate for the replacement of zirconium alloys in nuclear applications [40]. In research [51], the conducted experiment showed that Ti_3SiC_2 has a weak dependency on temperature, and in the range of temperatures between 25 to

1200 °C the following correlation (2.23)could be approximated from obtained results.

$$k_T = 38,6 - 0,0045 \cdot T, \tag{2.23}$$

where k_T is thermal conductivity (W/m.K), T is temperature (K). The thermal conductivity of Ti_3SiC_2 is higher than that of Zr alloys under normal operation conditions. Second, there is another area of possible use in nuclear engineering of Ti_3SiC_2, which could be added as a second phase to conventional UO_2 fuel pellets to improve conductivity. The other compounds proposed for application are beryllium oxide (BeO) and SiC. Although SiC may have higher thermal conductivity, irradiation impacts thermal performance because SiC develops structural defects [52]. These defects form even in Ti_3SiC_2, except that they recover at high temperatures [53].

In report [51] it is also possible to find the results of measurement of specific heat. By fitting the curve, the correlation (2.24) was determined.

$$c_p = 839,95 - \frac{83877}{T}, \tag{2.24}$$

where c_p is specific heat (J/kg.K) at temperature T(K). The oxidation in air is described by reactions (2.25)(2.26). During the reaction, a dense and adhesive coating of oxides is formed. Two layers are usually formed, the inner layer is a mixture of $Ti0_2$ and $Si0_2$, while the second formed is predominantly made up of $Ti0_2$. The layers formed protect the material from further oxidation, while the layers have a strong oxidation resistance to air on their own. The oxidation kinetics is parabolic, but the increase in the rate could be neglected for temperatures below 900 °C.

$$Ti_3SiC_2 + 5O_2 \rightarrow 3TiO_2 + SiO_2 + 2CO \tag{2.25}$$

$$Ti_3SiC_2 + 6O_2 \rightarrow 3TiO_2 + SiO_2 + 2CO_2 \tag{2.26}$$

However, the main driver of oxidation in nuclear applications has to be considered to be water, especially when concerning the fuel cladding. Research [54] conducted on the effects of hydrothermal oxidation of Ti_3SiC_2 by continuous flow of water at temperatures between 500 to 700 °C reports that the oxidation was not significant below 600 °C, but, accelerated at 700 °C, as the oxide layer on surface develops cracks. Oxidation is characterised by the following equations (2.27) (2.28) depending on the temperature.

$$Ti_3SiC_2 + 12H_2O \rightarrow 3TiO_2 + SiO_2 + 2CO_2 + 12H_2 \tag{2.27}$$

$$Ti_3SiC_2 + 9H_2O \rightarrow 3TiO_2 + SiO_2 + \frac{1}{2}CO_2 + \frac{3}{2}CH_4 + 6H_2 \tag{2.28}$$

Previously mentioned in section 2.3.2, SiO_2 layer dissolves into water and only the TiO_2 remain, resulting in lowered resistance to oxidation by hot water. When the temperature reaches approximately 700 °C, phase transformation of the oxide layer occurs, inducing tensile stress, leading to cracks in the oxide layer.

2.3.4 Comparison of Zirconium-based alloys with proposed materials

The fig. 2.2, 2.3, and 2.4 show the dependencies of thermophysical material properties of specific heat c_p (J/kg.K), thermal conductivity k_{total} (W / m K) and the coefficient of thermal expansion α (10^{-6}/K) respectively, at temperature T (K). These properties are stated in graphs without the effects of irradiation and may reflect the state of the material as it is manufactured. More research on neutron-irradiation effects is needed to understand the behaviour of these materials and changes in their properties.

Regarding Zr alloys, due to their long-lasting use and research over 60 years, most of the behaviours are well understood and described, including the oxidation kinetics in various temperature ranges. These investigations describe the safety limits under which Zr alloys must operate and the conditions under which they can withstand accident scenarios.

Regarding newly proposed materials, FeCrAl alloys have been used successfully in other areas of engineering, but information about their usage and behaviour under irradiation is still in development and needs to be further understood. Although the information is limited, it is already known that these materials have neutron absorption that are higher than those of Zr alloys, and thus some solutions, such as a reduced thickness, have to be applied. The material strength of FeCrAl is higher than that of Zr alloys, allowing for a reduction in the thickness of the material. However, FeCrAl alloys generally have higher thermal expansion coefficients, making them more vulnerable to possible deformations due to high heat. Furthermore, these materials have better oxidation behaviours, due to formation of Al_2O_3 layer on the surface, serving as a protection coating against further degradation. Another limitation is in the case of the melting point, as most FeCrAl alloys have a melting point between 1700 and 1800 K.

Refractory ceramic SiC has been used for a long time in places where a high melting point (more than 3000 K) is required, such as metal or glass melting. Research has been conducted on the effects of irradiation on thermal properties. The biggest advantage of SiC is its high thermal conductivity and low thermal expansion coefficient in wide ranges of temperatures. As a result of the high temperature gradients, SiC is susceptible to cracks, as the temperature difference induces additional stresses. Long SiC tubes are often produced by winding fibres, in patterns, of desired diameters to achieve the required thickness and properties, and the winding could be done in multiple layers. SiC has weak resistance to hydrothermal corrosion, as the formed SiO_2 is soluble in the water environment, requiring an environmental barrier to protect material degradation and environmental damage.

Ti_3SiC_2 is a representative of MAX phase materials, which share the advantages of metals and ceramics and have high strength, resistance to oxidation, and are stable even at high temperatures. It has a high thermal conductivity that is only weakly dependent on temperature. Tubes of this material could be easily shaped by machining. Further research on irradiation effects is needed, to understand fully the defects induced and self-healing at high temperatures. Ti_3SiC_2 is has higher resistance to hydrothermal corrosion at lower temperatures, but at higher temperatures, the in water soluble SiO_2 over time is dissolved and the structural integrity of the oxide layer is compromised, leading to cracks and breaking-off of the oxide layers and thus progressing the oxidation.

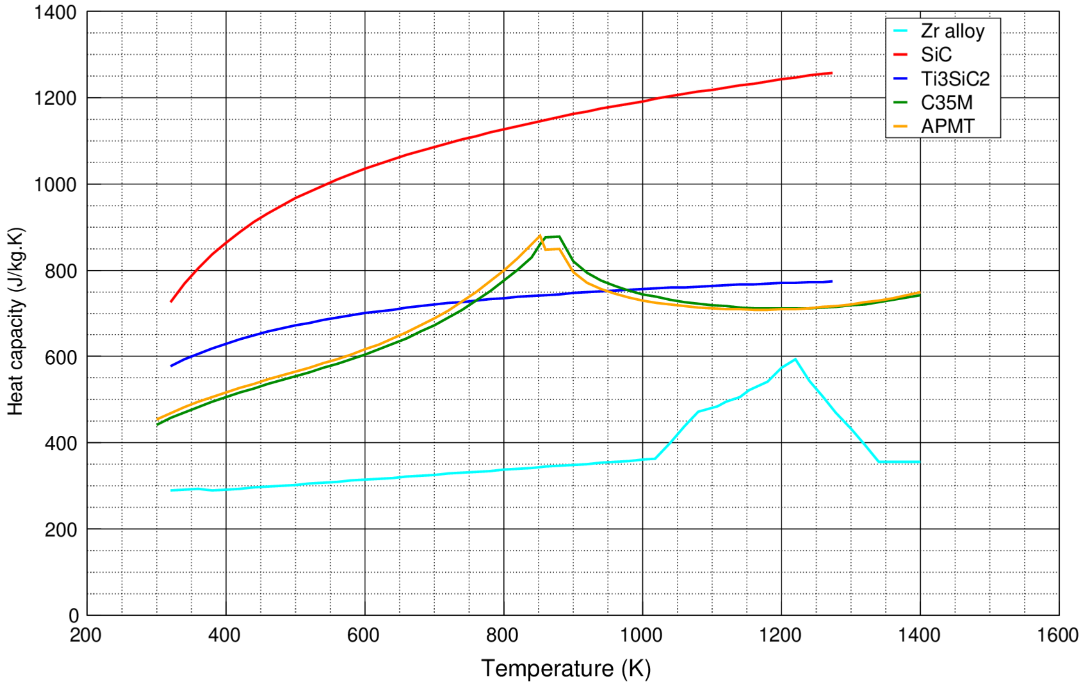

Fig. 2.2: Heat capacity c_p dependency on temperature T

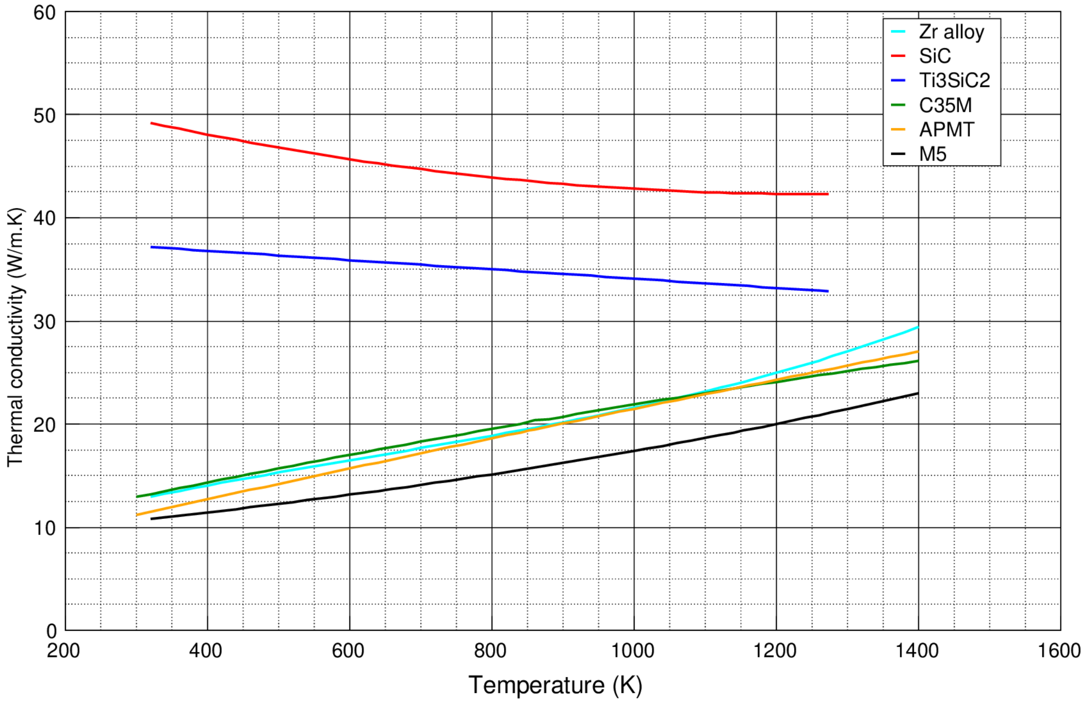

Fig. 2.3: Thermal conductivity k_t dependency on temperature T

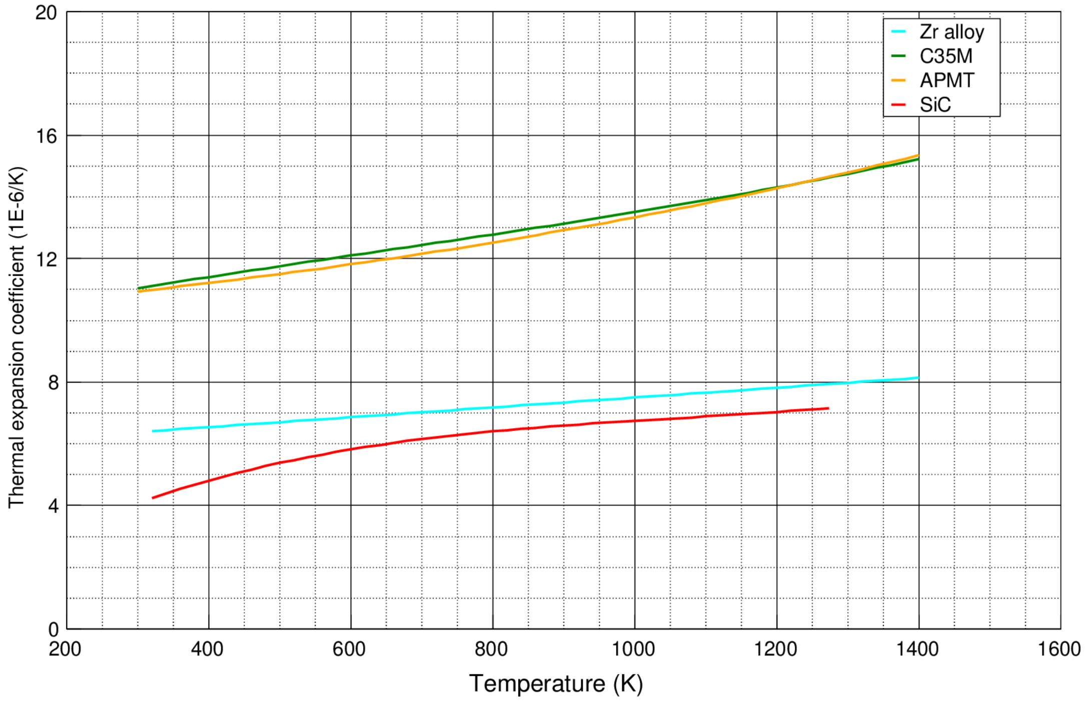

Fig. 2.4: Thermal expansion coefficient α dependency on temperature T

2.4 Protection coatings

Another concept of ATF considers the development of protective coatings to protect Zr alloy-based cladding tubes. Protective coatings are proposed to greatly enhance corrosion and oxidation, particularly at high temperatures, where Zr alloys are susceptible to aggressive oxidation. In addition, hydrogen deposition on the Zr alloy microstructure would be greatly reduced and the wear resistance could be improved. The coating could be applied to the cladding during the fuel assembly manufacturing process. Although this coating process is used in many areas of engineering, further problematic factors have to be addressed, such as adhesion of the deposited layer, thermal conductivity, neutron cross section, irradiation stability and resistance, and mechanical properties. These factors have an influence on behaviour and overall performance during normal operation and accident scenarios. Multiple studies have been conducted to improve the Zr-based alloy cladding by deposition of metallic (Fe alloys, Cr, Cr-Al, Y, Ni-Cr), non-metallic (oxides, nitrides, and carbides), or MAX-phase coatings. Among coating materials, the highest level of desired performance during LOCA was observed in materials that form oxide phases of aluminium, chromium, zirconium, or silica. Coatings should not significantly affect neutron absorption in the core and should not reduce the heat transfer between the cladding and the coolant. Research shows that coating materials should have at least one Cr, Al, or Si component in the material composition to allow the formation of a protective layer, for example Cr_2O_3, Al_2O_3, SiO_2 [55].

2.4.1 FeCrAl coatings

Major research on this type of coating is underway on the development of a FeCrAl coating for nuclear applications by the Korea Atomic Energy Research Institute (KAERI), the University of Illinois. This type of coating requires a barrier layer between the coating and the cladding to prevent the formation of Zr-Fe eutecticum at high temperatures. Study [56] investigates the oxidation performance of Zircaloy-2 deposited by layer of FeCrAl using magnetron sputtering in high temperature steam environment. The sample with a coating of 1 micrometre thick, according to the results obtained, prevented Zircaloy-2 oxidation in steam at 700 ℃ for up to 15 hours, while the thinner coating of 0,3 micrometre thickness did not prevent oxidation. The autoclave test performance investigation for 20 days simulated in a boiling water reactor (BWR) environment showed adequate performance and the integrity of the cladding remained intact.

The research [57] conducted investigation about modification of protective layer deposition concepts by laser and arc ion implantation to increase the adhesion bond between substrate and coating layer. The samples obtained through the depositions by these methods have shown enhanced corrosion and oxidation, creep, and irradiation resistance.

FeCrAl alloys have been observed to have good resistance to heavy ion irradiation. There were no locations in samples of void formation with Cr-enriched phases for 10Cr and 13Cr FeCrAl alloys; Irradiation defects lead to increased hardness of coating [58]. Experiments showed that thick cold-sprayed FeCrAl coating have high oxidation resistance during autoclave tests and high temperature in air [59]. However, a fast diffusion of Fe from the coating to Zr alloys occurred, forming the interlayer of Fe_2Zr, $FeZr_2$ and $FeZr_3$ intermetallic phases [60]. $FeZr_2$ is known for its negative thermal expansion, the material shrinks as the temperature increases, inducing further stresses at the clad-coating interface [61].

In [59] [62] the FeCrAl coating deposited on Zr substrate using cold spraying was investigated. An interlayer of molybdenum was deposited between the coating and the substrate to suppress the diffusion of Fe to Zr at high temperatures. A complex multilayer structure was developed as a result of diffusion, shown in fig. 2.5. The resulting structure has shown an improved oxidation resistance of the Zr alloy when exposed to steam at 1200 °C. The ballooning behaviour and mechanical properties of coated samples studied under simulated LOCA conditions revealed a higher burst temperature, decreased strain, and reduced rupture size compared to those of an uncoated alloy.

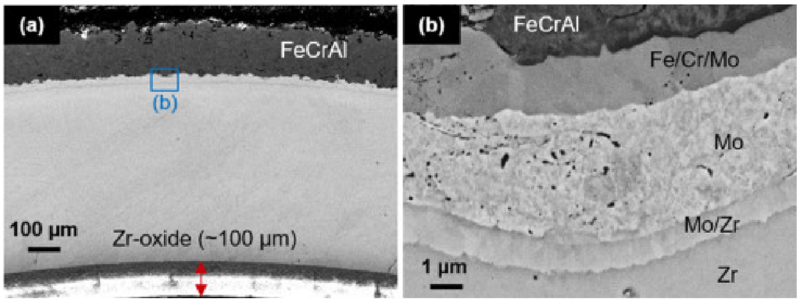

Fig. 2.5: FeCrAl/Mo/Zr complex microstructure [59]

2.4.2 Cr coating

Metallic Cr coating have a high potential due to their exceptional properties; they have high melting point, high corrosion resistance in water and steam environments, as they form protective layer of chromium oxide Cr_2O_3, and they have coefficient of thermal expansion close to Zr alloys. Multiple options of deposition of Cr on Zr substrates were developed, such as magnetron sputtering, cathodic arc deposition, cold spraying, laser cladding, electroplating, etc. Various full-scale tests of Cr coated

Zr alloy cladding and UO_2 fuel assemblies are being carried out, including in-pile tests [55].

The enhanced oxidation properties of Cr coated alloys were successfully demonstrated by multiple autoclave tests, which resulted in medium to high corrosion resistance in boric acid and oxygen in water solutions, showing a 50 to 100 micrometre thick stable layer of Cr_2O_3 after 3000 hours of autoclave test [63]. Chromium coatings on Zircaloy-4 have shown promising results under steady-state, power ramp, and LOCA conditions [64]. Furthermore, the Cr coating of thicknesses of 5 to 12 micrometres in Zircaloy-4 exhibited improved protection against steam oxidation at 1200 ℃. The experiment shows that the enhanced resistance to oxidation ensured the integrity of the cladding for a longer period, approximately 10 times longer than in the LOCA criteria used nowadays [65].

Report [66] exhibits that Cr coated Zr-1Nb alloys have enhanced oxidation resistance to high temperature steam oxidation at 1200 and 1300 ℃. The thickness of formed Cr_2O_3 oxide and residual Cr layers formed depends on the exposure time to the oxidation environment, probably caused by ongoing redox reactions between Cr oxide and zirconium, in fig. 2.6.

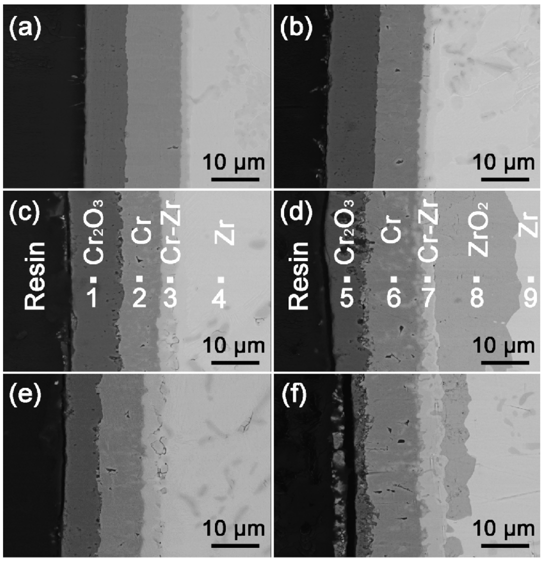

Fig. 2.6: SEM images of the microstructure of Cr coated Zr alloy after high temperature steam oxidation at 1200 ℃ for 0,5 h (a), 1 h (b), 2 h (c), 4 h (d), and at 1300 ℃ for 0,5 h (e) and 1 h (f) [66]

Mechanical tests at room and elevated temperatures showed no significant dissimilarities between coated and uncoated claddings [55]. Comparative analysis of Cr and CrN coated Zircaloy-4 deposited by the multiarc ion method was executed.

Shows that Cr coatings exhibit a transition from brittle to ductile under thermomechanical loads, resulting in an improved cracking resistance in comparison to that of CrN coating [67].

Study [68] shows appropriate resistance of chromium coatings under ion irradiation. The samples retained the adhesion of the coating layer and microstructure stability. Swelling of 1,6 % was observed at 500 °C under heavy-ion radiation of 1,4 MeV, up to 25 DPA. And the results are lower than the acceptable limit value of 5 % for reactor materials [69]. Cr-Al intermetallic coatings show improved oxidation resistance compared to pure chromium [70]. However, a more complex and heterogeneous structure of oxide layers is formed during oxidation, requiring more detailed research, especially under long-term high-temperature steam oxidation, as well as under Design Extension Conditions (DEC) [71]. Ni-Cr coatings show toughness better than that of pure chromium coatings; however, at high temperatures, they exhibit lower oxidation resistance because of the rapid diffusion of Ni into zirconium alloys [72].

2.4.3 Nitride protection coatings

Development of titanium nitride (TiN) and titanium aluminium nitride (TiAlN) coatings is being carried out for the cladding of Zr alloys. In report [73] the substrates of Zircaloy-4 were deposited by TiN and $Ti_{0,35}Al_{0,65}N$ protective layer by pulsed laser deposition process. These samples were exposed to a supercritical water environment (500 °C and 25 MPa) for 48 hours. The coated samples were intact after exposure, while the uncoated samples showed severe degradation and progressed to breakaway corrosion.

TiAlN and TiN coatings applied to ZIRLO™ to improve corrosion resistance in a high temperature water environment showed good adhesion to the substrate surface when the surface was properly prepared and the Ti interlayer was deposited. The coating layers of TiN and TiAlN were deposited by a cathodic arc vapour deposition process (CA-PVD). The sample with an interlayer of 0,6 micrometres thick, with surface roughness of 0,25 micrometres shows the best results with the smallest weight gain in the water environment at 360 °C, 18,7 MPa and 72 hours of exposure. Measurement of a specimen coated with TiAlN by scanning electron microscopy (SEM) has shown that Al partially reacted with water while forming the boehmite phase (aluminium oxide hydroxide), resulting in a degradation of the resistance to corrosion in the water environment. Formation of the boehmite phase may be reduced by applying the multilayer coating approach of the Ti interlayer, TiAlN, and TiN layer (in the direction from the substrate to the surface) [74].

Study [75] focusses on the hydrogenation of Zr-1Nb alloy coated by TiN coating applied by magnetron sputtering and filtered vacuum arc. The hydrogen absorption rate of the coated sample has decreased in comparison to that of the samples of an uncoated Zr alloy. Lower absorption is caused by the formation of oxide films on the surface of the deposited layer, thus preventing hydrogen permeation to the microstructure. The evaporated coating by the filtered vacuum arc process shows a denser and more homogeneous structure, leading to lower hydrogen absorption compared to the coating deposited by magnetron sputtering. Furthermore, the implementation of a Ti interface layer was performed, and then gas-phase hydrogenation was conducted to simulate conditions comparable to those in PWR operation. The results show that the hydrogen is mostly absorbed in the Ti interface layer, whereas a small amount is absorbed into the TiN coating. When the maximum concentration that the Ti layer is able to absorb is exceeded, an amount of hydrogen penetrates the Zr substrate, forming hydride phases; however, no lattice distortions were observed. The lowest hydrogen absorption rate was achieved by deposition of Ti interface layer and TiN layer by evaporation using a vacuum arc process. The results show that TiN coatings are suitable for use as barrier coatings to reduce the amount of hydrogen absorption to the interface layer, which can contain the penetrated hydrogen. The combination of both layers thus provides reliable protection against hydrogen embrittlement of the Zr-1Nb alloy.

In [76] the heavy particle irradiation and its effects on the TiN coating were examined. The results show that the TiN is susceptible to dissociation when exposed to energetic particle bombardment (Radiation Induced Segregation - RIS), in fig. 2.7, leading to formation of Ti enriched spots, where at high temperature, hydrogen by oxidation would be produced, similarly to the oxidation of Zr alloys under accident conditions. It was also observed that the formation of inert gases in the microstructure of TiN coating can enhance the RIS effects. The suggestions in this report are to focus more on materials with reduced activation to reduce the forming of inert gas bubbles. With the results in mind, MAX phase compounds and high-entropy alloys (HEAs), should be further investigated for possible use, as they are not prone to irradiation damage like TiN.

However, as TiN acts well as a diffusion barrier, when intacted, it has a huge negative in case of its thermal properties. The coefficient of thermal expansion is high compared to that of Zr alloys, which leads to induction of stresses on the coating and material surface. Experiments have shown that the TiN is subject to cracking, which reduces the protection of the Zr substrate and allows the diffusion of oxygen into the Zr microstructure. The layer is too thin to effectively form a sufficiently thick layer of TiO_2 that could inhibit oxygen diffusion. This process can be observed during thermal cycling [77].

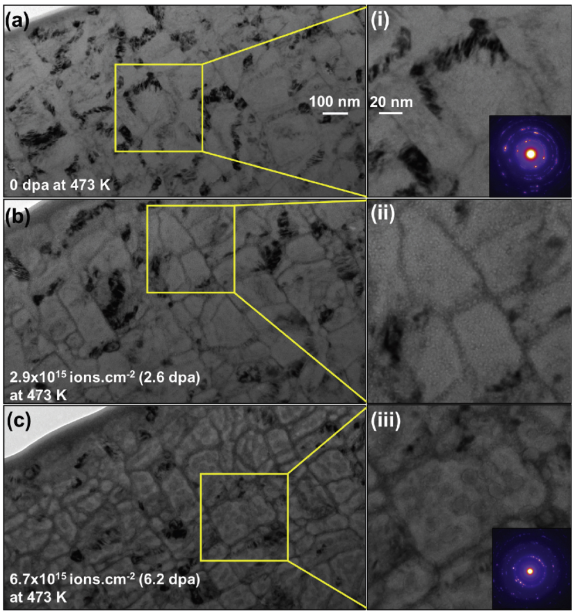
(a)
100 nm
0 dpa at 473 K
(i)
20 nm
(b)
2.9x10^{15} ions.cm^{-2} (2.6 dpa)
at 473 K
(ii)
(c)
6.7x10^{15} ions.cm^{-2} (6.2 dpa)
at 473 K
(iii)

Fig. 2.7: SEM scan of TiN that underwent heavy particle irradiation - RIS [76]

2.4.4 Carbide protection coatings

SiC has a number of properties that are favourable for use; the basic properties were already introduced in section 2.3.2. SiC coatings could be deposited on the Zr alloys by magnetron sputtering. Such an applied coating exhibits an enhanced oxidation resistance up to 900 °C steam, as they are prone to form a protective SiO_2 oxide layer in high temperature, water-containing environments - similar to accident scenarios, however, the problems with water dissolution of this layer were addressed in section 2.3.2. Si interface layer provides for improved adhesion of the SiC coating to the substrate and further improves the oxidation resistance. Although the SiC and Si layers were oxidised, oxidation of the Zr alloy was prevented, rendering the use of SiC coating viable for coating of cladding in nuclear applications [78].

The research [79] experiments with deposition of amorphous SiC coating on Zr-1Nb alloy by magnetron sputtering method. The hydrogen absorption behaviour was investigated in a temperature range of 350 to 450 °C during hydrogenation by the gas phase. With the deposited SiC layer, the absorption of hydrogen into the Zr alloy was significantly decreased, because SiC is not prone to hydrogen deposition into its microstructure. The absorption decreases approximately 8 times at a temperature of 450 °C, compared to the uncoated Zr alloy with a thin oxide layer of ZrO_2. Hydrogen trapping at the C-rich interface between the substrate and the coating was observed. No adhesion deterioration was observed up to 450 °C.

2.4.5 MAX phase protection coatings

Aluminium oxide forming MAX phases exhibit superior oxidation resistance at high temperature and show self-healing ability. Investigation of high temperature oxidation of Ti_2AlC coating, 12 micrometre thick, on ZIRLO alloy, in pure steam at 1000 to 1200 ℃ shows a significantly increased resistance to oxidation because the coating remains intact during 5 minutes of exposure time. The improvement in oxidation resistance is the result of a dense coating microstructure and a triple oxide layer of the alpha phase Al_2O_3 and rutile phase TiO_2/alpha phase Al_2O_3/TiO_2 [80].

Report [81] concludes experiment of Ti_2AlC coating deposited on Zircaloy-4 in steam-argon mixture at 1005 ℃ for 20 minutes. These conditions simulate the LOCA scenario at its start; the test was followed by water quenching. The coating protected the Zr alloy from oxidation, showing increased hardness, about four times higher than that of Zr alloys, and wear resistance while having good adherence to the substrate. Research continues to reduce the thickness of the coating to improve the neutronics economy and to achieve depositions on tubular geometries. Further long-term steam autoclave and hydrogenation tests must be performed.

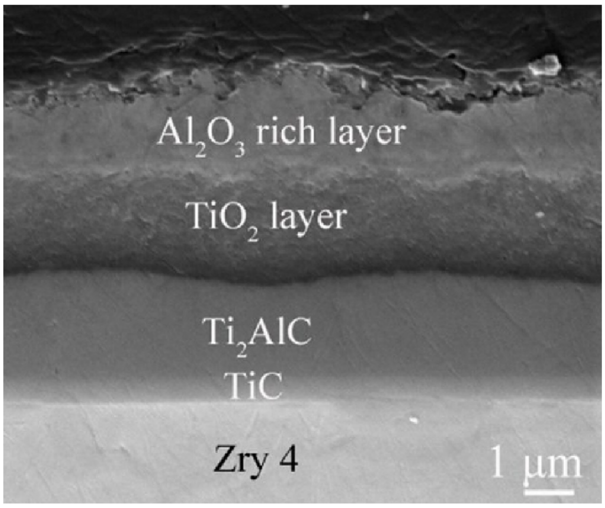

Fig. 2.8: SEM scan Ti_2AlC/TiC coating after oxidation at 800 ℃ in steam for 250 minutes [82]

Research [82] on the thinner Ti_2AlC/TiC coatings was performed. The coating was applied by magnetron sputtering on the Zircaloy-4 substrate. Coated samples exhibited parabolic oxidation kinetics, with significantly higher oxidation resistance compared to uncoated Zircaloy-4. Without the TiC barrier, two layers of mixed oxides were formed: the outer layer consisted of rutile Al_2O_3 and TiO_2, while the inner layer consisted mainly of TiO_2. With the TiC barrier, the three layers of oxide were formed: rutile phase Al_2O_3 and TiO_2/rutile Al_2O_3/TiO_2. The TiC barrier inhibited the diffusion of Al from the coating into the substrate structure, resulting in better performance in oxidation environments and improved durability. Both coatings with and without the barrier were rapidly oxidised at temperatures greater than 1000 ℃, as the protective effect was negligible. However, it should be noted that the coating thickness was 5 micrometres thick and with or without a 0,5 micrometre thick TiC barrier. Most reports are about coatings of thicknesses in tenths of micrometres.

3 APR1400 - Advanced Power Reactor

The APR1400, designed by Korea Electric Power Company (KEPCO), is an evolutionary reactor design of generation III that incorporates a variety of engineered features to improve safety and economics and increase operation reliability, compared to its predecessor, the OPR1000 plant. APR1400 is a 1400 MWe pressurised light water reactor and uses innovative active and passive safety systems to provide high-performance and safe reactor operating conditions. The plant overview is shown in fig. 3.1 [83]. The impact of advanced cladding materials on performance under severe accident conditions would be simulated on the APR1400 model available at the Department of Electrical Engineering of FEEC BUT.

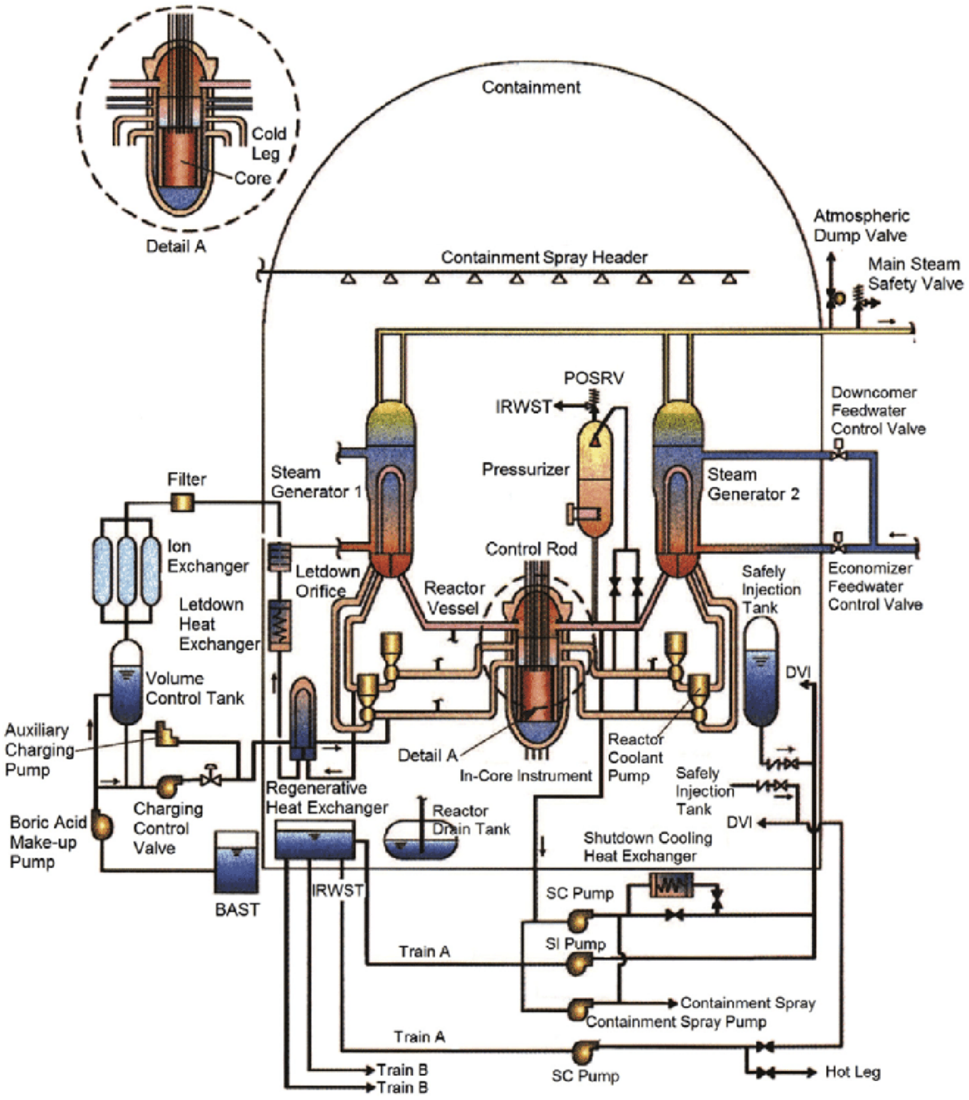
Cold Leg
Core
Detail A
Containment
Atmospheric Dump Valve
Containment Spray Header
Main Steam Safety Valve
POSRV
IRWST
Downcomer Feedwater Control Valve
Pressurizer
Steam Generator 1
Steam Generator 2
Filter
Ion Exchanger
Control Rod
Letdown Orifice
Safely Injection Tank
Economizer Feedwater Control Valve
Letdown Heat Exchanger
Reactor Vessel
DVI
Volume Control Tank
Auxiliary Charging Pump
Detail A
Reactor Coolant Pump
In-Core Instrument
Safely Injection Tank
Regenerative Heat Exchanger
Charging Control Valve
Boric Acid Make-up Pump
Reactor Drain Tank
DVI
Shutdown Cooling Heat Exchanger
IRWST
BAST
SC Pump
SI Pump
Train A
Containment Spray
Containment Spray Pump
Train A
Train B
Train B
SC Pump
Hot Leg

Fig. 3.1: APR1400 plant - schematic overview of reactor coolant system and engineered safety features [84]

3.1 Plant description

In general, the APR1400 is designed in twin-unit concept and a slide-along arrangement with common facilities, e.g., radwaste and access control building. Auxiliary systems building, where safety systems are accommodated, surround the reactor building structure. The reactor building is a containment made of a post-tensioned cylindrical concrete wall, with an inner steel liner and reinforced concrete structures. Containment houses all components of reactor coolant system, a reactor, steam generators, pressuriser, reactor coolant loops, in-containment refuelling water storage tank (IRWST) and parts of the auxiliary systems. The turbine building houses the turbine generator (TG), condenser systems, reheaters, condenser, condensate and feedwater systems, and other systems related to power generation.

The reactor coolant system (RCS) has two coolant loops, the coolant is circulated in a closed cycle, removing heat from the core and internals and transferring it to the secondary system through steam generators (SG). The main components are reactor pressure vessel (RPV), steam generators, reactor coolant pumps (RCP), pressuriser, and components related piping. Each coolant loop consists of a steam generator and two reactor coolant pumps, connected to the reactor pressure vessel. The pressuriser is connected to one of the hot legs between RPV and SG of the second loop via the surge line.

The reactor pressure vessel, shown in fig. 3.2, is a cylindrical vessel with a welded hemispherical lower head and a removable closure head at the top. The pressure vessel contains internal and core support structures, fuel assemblies, control element assemblies (CEA), and instrumentation and control components. The core support structures are designed to support and orient the fuel assemblies and CEA and direct the flow of coolant through the core. Reactor coolant flows into the pressure vessel downcomer annulus through the inlet nozzles from the reactor coolant pump, through the bottom plenum, the core and flows out through outlet nozzles to the hot legs. The reactor core is designed for a nominal power output of 3983 MWt. In total, 241 fuel assemblies are loaded in the core.

The steam generators are vertical with an inverse U-tube heat exchanger and an integral economiser. Two steam generators transfer heat from the RCS to the secondary system. The RCS coolant flows in the tubes, and the secondary coolant is outside the tubes on the SG shell side. Water is injected into the steam generator through the downcomer from the feedwater system. Flows through the lower plenum where it is mixed with economiser feedwater with higher parameters to enhance the thermal efficiency. The water absorbs the heat from the U-tubes and evaporates. Evaporated steam flows through the separator, which separates the water droplets, and through the steam dryer. The saturated steam produced in the SG drives the turbine to which the generator is connected. The cross section of steam generator is shown in fig. 3.3 [83].

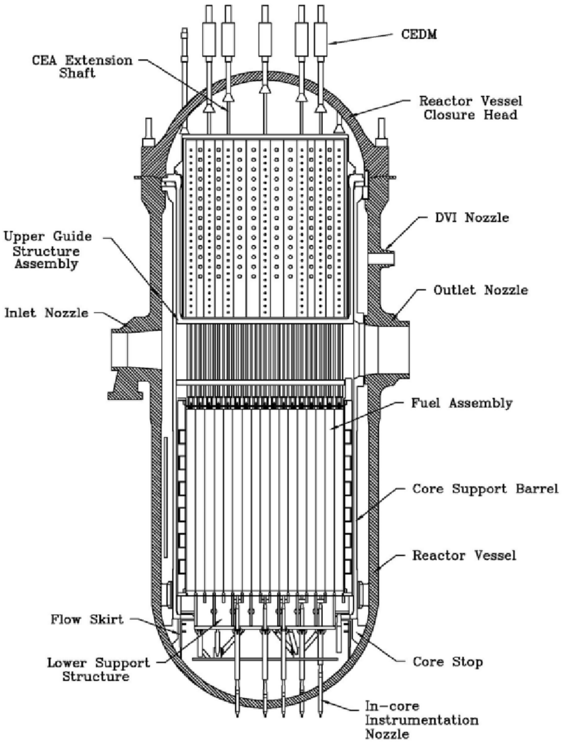
CEDM
CEA Extension Shaft
Reactor Vessel Closure Head
DVI Nozzle
Upper Guide Structure Assembly
Outlet Nozzle
Inlet Nozzle
Fuel Assembly
Core Support Barrel
Reactor Vessel
Flow Skirt
Lower Support Structure
Core Stop
In-core Instrumentation Nozzle

Fig. 3.2: Reactor pressure vessel [83]

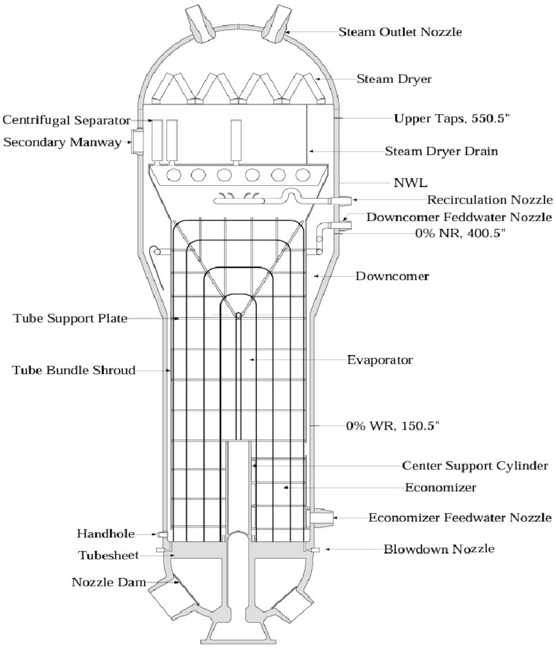
Steam Outlet Nozzle
Steam Dryer
Centrifugal Separator
Upper Taps, 550.5"
Secondary Manway
Steam Dryer Drain
NWL
Recirculation Nozzle
Downcomer Feddwater Nozzle
0% NR, 400.5"
Downcomer
Tube Support Plate
Evaporator
Tube Bundle Shroud
0% WR, 150.5"
Center Support Cylinder
Economizer
Economizer Feedwater Nozzle
Handhole
Tubesheet
Blowdown Nozzle
Nozzle Dam

Fig. 3.3: Steam generator [83]

3.2 Plant safety under accident conditions

The main system responsible for the actuation of the safety features is a plant protection system (PPS). The system initiates an adequate means of mitigation when certain setpoints, such as pressure, temperature, or flow rate, are met. Most of the safety systems and their connections are shown in fig. 3.1.

Safety injection system (SIS) is designed to restore, maintain the water level, and provide core cooling in the event of loss of coolant accident. By preventing prolonged core uncovering, fuel oxidation and damage is limited. The safety injection system uses unique direct vessel injection nozzles through which the coolant is injected directly into the RPV. Two diverse systems are used for injection: passive safety injection tanks that start to inject borated water when the RCS pressure decreases below the opening pressure of the check valves, and active safety injection pumps are started upon the actuation signal of low water level in the SIT.

Shutdown cooling system (SCS) is employed to further reduce the temperature in the RCS. Initially, the cooldown phase is accomplished by heat dissipation from the steam generators. After the decrease in the temperature and pressure of the RCS, the SCS is activated. SCS could also be used to remove heat from RCS after accidents.

The containment spray system reduces the pressure and temperature in containment following LOCA and the main steam line break events. The spray system also removes fission products in the containment atmosphere and mitigates radioactive release. Safety depressurisation and vent system (SDVS) provides means for RCS depressurisation in case of loss of ultimate heat sink - steam generator dry-out. The system is capable of rapid depressurisation of the RCS using pilot operated safety relief valves (POSRVs).

The auxiliary feedwater system (AFWS) supplies feedwater to the SG secondary side and allows for heat removal from the RCS, the system starts upon the loss of offsite power, although the DC power has to be available for system controllability. The auxiliary feedwater system has two divisions, one for each SG, and each division has two trains, one supplied by motor-driven pump and the second by turbine-driven pump. Each pump is able to provide for 100 % of the required flow rate. The main steam lines and steam generators are protected against overpressurisation by multiple safety valves. The main steam safety valves with AFWS could be used for feed-and-bleed operation through the secondary system, when the turbine bypass is inoperable.

3.2.1 Severe accident management

Severe accidents in the APR1400 design are addressed in two ways based on the phenomenon and its likelihood to cause containment failure and radioactive release, two categories are considered for the implementation of mitigation measures:

- For phenomena likely to cause early containment failure within 24 hours after accidents, mitigation systems shall be provided
- For phenomena that potentially lead to late containment failure if not adequately mitigated, the mitigation system or design measures should be considered in conjunction with the results of probabilistic risk assessment

Hydrogen generation is considerably higher during severe accidents than during DBA because of prolonged and significant cladding degradation. The hydrogen management system (HMS) limits the hydrogen concentration below 10 % in the containment atmosphere. Passive autocatalytic recombiners (PARs) remove hydrogen under accident conditions, where slow hydrogen release may be expected. PARs are supplemented with hydrogen igniters for accidents during which rapid hydrogen release occurs. Hydrogen igniters burn hydrogen at a controlled rate [83].

During scenarios with core melting, the ex-vessel cooling system is used to retain corium in the vessel; the principle is shown in fig. 3.4. The system floods and maintains the water level in the reactor cavity, and heat is conducted through the RPV walls to the water. The RPV and molten corium are cooled, slowing the melting of the lower head, and eventually corium solidifies in the RPV. The cavity flooding is used to cool the corium that has melted through the vessel and ejected to the cavity [85].

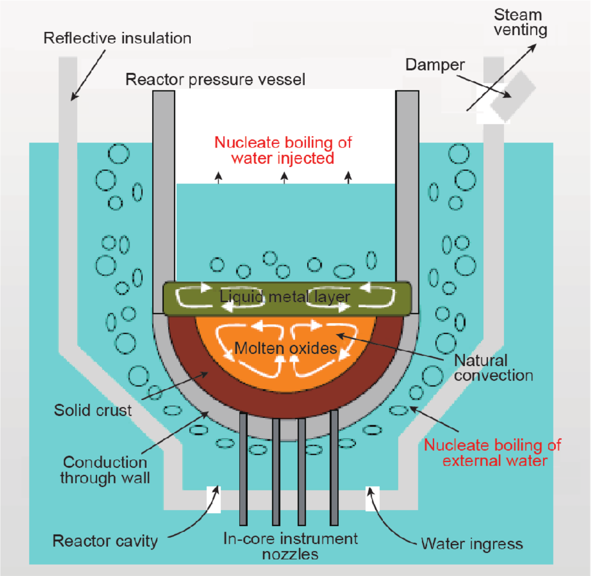
Steam venting
Reflective insulation
Damper
Reactor pressure vessel
Nucleate boiling of water injected
Liquid metal layer
Molten oxides
Natural convection
Solid crust
Nucleate boiling of external water
Conduction through wall
Reactor cavity
In-core instrument nozzles
Water ingress

Fig. 3.4: In-vessel corium retention [85]

4 Design Basis Accidents, Beyond Design Basis and Design Extension Conditions

Design basis accidents (DBA) are postulated accidents to which the nuclear power plants are designed according to established design criteria [86]. That is, the NPP has to withstand such an accident without loss to the systems, structures, and components that are necessary to ensure public health and safety. Under the conditions of such accidents, the fuel damage and the release of radioactive material are kept within the authorised limits. Safety limits for the principal design criteria of LWR are established for DBA under the US NRC publication 10 CFR 50 [87]. For APR1400 plant, the limits are as follows:

Tab. 4.1: Safety limits for the principal design criteria of LWR [87]

Criteria	Limit
Peak cladding temperature	1204 °C
Departure from nucleate boiling ratio (DNBR)	$> 1{,}3$
RCS pressure	$<$ 19,3 Mpa
Hydrogen generation	$<$ 1%
Containment pressure	$<$ 0,4 Mpa
Containment temperature	$<$ 140 °C
Containment leak rate	$<$ 0,2 vol.%/day
Exposure dose limit	$\sim$ 5 mSv (whole body)
	$\sim$ 30 mSv (thyroid dose)

These accidents are not expected to occur, but are postulated to occur to set the design basis. A single failure criterion is assumed under DBA conditions.

Beyond design basis events (BDBE) and design extension conditions (DEC) are not expected during plant lifetime and are very unlikely to occur. The conditions in these scenarios are more severe than in DBA. In general, DEC are selected conditions beyond the DBAs, to which the NPPs still shall have provisions to prevent unacceptable radiological consequences, but to the practical extent and may or may not include core damage. In BDBE, a multiple failure criterion is assumed.

- DEC category A - Assume design extension rules without severe fuel degradation, with deterministic acceptance criteria on containment performance limits, without radiological acceptance criteria - focused on prevention
- DEC category B - Assume design extension rules with severe fuel degradation, with deterministic acceptance criteria on containment performance limits, without radiological acceptance criteria - focused on mitigation

In fig. 4.1 the plant design envelope is shown. The envelope categorises plants states under design rules and outlines the core condition during the plant states together with analyses acceptance criteria. Defence-in-depth levels are assigned for the plant states with the required operator procedures. The confidence in radioactive release prevention is degrading when design basis rules are violated. Graded offsite response would be needed for beyond design basis events, while DBA should not require such response.

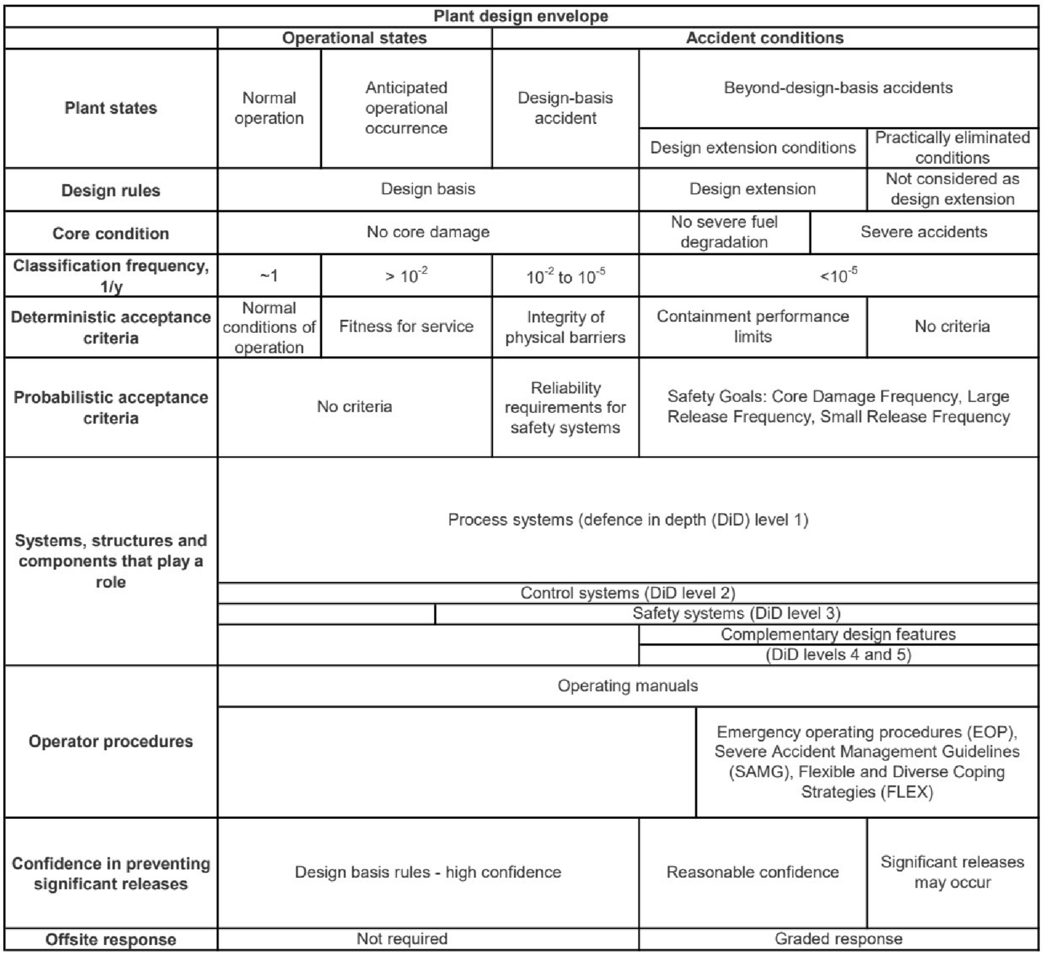

Plant design envelope					
	Operational states		Accident conditions		
Plant states	Normal operation	Anticipated operational occurrence	Design-basis accident	Beyond-design-basis accidents	
				Design extension conditions	Practically eliminated conditions
Design rules	Design basis			Design extension	Not considered as design extension
Core condition	No core damage			No severe fuel degradation	Severe accidents
Classification frequency, 1/y	~1	> 10^{-2}	10^{-2} to 10^{-5}	<10^{-5}	
Deterministic acceptance criteria	Normal conditions of operation	Fitness for service	Integrity of physical barriers	Containment performance limits	No criteria
Probabilistic acceptance criteria	No criteria		Reliability requirements for safety systems	Safety Goals: Core Damage Frequency, Large Release Frequency, Small Release Frequency	
Systems, structures and components that play a role	Process systems (defence in depth (DiD) level 1)				
	Control systems (DiD level 2)				
		Safety systems (DiD level 3)			
				Complementary design features (DiD levels 4 and 5)	
Operator procedures	Operating manuals				
				Emergency operating procedures (EOP), Severe Accident Management Guidelines (SAMG), Flexible and Diverse Coping Strategies (FLEX)	
Confidence in preventing significant releases	Design basis rules - high confidence			Reasonable confidence	Significant releases may occur
Offsite response	Not required			Graded response	

Fig. 4.1: Impact of plant design envelope and plant states [88]

Severe accident (SA) conditions involve severe degradation of fuel in core, particular DBA like Large Break Loss Of Coolant Accident (LB LOCA) may progress to severe under specific conditions with assumption of multiple failure criterion. Station Blackout is an example of an event under Beyond Design Basis category; it progresses to severe accident if plant power is not restored before the DC power reserve is depleted and if the FLEX equipment is not available. The station blackout event and the unmitigated LB LOCA were selected as scenarios to evaluate the advanced cladding materials under severe accident conditions.

4.1 Large Break - Loss Of Coolant Accident

The initiating event for this scenario is a guillotine break of the cold leg pipe between the RPV and the RCP, the equivalent break area is 200 % of cold leg area. For successful accident mitigation, the ESF must control reactivity, maintain water inventory to prevent prolonged core uncovering, and remove heat from RCS. The scenario could be divided into three parts, blowout, refill, and reflood, followed by long-term cooling.

Just after the break occurs, the coolant is blown out of the RCS as the pressure difference between the RCS and the containment atmosphere is very high. As the pressure and temperature of the coolant decrease rapidly, it flashes and changes its state from liquid to vapour. Heat transfer from fuel to coolant drops as the core is dried, resulting in an immediate increase in the cladding temperature (PCT).

Refill starts after blowout by emergency core coolant (ECC) - borated water injection into the downcomer of RPV. However, there is still a significant flow of steam upward in the downcomer annulus, preventing the water from reaching the lower plenum, thus the water flow partially bypasses the inlet and flows out through the break. After further depressurisation, and decrease of steam flow in the downcomer annulus that was restricting the flow (counter-current flow limitation), the water injected is able to fill up the core. The coolant is supplied by SIT via DVI when the RCS pressure drops below the opening pressure of the check valves for a limited time period.

In the reflooding phase, the core coolant is vertically stratified, the water level in the RPV increases with time, and heat transfer becomes more complex. The core water level is proportional to the mass of water injected. Below the water level in the core, where there is a low void fraction, the bubbly flow regime occurs, and nucleate boiling is the dominant convection mode. Above the water level, there is a high void fraction, the mist flow regime occurs. Vapour-liquid mixture flows from the upper plenum to the SG and back into the cold leg, flowing out of the break. The phenomenon of steam binding may occur; mixture could be reheated from the secondary side and hot structures, reversing the heat flow, increasing the temperature and pressure in the RCS, restricting the reflooding rate and core water level recovery. Water is supplied via DVI from IRWST by a low-pressure safety injection system. The system is started when the water level in the SITs reaches the low water level setpoint [89].

4.2 Station Blackout

The results of the Probabilistic Risk Assessment have shown that the SBO is a dominant sequence that results in core damage and containment failure in the APR1400 plant. The initiating event to station blackout (SBO) is a loss of offsite power (LOOP) with a concurrent failure of emergency diesel generators (EDGs). With the loss of AC power sources, most active safety systems dependent on these sources are rendered unavailable. For prevention of SBO progression, installed non-safety class alternative AC (AAC) power sources may supply power to essential safety equipment to ensure that safety function is maintained. However, even these may fail. With the loss of all AC power, the plant is left with only safety systems powered by DC from station batteries and passive systems, which do not need electricity for their function. Under these conditions, only turbine-driven auxiliary feedwater pumps can be operated to supply cooling water to the SGs. Reactor coolant pumps cannot provide forced circulation of coolant, natural circulation is the only mean to remove heat from the core, but only if the conditions are met. Conditions for natural circulation are: the height difference between the heat source and the sink, the temperature difference between the source and sink systems, and the continuous stream of liquid.

Operators have to follow emergency operating procedures after recognising the initiating event and should restore electrical power before batteries are depleted. Station batteries can provide DC power for at most eight hours. If power is not restored, the SGs will dry out, and the ultimate heat sink will be lost. There are no further means to cool the RCS. Under these conditions, the SBO progresses to severe accident. When the core exit temperature exceeds 922 K, the severe accident management guidelines (SAMG) are initiated. Once again a power recovery action is performed using portable external power sources, and the recovery action could be applied continuously. At the same time, the operator monitors the main safety functions and performs mitigation measures when certain safety functions are challenged. Related measures are mitigation by RCS depressurisation, injection into SG, and injection to RCS. As a reaction to the Fukushima-Daichi accident, multiple measures were taken and APR1400 plants were equipped with upgraded AAC diesel generators, water-proof gates for the EDG rooms, and equipment and provisions were installed for external water injection for the RCS and SGs [90].

Furthermore, flexible and diverse coping strategies (FLEX) [706] were developed and introduced to improve the defence-in-depth, in fig. 4.2, for beyond design basis scenarios to address the loss of power and loss of access to ultimate heat sink occurring simultaneously on a site. FLEX strategies consist of both on-site equipment stored at the plant site and off-site equipment for the provision of additional materials and equipment for a longer-term response [91]. FLEX consists of the following key elements:

- Portable equipment that provides means of obtaining power and water to maintain or restore key safety functions for all reactors at a site
- Reasonable protection and placing of portable equipment from beyond design basis external events
- Procedures and guidelines for FLEX strategies implementation
- Programmatic controls that assure continued viability and reliability of the FLEX strategies

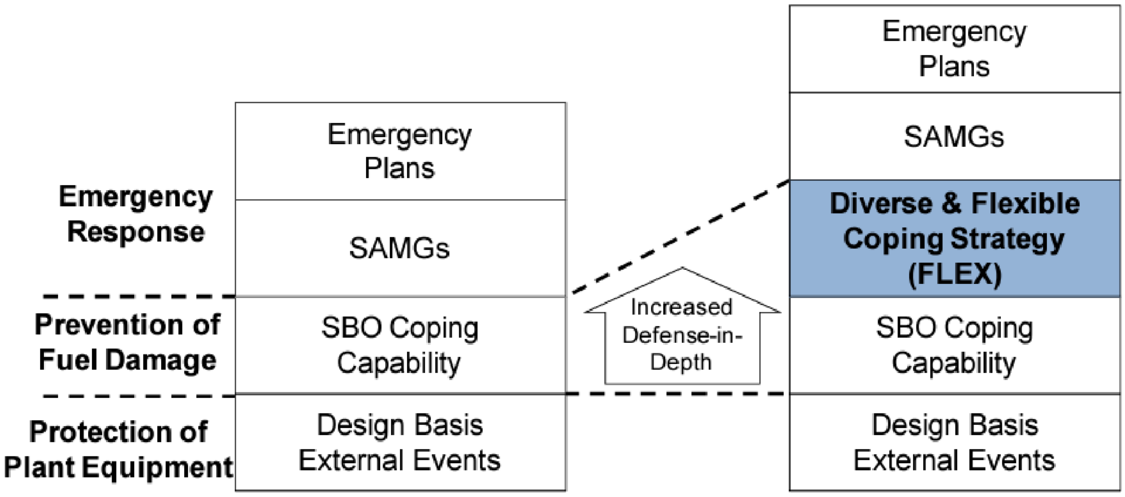
Emergency Response
Prevention of Fuel Damage
Protection of Plant Equipment
Emergency Plans
SAMGs
SBO Coping Capability
Design Basis External Events
Increased Defense-in-Depth
Emergency Plans
SAMGs
Diverse & Flexible Coping Strategy (FLEX)
SBO Coping Capability
Design Basis External Events

Fig. 4.2: FLEX enhances Defence-in-Depth [91]

5 Nuclear safety analysis

The objective of the safety analysis is to define and confirm, by appropriate means, the safety basis for crucial safety-related parts and systems of the plant and to ensure that the design can meet the dose limits and radioactive releases specified for plants under all conditions. Safety analyses are part of the plant design safety evaluation, used in the plant licencing procedure. Analyses should proceed while the design stage progresses for the purpose of verification. Analyses are not just a part of a plant design, but should be addressed during the plant lifetime, in order to reflect the progress in research and to account for plant design or site-specific modifications. Currently, there are two separate approaches to safety analysis that complement each other.

5.1 Deterministic safety analysis - DSA

The deterministic approach is based on studies of plant behaviour under operating conditions and under specific accident conditions identified on the basis of engineering evaluations or on compliance with the chosen criteria. Usually, deterministic analyses are performed based on conservative assumptions on input data (initial conditions), intermediate parameters, and on the behaviour of plant systems like single or multiple failures, etc. As the system is modelled and such modelling is not exact, the plant behaviour may vary from the real plant response. Deterministic analyses have been used for verification for a longer period, thus having a more robust and well-consolidated basis, mostly considering rare events and DBAs. DSA should consider various conditions and phenomena, normal operation, anticipated operational occurrences (AOO), and accidents.

The analysis of normal operation should assess the plant if the operation could be carried out safely, confirming that the radiological doses to the workers and the general public and that the planned release of radioactive material from the plant is within acceptable limits. All conditions met during normal plant operation should be considered, but without external and internal disturbances. These include start-up, normal power operation and power changes, various shutdown modes, and handling and storage of fresh and used fuel. Not only the limits, but also the "as low as reasonably achievable" principle (ALARA) should be complied with. ALARA is based on the avoidance of exposure to radiation that does not have a direct benefit to you, even if the dose is small; achievable by the use of three basic protective measures in radiation safety: time, distance, and shielding.

Anticipated operational occurrences are off-normal events, resulting in plant transients that are coped by plant protection systems, but which could potentially damage the reactor if another malfunction happens. The typical frequency is 10^{-2} per year. Design basis accidents have a lower frequency to occur, typically in range 10^{-2} to 10^{-6}, and are not considered to occur during the plant life, however, are considered for the design of safety systems. The typical AOO categories should be considered to be potential initiating events (IEs) of DBAs. Although the severity of IE has to be considered more severe. The number of IEs is large, to reduce it, the IE with same physical basis are grouped, and only the one from each group with most severe consequences is further studied, this IE is called bounding case. Each case has a figure of merit, such as peak RCS pressure, peak cladding temperature (PCT), or minimum departure from nucleate boiling ratio (minimum DNBR) which is evaluated and compared to safety acceptable design limits. Two cases from one group can cause a different response from the plant and lead to a reduction in safety margins in different ways; thus, both have to be studied.

The analysis should show that the plant can be safely shutdown and maintained under safety shutdown conditions, that decay heat is dissipated from the core at any time after the accident and that the radioactive release is below the limits. The time covered by the scenario analysis has to be appropriately long to allow the plant to reach safety shutdown conditions and reach cooled core state.

5.2 Probabilistic risk assessment - PRA

Probabilistic risk assessment, although not compulsory, has become a common practice for new plants and for existing ones. International requirements include that safety analysis reports must include a summary of the PRA study of the plant. PRA is a complex but well-structured method for identifying possible accident scenarios and risk estimates. However, the results may be influenced by uncertainty and misinterpreted (if the probability is very low, it is thought that it may happen in a far future). The PRA approach has some pros; no sequence of events is excluded before the analysis, so all possible combinations of events are addressed; the view is not particular on some systems, but rather on the plant in general, highlighting specific plant weakspots, allowing especially in the design phase to reconsider the design or to create systems more diverse, redundant, and robust.

In present, the support of plant safety decisions, including those related to operation, involves both DSA and PRA analyses. Probabilistic analysis is divided into three levels; level 1 examines events up to core damage; level 2 evaluates radioactivity releases from the plant, and level 3 considers external radiological consequences.

Concerning the external events in the probabilistic assessment, there is no unified approach. For example, the seismic event have two ways of handling; first, the maximum historical event in the location is taken in the consideration, significantly increasing the probability; second, the seismic hazard curve which considers the maximum ground acceleration and corresponding expected frequency.

Also the PRA considers human error. Human error should be avoided by the implementation of an advanced man-machine interface, operation and emergency procedures, and maintenance rules and guidelines. The human error is significantly higher during the accident scenarios; in general, the human error considers factors such as operator available time, stress, procedure state, and training [92].

5.3 MELCOR

MELCOR is a computer code developed by Sandia laboratories in the United States, for support in nuclear reactor technology safety. The code was initially developed for the analysis of nuclear reactor technology to assess potential risks and consequences for public safety. Currently, MELCOR is a second-generation fully integrated code for advanced modelling of the progression of severe accidents in LWR technology plants. A wide range of severe accident phenomena could be modelled and simulated in both BWR and PWR plants, including:

- Thermal-hydraulic response in the reactor coolant system, reactor cavity, containment and confinement buildings
- Core uncovering (during loss of coolant accidents), fuel heat-up, cladding oxidation, fuel rods loss of geometry, and core material melting and relocation
- Heat-up of reactor vessel lower head from the relocated fuel materials, including the thermal and mechanical stress induced, failure of the RPV lower head, transfer of core materials to the cavity
- Melted core-concrete interaction
- Hydrogen production, transport, combustion and deposition
- Fission product release and transport behaviour
- Radioactive aerosols behaviour in the containment
- Engineered safety features impacts on thermal hydraulic and radionuclide behaviour

The MELCOR utilises a modular structure with properly defined interfaces, so that all phenomena are explicitly addressed. Most models are mechanistic with high detail capabilities. However, the use of only parametric models is limited in areas of high phenomenological uncertainty, since there is no accepted mechanistic approach. MELCOR in this case allows for uncertainty analyses and sensitivity studies by including the optional adjustable parameters; such a solution allows for studies on effects of particular parameters on the simulated phenomena. These parameters, together with the numerical convergence criteria and iteration limits, are incorporated as sensitivity coefficients and are optional for use if needed. In MELCOR the use of a "control volume" is utilised for a description of the plant, nodalization; no specifics of nodalization are forced, allowing for the various levels of nodalization based on the details requested from the simulation. Specific geometry is considered only in the case that the reactor core and cloud be modelled as one basic model, or be detailed appropriately to the analysed phenomena [93].

6 Simulation in MELCOR

The code in primarily focused on severe accident analysis phenomena. Complex detailed modelling of all parts of the plant is not desirable and would significantly increase the calculation times, due to the increased number of volumes and flow paths that would need to be analysed by the codes solver. That is why the nodalization of the plant systems is simplified, although the model still provides accurate calculations of the severe accidents. Scenarios in which the advanced cladding materials were analysed are described below. As fuel melting, oxidation heat released, amount of hydrogen released, and progression of core damage are points of interest in these simulations, the core, lower plenum, and RPV lower head are modelled in detail. The plant and core nodalization are described in their respective section.

6.1 Scenarios

The performance of advanced cladding materials was analysed in three scenarios. All scenarios are set up that the 100 % damage of the core occurs, dependent on the event progression sooner or later, and the lower head would be penetrated. Under all scenarios, the multiple failure criterion is assumed. All initiating events were assumed to occur under full-power operation at nominal level. Before the initiating event, 12000 seconds (over 3,3 hours) of simulation were calculated, to achieve a steady state. The length of simulation depends on the scenario.

The first scenario - unmitigated LB LOCA - was used for the basic verification of the implementation of the materials and the modelling of oxidation in the core, especially the oxidation kinetics. The LB LOCA under DBA conditions was described above. For severe accident progression, multiple failure criterion was assumed, extending the event to be beyond design basis. This progression is accomplished by the loss of offsite power with concurrent loss of EDG and AAC sources. The loss of AC power renders the active engineered safety features unavailable. For core reflooding, safety injection pumps are used. As these pumps could not have been supplied by the power, the core would be exposed once again due to the evaporation of the borated water that filled the core after initial refill from safety injection tanks. When the core is exposed, it heats up and evaporated water oxidises the cladding. As a result of the cladding oxidation, the heat is released, increasing the cladding and fuel temperatures. Subsequently, hydrogen is released by oxidation. When the fuel or cladding temperature reaches the melting point, the cladding tube candles, after additional heating up, the fuel rods collapse. The formation of debris begins; corium emerges. The corium falls down the core and progressively heats up other fuel rods. After the corium drops to the support plate, it is stressed beyond its limits and eventually collapses. After the support structure fails, molten corium is dropped into the lower plenum, evaporating the remaining water, and steam furthermore oxidises not yet collapsed structures. Simultaneously the lower head is melted by the corium as there is no ex-vessel cooling available. In a certain time, the corium melts through the lower head and is ejected into the cavity, where it reacts with water and concrete (MCCI). The MELCOR does not have implemented a model of molten corium and user-defined materials interaction; thus, this phenomenon cannot be accurately observed. The length of simulation was 20000 seconds (over 5,5 hours) from the initiating event.

The second scenario is a station blackout with the concurrent loss of all AC and DC power sources, total power loss occurs in the plant. The control rods are immediately dropped into the core, stopping the chain reaction when the LOOP occurs. At the same time, forced flow of coolant in RCS ceases to exist as RCPs are coasting down, feedwater pumps and the auxiliary feedwater system are not available for operation, and the steam generators have begun to dry out, resulting in a decrease in water level. The ultimate heat sink (UHS) is lost. The temperature of the coolant increases; together with the pressure, the pressure is relieved by operation of POSRV. There is no makeup system available to restore the water level in the core and it begins to uncover. Due to uncovering the cladding begins oxidise. When the core outlet temperature reaches a setpoint, the RCS is depressurised, allowing for injection of borated from SIT when the check valves open. Partially refiling the core and cooling it down, slowing down the oxidation. However the volume of SIT is not infinite, injected water is evaporated in the core and vapour is released by the POSRV. After the volume of SIT is lost, the core progressively uncovers and melts down. Molten corium breaches through the support structure and eventually the lower head and is ejected to cavity. The length of simulation was 72 hours from the initiating event.

The third scenario is a station blackout with the concurrent loss of all AC power. Control rods are dropped into the core and RCPs begun to coast down. DC power is available in this scenario, allowing for cycling operation of auxiliary feedwater system between setpoints for 8 hours, extending the period before loss of UHS occurs and significantly cools down the core. After 8 hours, the AFW system is not operable, and steam generators begun to dry out. From this point the scenario is the same as the previous one, although the time before core damage occurs is prolonged. The length of simulation was 72 h from the initiating event.

6.2 Plant model

In fig. 6.1, a schematic overview of the RCS and the secondary system layout and flow directions is shown. RCS consists of 32 control volumes (CV), connected by flow paths (FL). The CV 130 represents the RPV downcomer, CV 150 represents the lower plenum below the core, CV 170 is a core volume, CV 180 represents the core bypass, and CV 260 is a region above the core, from where the coolant heated in core is directed to the hot legs 310 and 410, and partially back to the downcomer. Two coolant loops are modelled, CV's marked by 3xx number are part of loop A, and CV's marked by 4xx number are part of loop B. The pressuriser volume 500 is connected to the hot leg of loop A, and on top of the pressuriser is the POSRV. Volumes 320, 420 represent the SG inlet and are connected to the hot leg pipes 310 and 410 respectively, volumes 330 to 337, and volumes 430 to 437 represent the u-tubes of the SGs. CV's 350 and 450, are SG's coolant outlets, and are connected to intermediate legs x60 and x65. The reactor coolant pumps are placed between the intermediate legs and the cold legs piping.

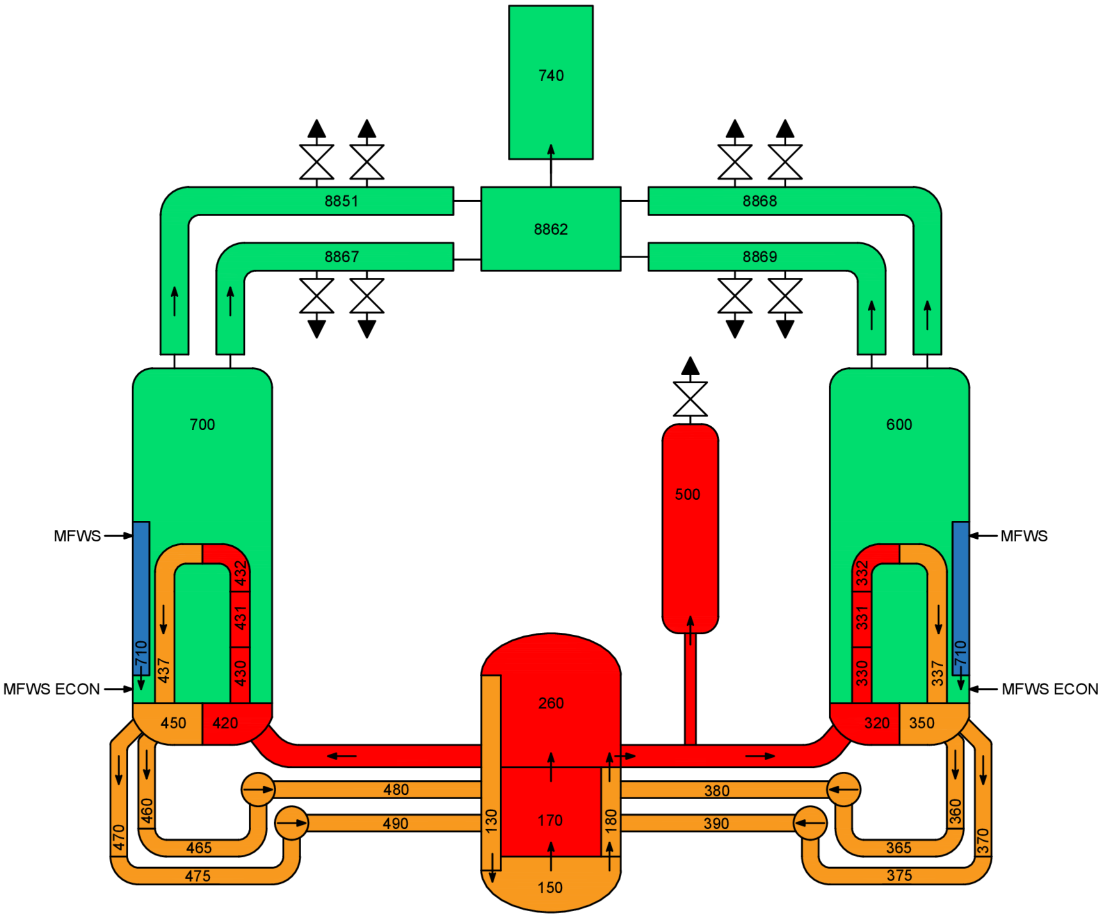
740
8851
8862
8868
8867
8869
700
600
500
MFWS
MFWS
MFWS ECON
MFWS ECON
710
437
432
431
430
450
420
332
331
330
337
710
320
350
260
480
490
380
390
130
170
180
150
460
470
465
475
360
370
365
375

Fig. 6.1: APR1400 plant nodalization - retrieved from [94]

The secondary system consists of 11 control volumes. CV's 600 and 700 are steam generator volumes, where the steam is produced. Volumes 610, 710 represent the downcomers for the feedwater. Volumes 8851, 8867, 8868 and 8869 are main steam limes, through which the steam produced in steam generators flows to the main steam hub 8862. Each main steam line is equipped with main steam safety valves and atmospheric dump valves. The main steam hub is connected to the 740 volume that represents the turbine. The boundary volumes of the secondary system are the main feedwater system (MFWS) and the turbine.

The reactor core is modelled in detail using a control volume and the COR package. In the COR package, not only is the core scheme modelled, but also the one of the lower plenum. The nodalization of the core and lower plenum is shown in fig. 6.2. The core is divided into 15 axial divisions and four radial rings. Axial levels 1 to 4 represent the volume of the lower plenum (blue). In radial rings 1 to 3 and in axial level 5 the core support plate is located (green), and the active fuel is in axial levels 6 to 15 (red).

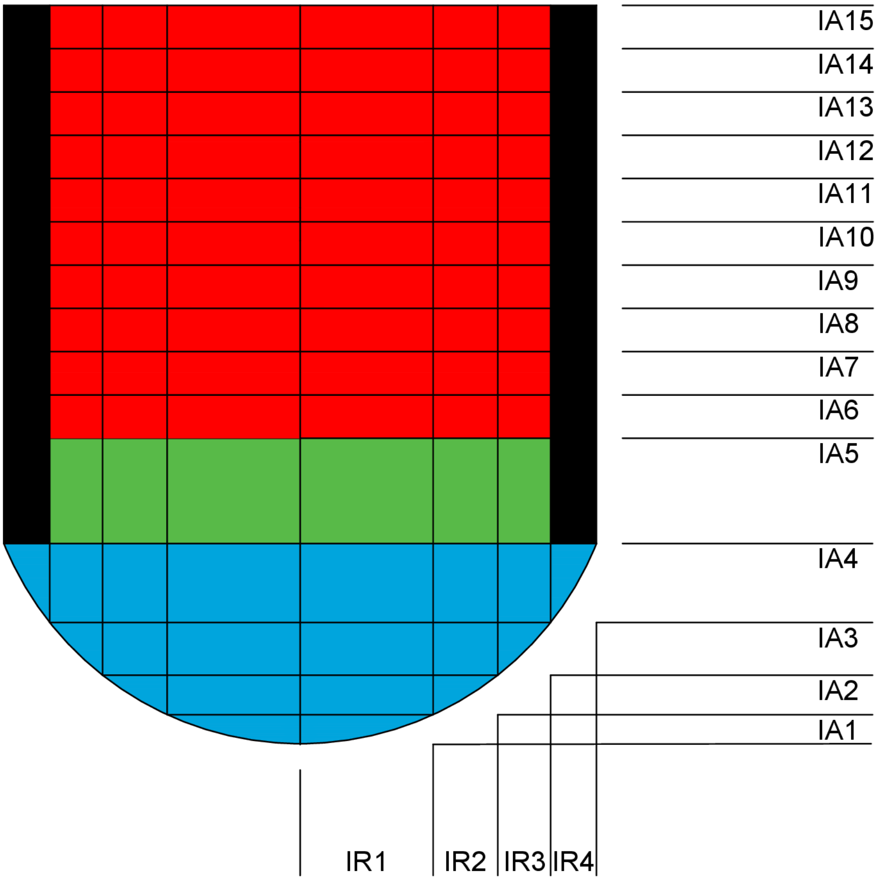

Fig. 6.2: Core and lower plenum nodalization - retrieved from [94]

6.3 Advanced cladding materials implementation

Advanced cladding materials used in simulations are not defined in MELCOR material libraries by default. The code allows for the implementation of user-defined materials. For cladding material and its use in the core, the pair of user metal and user oxide has to be defined with all required data. The user manual consists of a guide for implementation of the material pair, particularly for a FeCrAl alloy, but of unspecified type. Following the guide, two materials were implemented in MELCOR with respective oxides, silicon carbide, and the FeCrAl alloy. Both materials have been extensively researched for use in LWR technology plants because of their excellent oxidation resistance; faced issues and missing studies are described in the respective sections for each material. Although the data on the materials and their specific design are not complete, under estimated parameters, the materials could be implemented in MELCOR, and their properties and behaviour could be assessed under severe accident conditions. The required thermal properties of the material that were changed are described below in the following sections. The material specifics are defined in the material package (MP), the core-related properties such as weight, oxidation reaction, and oxidation kinetics are defined in core package (COR). Reaction heat with temperature dependency is in the COR package controlled by a control function (CF) that is supplied with data from precalculated tabular functions (TF).

6.3.1 Silicon Carbide

Most silicon carbide cladding designs consider the use of a multilayered fibre-winded tube instead of a monolithic design. The correlations for thermal conductivity and specific heat are listed in section 2.3.2. These correlations are applicable for the composite design with Hi-Nicalon Type-S fibres. The density of the material is 2910 kg.m^{-3} [95]. For simplification, the cladding tube is considered dense 100 %, with no porosity's or spaces between layers and individual fibres. Due to density change, the weight of cladding in each cell in core has to be recalculated with a multiplier as a ratio of SiC and Zircaloy density (MELCOR value), in eq. (6.1), geometry of the fuel rod is maintained.

$$x_{CL,CELL} = \frac{\rho_{SiC}}{\rho_{Zircaloy}} = \frac{2910}{6500} = 0,447692, \tag{6.1}$$

where $x_{CL,CELL}$ is weight of cladding in cell multiplier (-) and ρ is density (kg/m^{-3}). Molar weight of silicon carbide is 40,11 g.mol^{-1}. The melting point of silicon carbide is assumed to be 3103,15 K [96]. The thermal conductivity is calculated from eq. (2.20), the effects of heavy particle irradiation, resulting in a decrease in thermal conductivity, were neglected.

The data on enthalpy of silicon carbide were retrieved from the NIST JANAF database because data on the enthalpy of Hi-Nicalon Type-S fibres are not available. However, the values are not exact for the modelled material; there might be slight differences between the general SiC in the database and Hi-Nicalon Type S fibres. In the code, the enthalpy value at temperature is specified in J.kg^{-1}. From the melting point and higher, the value of latent heat of fusion must be added to the enthalpy value in MELCOR; typically, the reaction-bonded silicon carbide value is about 1,05.10^{6} J.kg^{-1} [97], the value was assumed slightly higher at 1,3.10^{6} J.kg^{-1}.

Following the theoretical prerequisites given in section 2.3.2, under high-temperature oxidation by steam of silicon carbide, the silicium is oxidised, resulting in the formation of SiO_2 and substituted by the release of carbon monoxide due to the oxidation of carbon in the structure.

$$SiC + 3H_2O \rightarrow SiO_2 + 3H_2 + CO \tag{6.2}$$

For calculation of oxidation kinetics, the code adopts the Arrhenius correlation. Arrhenius correlation specifies the reaction rate of a chemical reaction with temperature dependency. The modified MELCOR correlation is given in (6.3).

$$\frac{\mathrm{d}W^n}{\mathrm{d}t} = k_{p,H_2O} \cdot \exp(-\frac{E_a}{R \cdot T}), \tag{6.3}$$

where W is the mass of metal oxidized per unit surface area, k_{p,H_2O} is pre-exponential factor for water/steam containing environment in (kg^{2}.m^{-4}s^{-1}), E_a is activation energy for reaction to occur (J.mol^{-1}.K^{-1}), R is gas constant $8,314$ (J.mol^{-1}.K^{-1}), and T is the temperature of oxidised surface in (K). For silicon carbide oxidation, the following eq. (6.4) is used, based on the data given in the report [98] , and it is assumed that the reaction progresses at a parabolic rate.

$$\frac{\mathrm{d}W^1}{\mathrm{d}t} = 0,03424 \cdot \exp(-\frac{238000}{R \cdot T}) \tag{6.4}$$

For more accurate calculations, the heat that is released or absorbed during oxidation is calculated in dependence on temperature. The reaction (6.6) is exothermic. MELCOR assumes that the heat released by exothermic reactions is positive, which is different from the standard calculation of the heat of reaction using the standard enthalpies of formation, where exothermic reactions are marked by a negative sign. That is why the calculations are multiplied by (-1). The standard enthalpies of formation are assumed to not depend on pressure. Value calculated by eq. (6.6) is used for MELCOR as input; the code requires the value in kJ.kg^{-1} and not in kJ.mol^{-1}.

$$\begin{aligned} QOX_{MELCOR,SiC} = -&\Big[\Big(\Delta H^0_{SiO_2}(T) + \Delta H^0_{CO}(T)\Big) \\ &- \Big(3 \cdot \Delta H^0_{H_2O}(T) + \Delta H^0_{SiC}(T)\Big)\Big] \text{ (kJ/mol)}, \end{aligned} \tag{6.5}$$

where QOX is heat of reaction (kJ.mol^{-1}) and ΔH^0 is standart enthalpy of formation (kJ.mol^{-1}).

$$QOX_{MELCOR,SiC} = - \Big[\Big(\Delta H^0_{SiO_2}(T) + \Delta H^0_{CO}(T)\Big) - \Big(3 \cdot \Delta H^0_{H_2O}(T) + \Delta H^0_{SiC}(T)\Big)\Big] \cdot \frac{1 \cdot 10^6}{M_{SiC}} \text{ (J/kg)}, \tag{6.6}$$

where QOX is heat of reaction (J.kg^{-1}), ΔH^0 is standart enthalpy of formation (kJ.mol^{-1}) and ΔH^0 is molar weight (g.mol^{-1}).

6.3.1.1 Oxide properties

The oxide formed under high temperature and low pressure from Si is SiO_2. Data on thermal conductivity and density with temperature dependence were reported in [99]. The author experimentally recovered data on multiple SiO_2 types. The molar weight of SiO_2 is 60,09 g/mol. The melting point is assumed to be 1983,15 K [100]. Data on enthalpy and heat capacity were retrieved from the NIST JANAF database.

6.3.2 FeCrAl

Information on the thermal properties of the C35M alloy is limited; in some cases, the properties are substituted for Kanthal APMT, as this material was used multiple times to estimate properties of nuclear grade FeCrAl alloys. The melting point of 1773,15 K is assumed, the same as Kanthal APMT [101], the exact melting point of the C35M alloy is not specified by the manufacturer. The specific heat was calculated using eq. (2.5) and (2.6). The thermal conductivity correlation is specified in eq. (2.8). The material density was calculated from the composition of the alloy. The percentage of weights and the assumed density of the alloying elements are listed in tab. (6.1).

Tab. 6.1: Density of elements and weight percentage composition of C35M alloy

Alloying element	ρ (kg.m^{-3})	φ (%)
Fe	7874	80,15
Cr	7190	13
Al	2700	4,5
Mo	10280	2
Si	2330	0,2
Y	4470	0,15

$$\begin{aligned}\rho_{C35M} &= \rho_{Fe}\cdot\varphi_{Fe}+\rho_{Cr}\cdot\varphi_{Cr}+\rho_{Al}\cdot\varphi_{Al}+\rho_{Mo}\cdot\varphi_{Mo}+\rho_{Si}\cdot\varphi_{Si}+\rho_{Y}\cdot\varphi_{Y}\\ &= 7874\cdot 0,8015+7190\cdot 0,13+2700\cdot 0,045+10280\cdot 0,02+\\ &+2330\cdot 0,002+4470\cdot 0,0015\\ &= 7423,43\,\text{kg.m}^{\text{-3}},\end{aligned}\tag{6.7}$$

where ρ is the element density in (kg.m$^{\text{-3}}$) and φ is the weight percentage of element in alloy in (%). The real density may vary depending on the material structure, porosity, etc. Due to density change, the weight of cladding in each cell in core has to be recalculated with a multiplier as a ratio of C35M and Zircaloy (MELCOR value) densities, in eq. (6.8), geometry of the fuel rod is maintained.

$$x_{CL,CELL}=\frac{\rho_{C35M}}{\rho_{Zircaloy}}=\frac{7423,43}{6500}=1,142066,\tag{6.8}$$

where $x_{CL,CELL}$ is weight of cladding in cell multiplier (-) and ρ is density (kg/m$^{\text{-3}}$). The material molar weight was calculated from the material composition of the alloy and the molar weights of each of the elements. The molar weights assumed for the calculation are in tab. (6.2).

Tab. 6.2: Molar weight and weight percentage composition of C35M alloy

Alloying element	M (g.mol$^{\text{-1}}$)	φ (%)
Fe	55,85	80,15
Cr	52	13
Al	26,98	4,5
Mo	95,94	2
Si	28,09	0,2
Y	88,91	0,15

$$\begin{aligned}M_{C35M} &= M_{Fe}\cdot\varphi_{Fe}+M_{Cr}\cdot\varphi_{Cr}+M_{Al}\cdot\varphi_{Al}+\\ &+M_{Mo}\cdot\varphi_{Mo}+M_{Si}\cdot\varphi_{Si}+M_{Y}\cdot\varphi_{Y}\\ &= 55,85\cdot 0,8015+52\cdot 0,13+26,98\cdot 0,045+95,94\cdot 0,02+\\ &+28,09\cdot 0,002+88,91\cdot 0,0015\\ &= 54,84622\,\text{g.mol}^{\text{-1}},\end{aligned}\tag{6.9}$$

where M is molar weight (g.mol$^{\text{-1}}$) and φ is the weight percentage of element in alloy (%). An ideal mixture with no interactions between elements is assumed; the real molar weight of an alloy would also depend on its structure and other factors.

The enthalpy of the alloy is weighted from the material composition and the enthalpies of each respective element, except yttrium, as there are no available data in the NIST JANAF database. The following eq. (6.10) is used for the calculation of the enthalpy with temperature dependency, and the pressure dependency is neglected. The value of latent heat of fusion (LHF), in eq. (6.11), must be added to the enthalpy values above the melting point, value of LHF for elements were retrieved from [102].

$$\begin{aligned} H_{C35M}(T) = H_{Fe}(T) \cdot \varphi_{Fe} + H_{Cr}(T) \cdot \varphi_{Cr} + H_{Al}(T) \cdot \varphi_{Al} + \\ + H_{Mo}(T) \cdot \varphi_{Mo} + H_{Si}(T) \cdot \varphi_{Si} \end{aligned} \tag{6.10}$$

where H is the enthalpy (J.kg^{-1}) and φ is the weight percentage of element in alloy (%).

$$\begin{aligned} LHF_{C35M} &= LHF_{Fe} \cdot \varphi_{Fe} + LHF_{Cr} \cdot \varphi_{Cr} + LHF_{Al} \cdot \varphi_{Al} + \\ &+ LHF_{Mo} \cdot \varphi_{Mo} + LHF_{Si} \cdot \varphi_{Si} \\ &= 247000 \cdot 0,8015 + 394000 \cdot 0,13 + 396000 \cdot 0,045 + \\ &+ 375000 \cdot 0,02 + 1787000 \cdot 0,002 \\ &= 278084,5 \text{ J.kg}^{-1} \end{aligned} \tag{6.11}$$

where LHF is latent heat of fusion (J.kg^{-1}) and φ is the weight percentage of element in alloy (%). Even though the following equations are balanced to not contain fractions, such input in MELCOR would not work because all reactions specified in the code have to be based on the reaction of one mole of the metal. The code allows only the implementation of only three reaction equations, because of that, only iron, chromium, and aluminium are considered for oxidation, such an approach is also supported by research on the oxidation of FeCrAl alloys in high-temperature steam [103]. The MELCOR does not treat each oxide separately; instead it forms a mixture of oxides (generic oxide) based on the user input; that is why the thermal properties of individual oxides have to be combined using weighting, which estimates the properties of a generic oxide formed.

$$3Fe + 4H_2O \rightarrow Fe_3O_4 + 4H_2 \tag{6.12}$$

$$2Cr + 3H_2O \rightarrow Cr_2O_3 + 3H_2 \tag{6.13}$$

$$2Al + 3H_2O \rightarrow Al_2O_3 + 3H_2 \tag{6.14}$$

For the oxidation kinetics of the C35M alloy, the following eq. (6.15) is used, based on the values given in the report [98], and it is assumed that the reaction progresses at a parabolic rate. The values given do not explicitly represent the oxidation rate of the C35M alloy as such information is not available; however, the values for the calculation of oxidation were substituted with the Kanthal APMT alloy, providing an estimated behaviour of FeCrAl alloys during oxidation. Kanthal APMT is not a nuclear-grade material; nuclear-grade FeCrAl alloys, which have optimised microstructure and composition, may behave differently under high-temperature steam oxidation.

$$\frac{\mathrm{d}W^2}{\mathrm{d}t} = 0,5231 \cdot \exp(-\frac{260000}{R \cdot T}), \tag{6.15}$$

To increase the accuracy, the heat that is released or absorbed during oxidation is calculated in dependence on temperature. All reactions (6.19), (6.20), (6.21) are exothermic. For simplified calculation of reaction heat dependent on temperature, the reactions with fractions were assumed. The heat of reaction is in general referred in kJ.mol^{-1}, however the MELCOR requires these values to be in J.kg^{-1}.

$$QOX_{MELCOR,Fe} = -\left(\frac{1}{3} \cdot \Delta H^0_{Fe_3O_4}(T) - \frac{4}{3} \cdot \Delta H^0_{H_2O}(T)\right) \qquad \text{(kJ/mol)}, \tag{6.16}$$

$$QOX_{MELCOR,Cr} = -\left(\frac{1}{2} \cdot \Delta H^0_{Cr_2O_3}(T) - \frac{3}{2} \cdot \Delta H^0_{H_2O}(T)\right) \qquad \text{(kJ/mol)}, \tag{6.17}$$

$$QOX_{MELCOR,Al} = -\left(\frac{1}{2} \cdot \Delta H^0_{Fe_3O_4}(T) - \frac{3}{2} \cdot \Delta H^0_{H_2O}(T)\right) \qquad \text{(kJ/mol)}, \tag{6.18}$$

where QOX is heat of reaction (kJ.mol^{-1}) and ΔH^0 is standart enthalpy of formation (kJ.mol^{-1}).

$$QOX_{MELCOR,Fe} = -\left(\frac{1}{3} \cdot \Delta H^0_{Fe_3O_4}(T) - \frac{4}{3} \cdot \Delta H^0_{H_2O}(T)\right) \cdot \frac{10^6}{M_{Fe}} \quad \text{(J/kg)}, \tag{6.19}$$

$$QOX_{MELCOR,Cr} = -\left(\frac{1}{2} \cdot \Delta H^0_{Fe_2O_3}(T) - \frac{3}{2} \cdot \Delta H^0_{H_2O}(T)\right) \cdot \frac{10^6}{M_{Cr}} \quad \text{(J/kg)}, \tag{6.20}$$

$$QOX_{MELCOR,Al} = -\left(\frac{1}{2} \cdot \Delta H^0_{Fe_3O_4}(T) - \frac{3}{2} \cdot \Delta H^0_{H_2O}(T)\right) \cdot \frac{10^6}{M_{Al}} \quad \text{(J/kg)}, \tag{6.21}$$

where QOX is heat of reaction (J.kg^{-1}), ΔH^0 is standart enthalpy of formation (kJ.mol^{-1}) and M is molar weight (g.mol^{-1}).

6.3.2.1 Oxide properties

For investigation and basic setup, the composition of oxide is considered to be with respect to material composition. The molybdenum, silicium and yttrium contents were neglected for oxidation because of their low percentage in composition and the nonallowance for such an implementation from MELCOR. The oxide is primarily consisting of Fe_3O_4 that has thermal conductivity of 3,5 W.m^{-1}.K^{-1} [104], the overall thermal conductivity of the oxide under the weighted approach would be closer to the one Fe_3O_4 even thought the thermal conductivity of Cr_2O_3 and Al_2O_3 are higher. The value of 4 W.m^{-1}.K^{-1} was adopted and is considered constant. The theoretical density of the generic oxide mixture is calculated in eq. (6.22) with data from [105–107]. The molar weight of the generic oxide formed would be 209,935 g.mol^{-1}, in eq. (6.23).

$$\begin{aligned}\rho_{C35M,oxide} &= \rho_{Fe_3O_4} \cdot \varphi_{Fe} + \rho_{Cr_2O_3} \cdot \varphi_{Cr} + \rho_{Al_2O_3}(T) \cdot \varphi_{Al} \\ &= 5170 \cdot 0,8015 + 5220 \cdot 0,13 + 3990 \cdot 0,045 \\ &= 5001,9 \text{ kg.m}^{-3},\end{aligned} \tag{6.22}$$

where ρ is the oxide density (kg.m^{-3}) and φ is the weight percentage of element in alloy (%).

$$\begin{aligned}M_{C35M,oxide} &= M_{Fe_3O_4} \cdot \varphi_{Fe} + M_{Cr_2O_3} \cdot \varphi_{Cr} + M_{Al_2O_3} \cdot \varphi_{Al} \\ &= 231,55 \cdot 0,8015 + 152 \cdot 0,13 + 101,96 \cdot 0,045 \\ &= 209,935 \text{ g.mol}^{-1},\end{aligned} \tag{6.23}$$

where M is the molar weight (g.mol^{-1}) and φ is the weight percentage of element in alloy (%). Melting point of 1901 K was adopted for the generic oxide, which is slightly higher than the one of Fe_3O_4, although the value respects the higher melting point of chromia and alumina contents. Specific heat (6.24), enthalpy (6.25), and latent heat of fusion (6.26) are calculated using the elemental alloy composition and data for each oxide from the NIST JANAF database, except for latent heat of fusion, for which data from [105, 106, 108] were used.

$$c_{p,ox} = c_{p,Fe_3O_4}(T) \cdot \varphi_{Fe} + M_{Cr_2O_3}(T) \cdot \varphi_{Cr} + M_{Al_2O_3}(T) \cdot \varphi_{Al} \text{ (J.kg}^{-1}\text{.K}^{-1}\text{)}, \tag{6.24}$$

where c_p is heat capacity (J.kg^{-1}.K^{-1}) and φ is the weight percentage of element in alloy (%).

$$H_{ox} = H_{Fe_3O_4}(T) \cdot \varphi_{Fe} + H_{Cr_2O_3}(T) \cdot \varphi_{Cr} + H_{Al_2O_3}(T) \cdot \varphi_{Al} \text{ (J.kg}^{-1}\text{)}, \tag{6.25}$$

where H is enthalpy (J.kg^{-1}) and φ is the weight percentage of element in alloy (%).

$$\begin{aligned}LHF_{ox} &= LHF_{Fe_3O_4} \cdot \varphi_{Fe} + LHF_{Cr_2O_3} \cdot \varphi_{Cr} + LHF_{Al_2O_3} \cdot \varphi_{Al} \\ &= 596000 \cdot 0,8015 + 855300 \cdot 0,13 + 1093000 \cdot 0,045 \\ &= 638068 \text{ J.kg}^{-1},\end{aligned} \tag{6.26}$$

where LHF is latent heat of fusion (J.kg^{-1}) and φ is the weight percentage of element in alloy (%).

6.3.3 FeCrAl with adjusted geometry

FeCrAl alloys exhibit about 10 times higher thermal neutron absorption cross section than traditional zirconium alloys, but as these alloys also exhibit improved overall strength, it is possible to reduce the cladding thickness. Such a reduction would not be sufficient and the enrichment of the fuel over 5 % would be necessary. Thickness reduction would allow for slightly larger fuel pellets in diameter, increasing the overall amount of fuel in the core. From the research [109], equation (6.27) could be derived. The equation was used for a recalculation of the thickness of the cladding for this simulation case using MELCOR; the dimensions of the geometry considered are shown in fig. 6.3. Only the thickness reduction was considered with all the dimensional factors that have changed due to different geometry, the core power level was maintained. The gap remained the same, to not hinder its thermal conductivity and the volume of gas. The material and oxide properties were set to the same as those for the FeCrAl weighted approach.

$$\delta_{FCA} = \delta_{ZRY}^{ACTOF} \cdot \frac{\delta_{FCA}^{ACTOF}}{\delta_{ZRY}^{ACTOF}} = 0,57145 \cdot \frac{0,385}{0,575} = 0,382623\,\mathrm{mm}, \tag{6.27}$$

where δ is cladding thickness (mm). Due to a change in geometry, a cross-sectional area, the outer surface area of the pellet, and the cross-sectional area of the cladding were calculated. The calculations are taken in eq. (6.28) to (6.33). The length of the fuel rods remained the same. Lower index 1 marks the original geometry and index 2 marks the adjusted geometry.

$$S_{FP1} = \pi \cdot r_{FP1}^2 = \pi \cdot 4,096^2 = 52,70717953\,\mathrm{mm}^2, \tag{6.28}$$

where S_{FP1} is fuel pellet cross-sectional area (mm^2) and r_{FP1} is fuel pellet radius (mm).

$$S_{FP1,surface} = 2\pi \cdot r_{FP1} \cdot l = 2\pi \cdot 4,096 \cdot l = 25,73592702 \cdot l\,\mathrm{mm}^2, \tag{6.29}$$

where $S_{FP1,surface}$ is fuel pellet surface area (mm^2) and r_{FP1} is fuel pellet radius (mm).

$$\begin{aligned} S_{CL1} &= \pi \cdot \left(R_{CL1}^2 - r_{CL1}^2\right) \\ &= \pi \cdot \left(4,75^2 - (4,75 - 0,57145)^2\right) = 16,02909655\,\mathrm{mm}^2, \end{aligned} \tag{6.30}$$

where S_{CL1} is cladding cross-sectional area (mm^2), R_{FP1} is cladding outer radius (mm) and r_{FP1} is cladding inner radius (mm).

$$S_{FP2} = \pi \cdot r_{FP2}^2 = \pi \cdot 4,284827^2 = 57,67883191\,\mathrm{mm}^2, \tag{6.31}$$

where S_{FP2} is fuel pellet cross-sectional area (mm^2) and r_{FP2} is fuel pellet radius (mm).

$$S_{FP2,surface} = 2\pi \cdot r_{FP2} \cdot l = 2\pi \cdot 4,284827 \cdot l = 26,92236205 \cdot l\,\mathrm{mm}^2, \tag{6.32}$$

where $S_{FP2,surface}$ is fuel pellet surface area (mm^2) and r_{FP2} is fuel pellet radius (mm).

$$\begin{aligned} S_{CL2} &= \pi \cdot \left(R_{CL2}^2 - r_{CL2}^2\right) \\ &= \pi \cdot \left(4,75^2 - (4,75 - 0,382623)^2\right) = 10,95950296\,\text{mm}^2, \end{aligned} \tag{6.33}$$

where S_{CL2} is cladding cross-sectional area (mm^2), R_{FP2} is cladding outer radius (mm) and r_{FP2} is cladding inner radius (mm). In eq. (6.34) the fuel weight factor multiplier was determined from the fuel cross sectional areas, the fuel density and length of fuel rods remained unchanged. The multiplier would thus be defined as a ratio between cross-sectional areas. There is approximately 9,4 % more fuel loaded in the core.

$$\begin{aligned} x_{FU} \cdot m_{FU1} &= m_{FU2} \\ x_{FU} \cdot \rho_{FU} \cdot V_{FU1} &= \rho_{FU} \cdot V_{FU2} \\ x_{FU} \cdot \rho_{FU} \cdot l \cdot S_{FP1} &= \rho_{FU} \cdot l \cdot S_{FP2} \\ x_{FU} &= \frac{S_{FP2}}{S_{FP1}} = \frac{57,67883191}{52,70717953} = 1,094325925, \end{aligned} \tag{6.34}$$

where x_{FU} is weight of fuel multiplier (-), m_{FU} is weight of fuel (kg), ρ_{FU} is fuel density (kg.m^{-3}), V_{FU} are fuel volumes (m^3), l is fuel rod length (mm) and S_{FP} are fuel pellet surface areas (mm^2). In eq. (6.35) the fuel surface area factor multiplier was calculated from the fuel pellet outer surface areas. The multiplier would be defined as the ratio between these areas. The area has an impact on the heat transfer between the fuel pellets and the cladding. The surface area of the fuel pellet with adjusted geometry is roughly 4,6 % larger.

$$\begin{aligned} x_{FU,surface} \cdot S_{FP1,surface} &= S_{FP2,surface} \\ x_{FU,surface} &= \frac{S_{FP2,surface}}{S_{FP1,surface}} = \frac{26,92236205 \cdot l}{25,73592702 \cdot l} = 1,046100342, \end{aligned} \tag{6.35}$$

where $x_{FU,surface}$ is fuel surface area multiplier (-) and S_{FP} are fuel pellet surface areas (mm^2). In eq. (6.36) the cladding weight factor was determined from the cross-sectional areas of the cladding, the density of the cladding and the length of the fuel rods remained unchanged. The multiplier would thus be defined as a ratio between cross-sectional areas. The weight of the cladding is reduced by almost one-third from the original geometry.

$$\begin{aligned} x_{CL} \cdot m_{CL1} &= m_{CL2} \\ x_{CL} \cdot \rho_{CL} \cdot V_{CL1} &= \rho_{CL} \cdot V_{CL2} \\ x_{CL} \cdot \rho_{CL} \cdot l \cdot S_{CL1} &= \rho_{CL} \cdot l \cdot S_{CL2} \\ x_{CL} &= \frac{S_{CL2}}{S_{CL1}} = \frac{10,959502961}{16,02909655} = 0,6837255566, \end{aligned} \tag{6.36}$$

where x_{CL} is weight of cladding multiplier (-), m_{CL} is weight of cladding (kg), ρ_{CL} is cladding density (kg.m^{-3}), V_{CL} are cladding volumes (m^3), l is fuel rod length (mm) and S_{CL} are fuel pellet surface areas (mm^2).

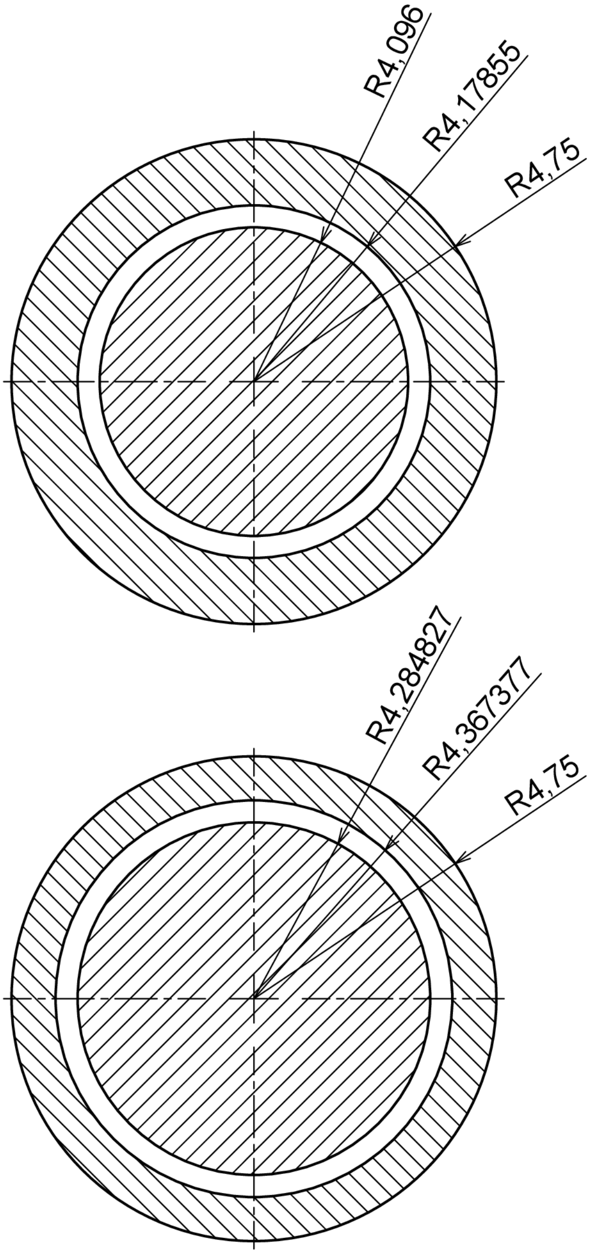
R4,096
R4,17855
R4,75
R4,284827
R4,367377
R4,75

Fig. 6.3: Adjusted geometry of fuel rod with FeCrAl cladding; top - original dimensions, bottom - adjusted dimensions; dimensions are not proportional, in mm

6.3.4 Sensitivity study on oxide formation

The sensitivity study is based on research [103] on advanced steels, FeCrAl alloys. The researchers demonstrated that the oxide layer formed on the surface of the oxidised alloy is mainly composed of aluminium oxide, ranging from 60 to 90 %, depending on the time of oxidation and temperature. Thus, the composition of resulting oxides formed on the surface is not in respect of oxidising elements. Following acquired information, the generic oxide formed under oxidation modelling would have thermophysical properties close to those of aluminium oxide. In total, seven different oxide compositions were implemented by calculation of their thermal properties; the compositions are listed in the tab. (6.3).

Tab. 6.3: Weight percentage composition of oxides considered for sensitivity study

Al_2O_3 (wt.%)	Cr_2O_3 (wt.%)	Fe_3O_4 (wt.%)
60	5	35
60	10	30
70	5	25
70	10	20
80	5	15
80	10	10
90	5	5

The thermal conductivity of the resulting oxide (6.37) would be closer to that of aluminium oxide, the thermal conductivity of Fe_3O_4 is assumed at constant 3,5 $W.m^{-1}.K^{-1}$ [104], Cr_2O_3 is assumed at constant 9,99 $W.m^{-1}.K^{-1}$ [110], and thermal conductivity of aluminium oxide was considered with temperature dependency, data were retrieved from [111].

The density of oxides is determined using (6.38). The density values of each oxide were previously mentioned. The molar weight of a generic oxide is calculated by (6.39). The melting point of the specified oxide composition is calculated with (6.40), however, such an approach may not be completely accurate, as many other factors have an impact on the melting point, the calculation gives an estimate. In addition, the specific heat (6.41), the enthalpy (6.42), and the latent heat of fusion (6.43) were estimated using the composition and thermal properties data that were previously introduced. The estimated values may not be absolutely accurate, as other factors such as gas diffusion into the layer, porosities, etc. result in changes in properties.

$$k = k_{Fe_3O_4} \cdot \varphi_{Fe_3O_4} + k_{Cr_2O_3} \cdot \varphi_{Cr_2O_3} + k_{Al_2O_3}(T) \cdot \varphi_{Al_2O_3} \quad (\mathrm{W.m^{-1}.K^{-1}}), \qquad (6.37)$$

where k_T is thermal conductivity (W/m.K) and φ is the weight percentage of oxide in composition (%).

$$\rho_{SENS} = \rho_{Fe_3O_4} \cdot \varphi_{Fe_3O_4} + \rho_{Cr_2O_3} \cdot \varphi_{Cr_2O_3} + \rho_{Al_2O_3}(T) \cdot \varphi_{Al_2O_3} \text{ (kg.m}^{-3}\text{)}, \tag{6.38}$$

where ρ is the oxide density (kg.m^{-3}) and φ is the weight percentage of oxide in composition (%).

$$M_{SENS} = M_{Fe_3O_4} \cdot \varphi_{Fe_3O_4} + M_{Cr_2O_3} \cdot \varphi_{Cr_2O_3} + M_{Al_2O_3} \cdot \varphi_{Al_2O_3} \text{ (g.mol}^{-1}\text{)}, \tag{6.39}$$

where M is the molar weight (g.mol^{-1}) and φ is the weight percentage of oxide in composition (%).

$$T_{mSENS} = T_{mFe_3O_4} \cdot \varphi_{Fe_3O_4} + T_{mCr_2O_3} \cdot \varphi_{Cr_2O_3} + T_{mAl_2O_3} \cdot \varphi_{Al_2O_3} \text{ K}, \tag{6.40}$$

where T_m is the melting point (g.mol^{-1}) and φ is the weight percentage of oxide in composition (%).

$$c_{p,SENS} = c_{p,Fe_3O_4}(T) \cdot \varphi_{Fe_3O_4} + M_{Cr_2O_3}(T) \cdot \varphi_{Cr_2O_3} + M_{Al_2O_3}(T) \cdot \varphi_{Al_2O_3} \text{ (J.kg}^{-1}\text{.K}^{-1}\text{)}, \tag{6.41}$$

where c_p is heat capacity (J.kg^{-1}.K^{-1}) and φ is the weight percentage of oxide in composition (%).

$$H_{SENS} = H_{Fe_3O_4}(T) \cdot \varphi_{Fe_3O_4} + H_{Cr_2O_3}(T) \cdot \varphi_{Cr_2O_3} + H_{Al_2O_3}(T) \cdot \varphi_{Al_2O_3} \text{ (J.kg}^{-1}\text{)}, \tag{6.42}$$

where H is enthalpy (J.kg^{-1}) and φ is the weight percentage of oxide in composition (%).

$$LHF_{SENS} = LHF_{Fe_3O_4} \cdot \varphi_{Fe_3O_4} + LHF_{Cr_2O_3} \cdot \varphi_{Cr_2O_3} + LHF_{Al_2O_3} \cdot \varphi_{Al_2O_3} \text{ (J.kg}^{-1}\text{)}, \tag{6.43}$$

where LHF is latent heat of fusion (J.kg^{-1}) and φ is the weight percentage of oxide in composition (%).

7 Simulation evaluation

This chapter discusses the results derived from simulations of advanced cladding materials that are compared to Zircaloy model available in MELCOR. Each scenario is described in its respective section on the phenomenon occurring at time and its impact on the system.

7.1 Unmitigated LB LOCA

Large break LOCA is initiated by a guillotine break of the cold leg. Rapid depressurisation of the RCS occurs, the core water level drops significantly in first few seconds after break occurs, which could be observed in fig. 7.1. The core is quickly refilled by injected water from SIT in the fluidic device's high-flow regime. At 37 seconds, the fluidic device switches to low-flow regime, which leads again to core uncovery as there is still a substantial amount of heat produced in the core. The injected water in low-flow regime initially boils out quickly but also removes the heat from the core, cooling it down and is eventually able to refill the core.

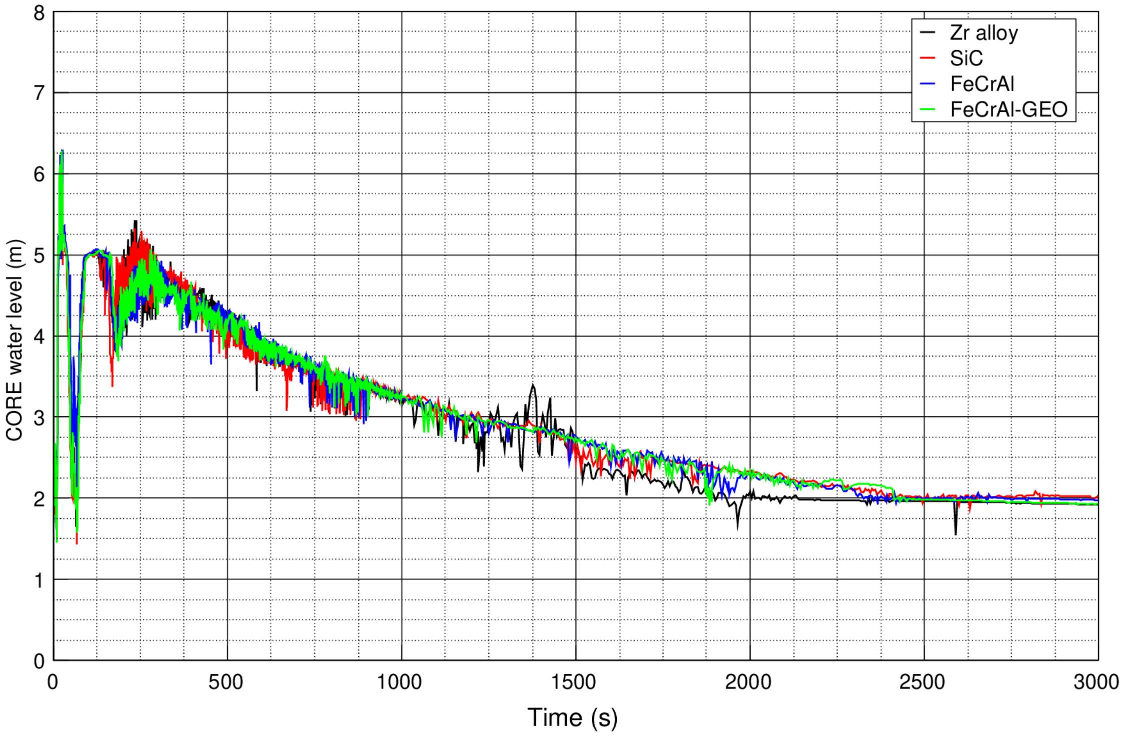

Fig. 7.1: CORE water level - unmitigated LB LOCA

The temperature of the fuel rods increases rapidly as a result of the decay heat and no cooling, first peaks in fig. 7.2. The core water level is partially restored from the SIT, reducing the temperature of the fuel rods. After 160 seconds, the volume of SITs is depleted and SIPs are unavailable for the core reflood phase. Injected water evaporates and core water level decreases again, consequently the temperature of cladding rises again. As the surface temperature exceeds 1100 K (Zircaloy and FeCrAl) and 1373,15 K (SiC), the cladding oxidation occurs. The oxidation kinetics of FeCrAl and SiC is considerably slower, resulting in lower amount of heat released by oxidation, temperature increase is primarily driven by the decay heat. Zircaloy degrades faster and oxidation progresses rapidly, while more heat is released (the difference is observable in fig. 7.3), combined with decay heat, causing an increased rate of temperature rise compared to advanced cladding materials (an increase in the rate could be observed at time greater than 1000 seconds in fig. 7.2). The heat released as a result of oxidation affects the rate of core water level decrease; the lower the heat released, the rate decreases. It is observable at times over 1500 seconds in fig. 7.1, where the core is fully uncovered at 2000 seconds in case of Zircaloy, and later on at about 2300 seconds the core is almost fully uncovered in case of advanced cladding materials. The water level drops to 2 metres eventually, but the core is fully uncovered at this water level, the additional 2 metres of water are from the volume of lower plenum which is modelled together with the core.

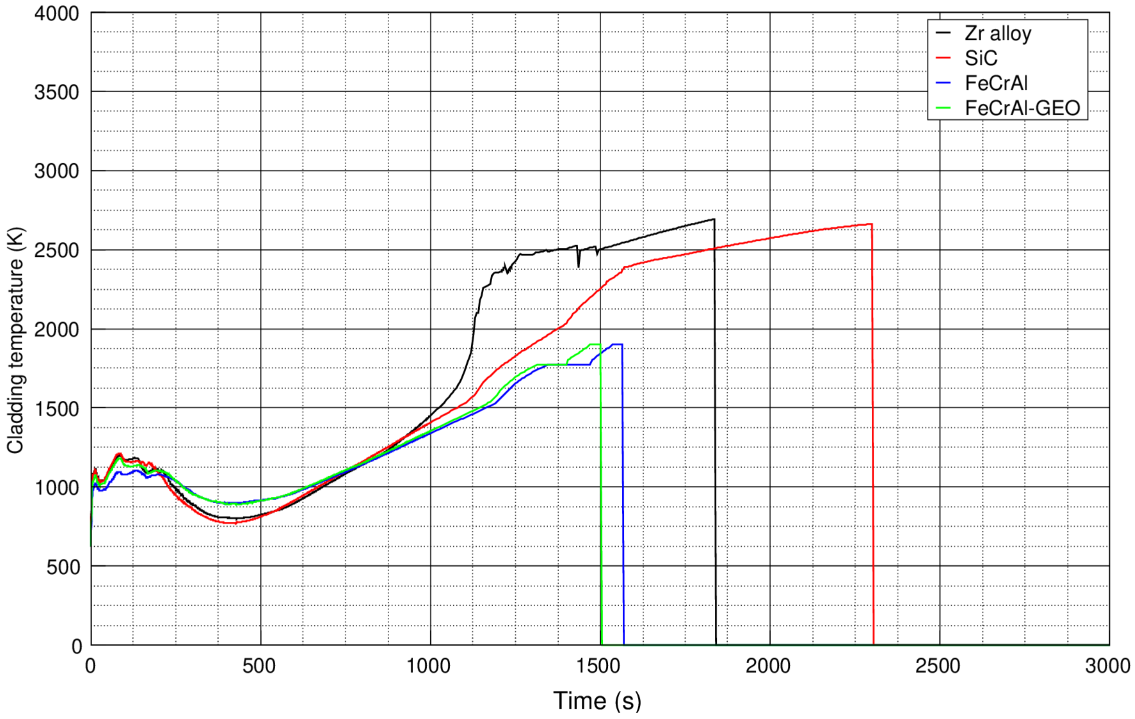

Fig. 7.2: Cladding temperature in cell 213 - unmitigated LB LOCA

As a result of the lower melting point of FeCrAl, the fuel rods fail earlier compared to that of Zircaloy. FeCrAl cladding with an adjusted geometry fails even sooner due to reduced thickness. In contrast, SiC cladding fails the latest, as it has a high melting point and high thermal conductivity. In addition, during simulations in MELCOR, the fuel inside the rods melted before the SiC cladding was even melted; the MELCOR recognises this and eventually marks the cell as failed due to damage function.

Cell IR2, IA13, is not necessarily the first to fail in simulations for all cases, the cell was selected because the impact of the oxidation heat is easily observable. Whether the cell failure occurs in MELCOR, the failed material is transferred to particulate debris. The same happens to all cells above the one that has failed. So not all cells have to be melted to be considered as failed. This is because the integrity of the failed cell is compromised and the cells above are not supported.

In fig. 7.3, the total cumulative hydrogen produced by the oxidation of the vessel components is shown. For both FeCrAl and SiC, a considerably lower amount of hydrogen is released compared to that of the case in which Zircaloy was used. The difference is caused by the amount of hydrogen produced by cladding oxidation. FeCrAl cladding with an adjusted geometry is initially oxidised more than that of the one with an unchanged geometry because the surface temperature for oxidation was exceeded earlier.

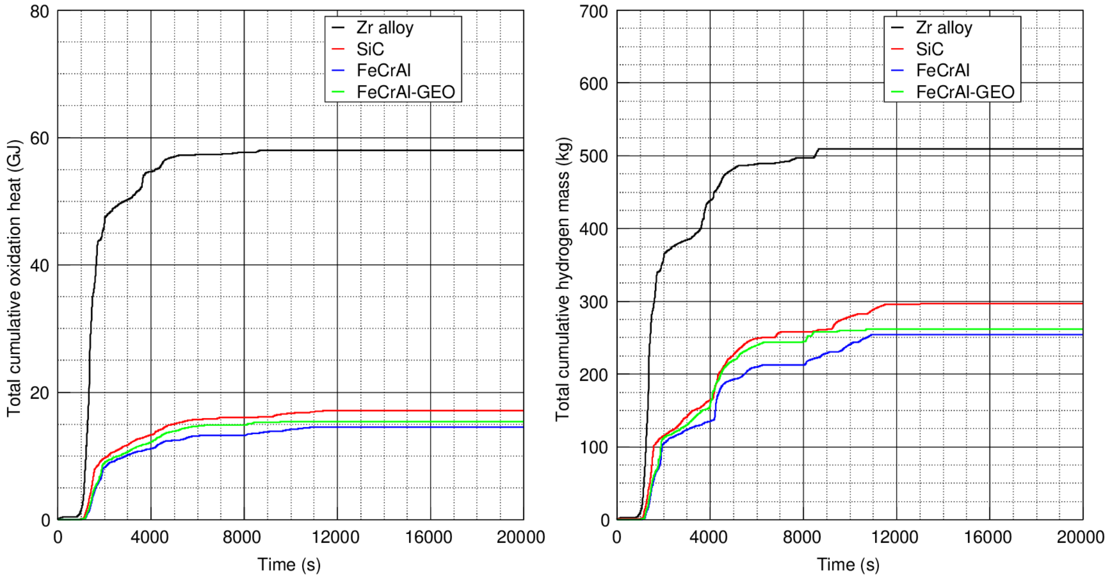

Fig. 7.3: Total cumulative heat and hydrogen produced due to in-vessel oxidation of components - unmitigated LB LOCA

The increase in hydrogen released at about 4000 seconds is caused by the drop of molten corium into the lower plenum after the support plate has failed. There is still water in the lower plenum that immediately evaporates, and the vapour released further oxidises structures not yet melted. Furthermore, in the case of an adjusted FeCrAl geometry, a higher amount of fuel is loaded into the core, and the total mass of corium would be higher. Higher mass means more energy accumulated in the system; when the mass is dropped into the lower plenum to the water, more energy is transferred, increasing the vapour temperature, and more energy is also transferred from corium to the RPV, heating it up, increasing the rate for oxidation. The increased rate leads to a higher amount of cumulative heat and hydrogen produced by oxidation.

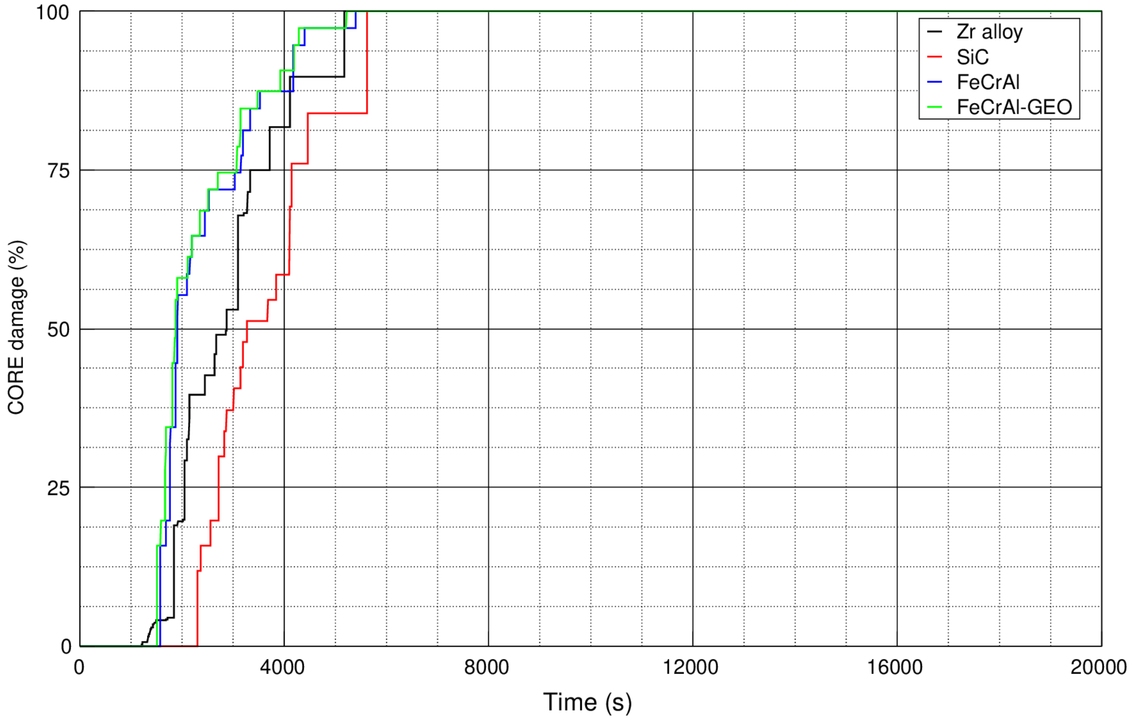

Fig. 7.4: CORE damage - unmitigated LB LOCA

In fig. 7.4 the percentual core damage is shown. Core damage occurs upon candling of the cladding. Candling occurs when the melting point of the cladding material is reached and its surface partially melts, but the integrity is still maintained. This happens in case of Zircaloy at the time about 1200 seconds. The core damage in the case of FeCrAl progresses at a faster rate because of its lower melting point. In the case of SiC, its higher melting point leads to the latest time of the first core damage; the progression rate of core damage is comparable to the one of Zircaloy. Total core damage (100 %)is achieved when all corium, which contains fuel, cladding, support and non-support structures, melts through the support plate and relocates to the lower plenum of RPV.

The results of unmitigated LB LOCA with conventional Zircaloy, SiC, FeCrAl and FeCrAl with adjusted geometry are listed in tab. 7.1. The total cumulative heat and hydrogen produced as a result of in-vessel oxidation of the components have been significantly reduced by the use of advanced cladding materials. Failures of the RPV occurred later when SiC and FeCrAl were used, SiC maintained its structural integrity for a longer period because of its high melting point, FeCrAl alloy melts sooner when the fuel pellets are not yet melted, and pellet melting occurs on the support plate and in the lower plenum, respectively. The masses of carbon monoxide and dioxide released are dependent on the failure od RPV and resulting molten corium concrete interaction in the cavity.

Tab. 7.1: Results of unmitigated LB LOCA

	Zr alloy	SiC	FeCrAl	FeCrAl-GEO
Total cumulative oxidation heat (GJ)	57,96	17,14	14,52	15,41
Total cumulative hydrogen mass (kg)	509,1	296,4	254,30	262,1
Carbon monoxide (kg)	114,55	91,37	79,72	82,69
Carbon dioxide (kg)	30,72	69,53	85,44	80,78
Hydrogen by cladding oxidation (kg)	324,4	1,785	3,274	2,728
Time to first cladding failure (s)	~1835	~2301	~1567	~1501
Time to RPV failure (s)	~8435	~9203	~9508	~9423

7.2 Unmitigated LB LOCA - Sensitivity study

The sensitivity study was conducted to analyse upon a sensitivity of formation of FeCrAl oxides based on their composition in MELCOR. The same oxidation kinetics was considered for all cases of FeCrAl, but for the sensitivity study, it was adjusted to the weight percentage of the individual oxides formed in the generic oxide and not by the alloy composition.

In general, the formation of aluminium oxide on the surface protects the material from further oxidation. Chromium oxide stabilises the layer of aluminium oxide and prevents the oxide from breaking down. However, in MELCOR the layers are not formed, the principle of multiple layers of different oxides is currently not achievable, and the generic oxide formed would behave differently. In following plots and results in tab. 7.2 7.3, the legend marks each case based on its oxide composition, e.g., case 60-5-35 considers the oxide with 60 % Al_2O_3, 5% Cr_2O_3 and 35 % Fe_3O_4. The cases are described in detail in section 6.3.4.

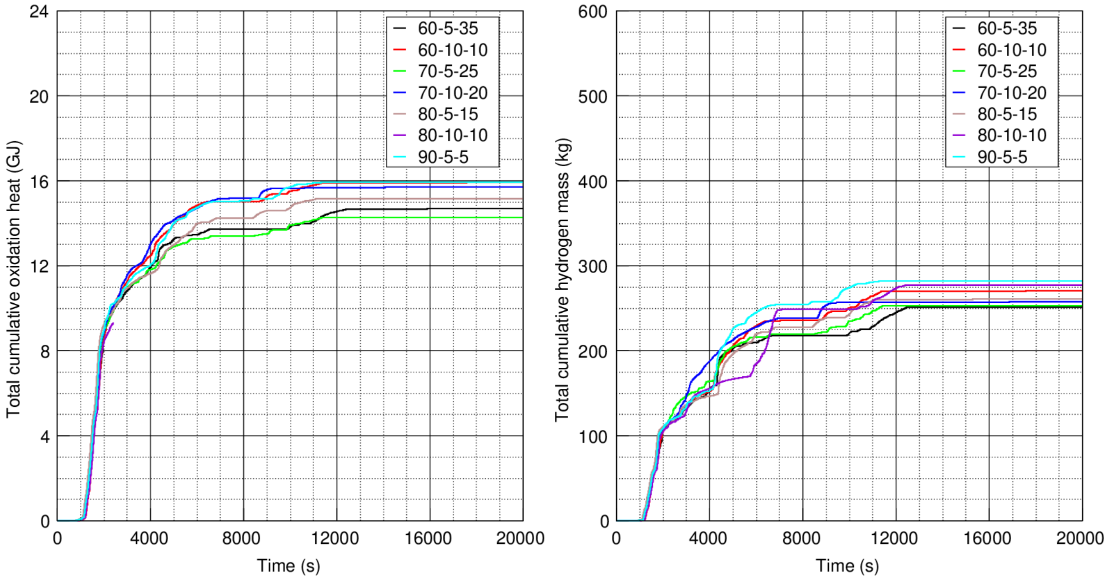

Fig. 7.5: Total cumulative heat and hydrogen produced due to in-vessel oxidation of components - unmitigated LB LOCA - sensitivity study

Aluminium oxide has a melting point higher than that of ferrous ferric oxide. The higher melting point combined with the higher conductivity should prolong the period before the cladding fails. Although the conductivity and melting point increase with the larger proportion of aluminium oxide, aluminium oxidation also releases the highest amount of heat from the reaction. The cumulative amounts of heat and hydrogen produced are shown in fig. 7.5, the cladding temperatures in cell 213 are shown fig. 7.6.

For example the composition 80-5-15, the heat produced by oxidation is slightly lower than for other compositions while the conductivity is decreased due to iron oxide in the composition, but the failure of the cladding time is the latest, as the melting point is close to the one of aluminium oxide. On the other hand, composition 60-5-35 exhibits the earliest failure time of the cladding. Although the heat produced by oxidation is even lower than in the case of 80-5-15, the melting point and conductivity are greatly influenced by the iron oxide in the composition.

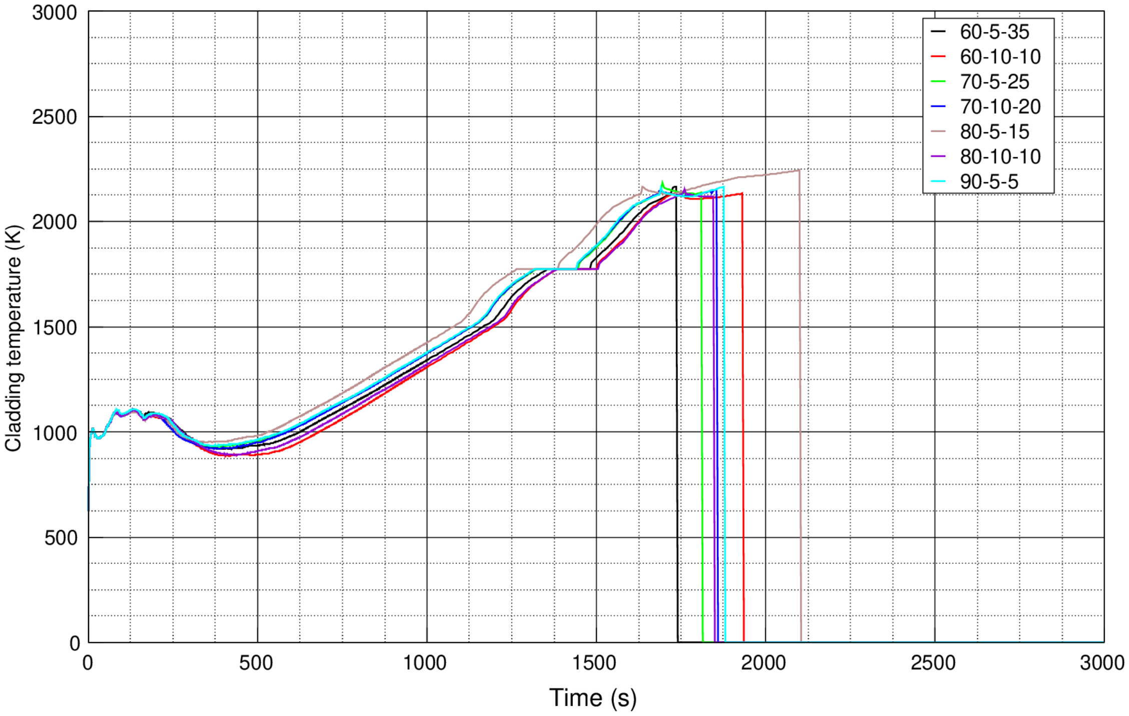

Fig. 7.6: Cladding temperature in cell 213 - unmitigated LB LOCA - sensitivity study

The overall results of the simulations are listed in tab. 7.2 and 7.3. The numbers in the header specify the composition of the generic oxide. In case of oxidation heat, there is a trend of more heat released with more aluminium oxide in the composition, and the same applies to the cumulative amount of hydrogen mass released. In all sensitivity study cases, the amount of hydrogen produced by cladding oxidation is dramatically lower than that produced by Zircaloy. The missing value of oxidation heat for 80-10-10 is caused by an error in variables plotting by MELCOR, multiple simulations were trialled to recover the error, without success.

Tab. 7.2: Results of unmitigated LB LOCA - sensitivity study 1/2

	60-5-35	60-10-30	70-5-25	70-10-20
Total cumulative oxidation heat (GJ)	14,69	15,94	14,29	15,71
Total cumulative hydrogen mass (kg)	251,5	271,1	253	257,4
Carbon monoxide (kg)	86,24	87,14	88,04	88,81
Carbon dioxide (kg)	75,23	73,78	72,37	71,16
Hydrogen by cladding oxidation (kg)	2,365	7,658	1,653	3,218
Time to first cladding failure (s)	∼1738	∼1930	∼1813	∼1856
Time to RPV failure (s)	∼10854	∼9826	∼9826	∼8631

Tab. 7.3: Results of unmitigated LB LOCA - sensitivity study 2/2

	80-5-15	80-10-10	90-5-5
Total cumulative oxidation heat (GJ)	15,15	-	15,93
Total cumulative hydrogen mass (kg)	260,8	277,6	282,5
Carbon monoxide (kg)	87,13	87,110	89,31
Carbon dioxide (kg)	73,81	73,84	70,38
Hydrogen by cladding oxidation (kg)	4,148	1,613	3,363
Time to first cladding failure (s)	∼2100	∼1846	∼1877
Time to RPV failure (s)	∼9802	∼10267	∼9503

7.3 Station blackout

The FeCrAl alloy simulation results are not included for SBO. The simulations have been collapsing even at small time steps on mass and energy errors. Following the MELCOR user guide and error message reports, these errors indicated that the relative mass and energy errors were exceeded, not to hinder the accuracy and relevancy of simulations and retrievable results, MELCOR automatically stops the calculation. Particular errors have been related to the enthalpies of the C35M alloy implemented and its generic oxide. Under LOCA, the event progresses faster, and the oxidation is not that severe, so relative errors could not reach that high as during SBO. The SBO is slower; as a result of prolonged oxidation, relative errors could increase. One of the solutions would be to experimentally obtain data on the enthalpy and latent heat of fusion of the C35M alloy and the oxides that are formed in a high temperature steam environment.

7.3.1 Station blackout - total loss of power

The station blackout with total loss of power leads to steam generator dryout and loss of ultimate heat sink. As the heat sink is lost, the pressure and temperature in RCS increases due to decay heat. The pressure is relieved by opening the POSRV. But because there is no making up on the core water level, it decreases, exposing the core. The decrease in water level due to depressurisation is evident in fig. 7.7.

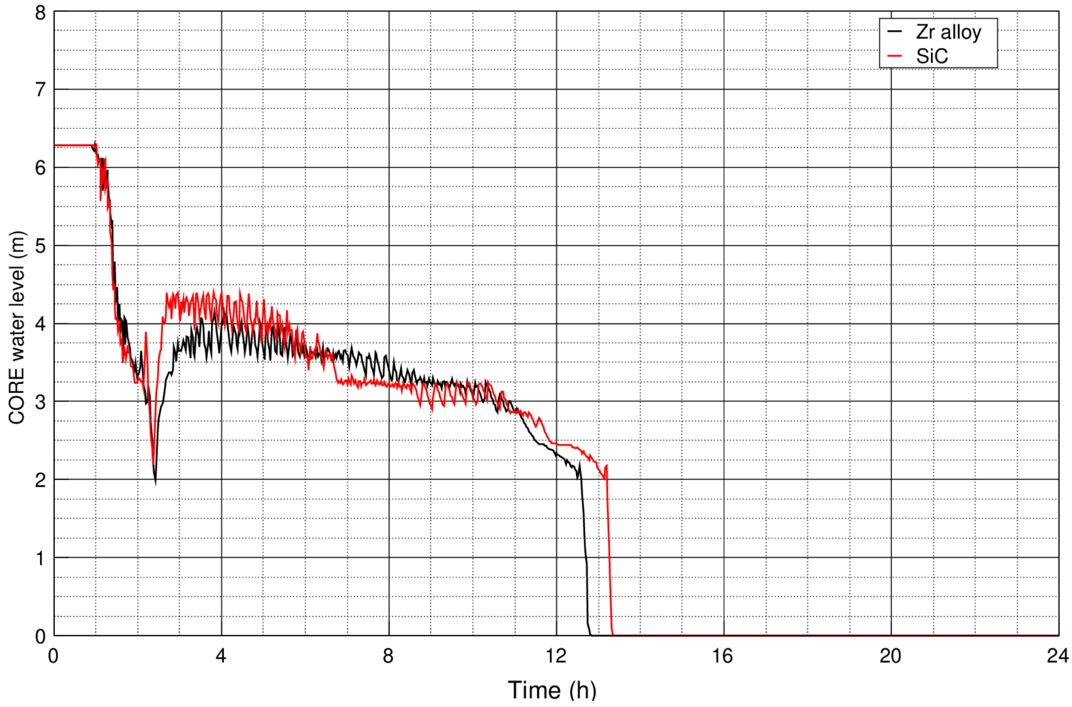

Fig. 7.7: CORE water level - SBO - total loss of power

The temperature of the coolant increases until it exceeds the setpoint for safety depressurisation of the RCS at about 2 hours after initiating event. When depressurisation is initiated, the pressure is relieved by fully opening the POSRV, but the water in the core evaporates. Due to the uncovery of the core, the cladding temperature quickly rises and oxidises, temperature rise is observable in fig. 7.8.

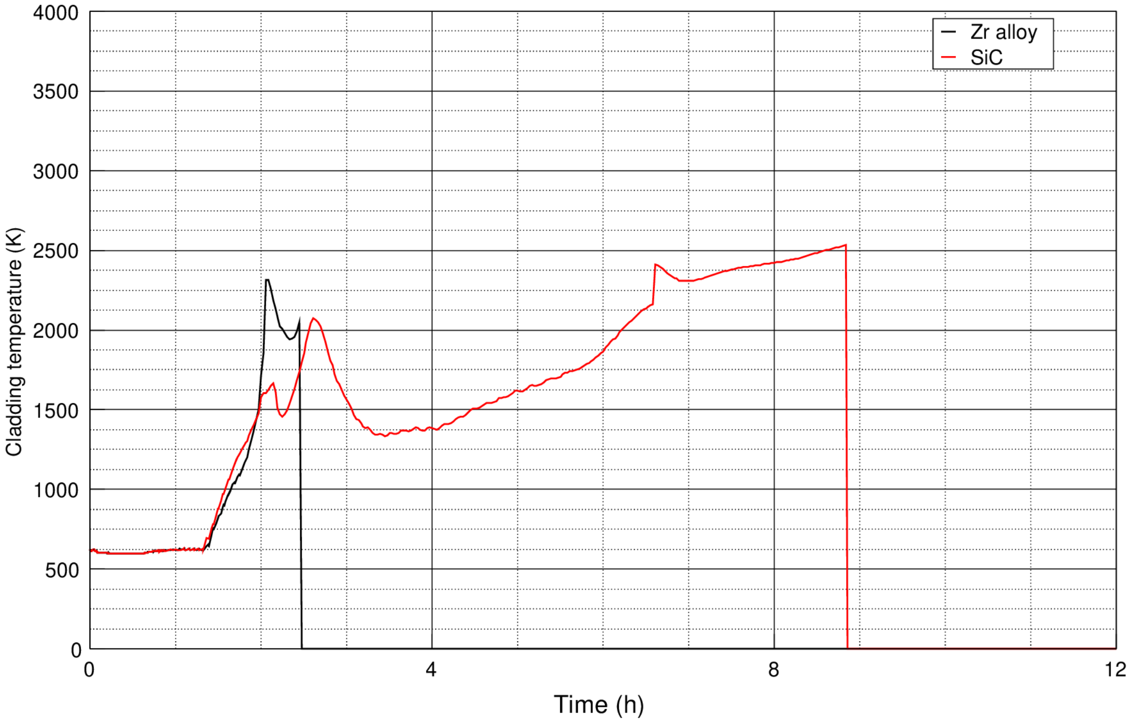

Fig. 7.8: Cladding temperature in cell 213 - SBO - total loss of power

A significant amount of heat in a short time is released, in fig. 7.9 apparent in the initial quick rise. Zircaloy cladding fails in cell 213 due to this heat release at about 2,5 hours. The SiC cladding oxidises slower, and because its melting point is higher, it does not melt at the time when the Zircaloy cladding has already failed. After depressurisation, the SIT check valves have opened and injected borated water into the core, cooling it down. Fuel rods with Zircaloy cladding that had been melted are more difficult to cool because of the limited surface area for heat transfer. Due to the decay heat from the fuel, the injected water evaporates and the core water level decreases again over time.

Zircaloy cladding is severely oxidised; oxidation is only slowly progressing on other structures. SiC further oxidises, releasing heat and hydrogen. At a time about 12 hours for Zircaloy and 13 hours for SiC, the water in the lower plenum evaporates by dropped corium, and the released vapour further oxidises the structures. The total cumulative amount of oxidation heat and hydrogen produced is lower in the case of SiC because of its slower oxidation kinetics.

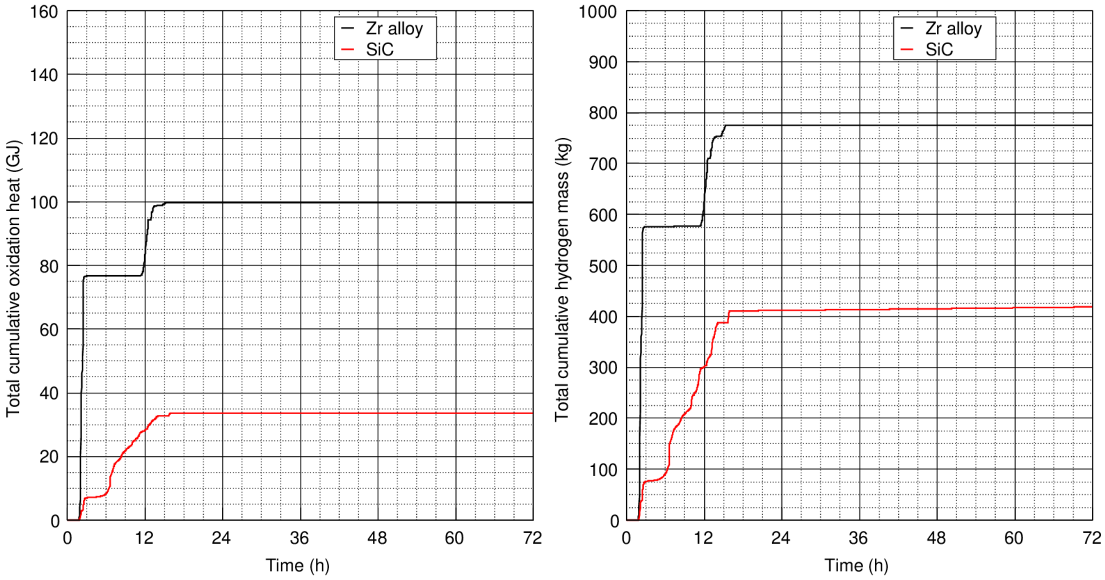

Fig. 7.9: Total cumulative heat and hydrogen produced due to in-vessel oxidation of components - SBO - total loss of power

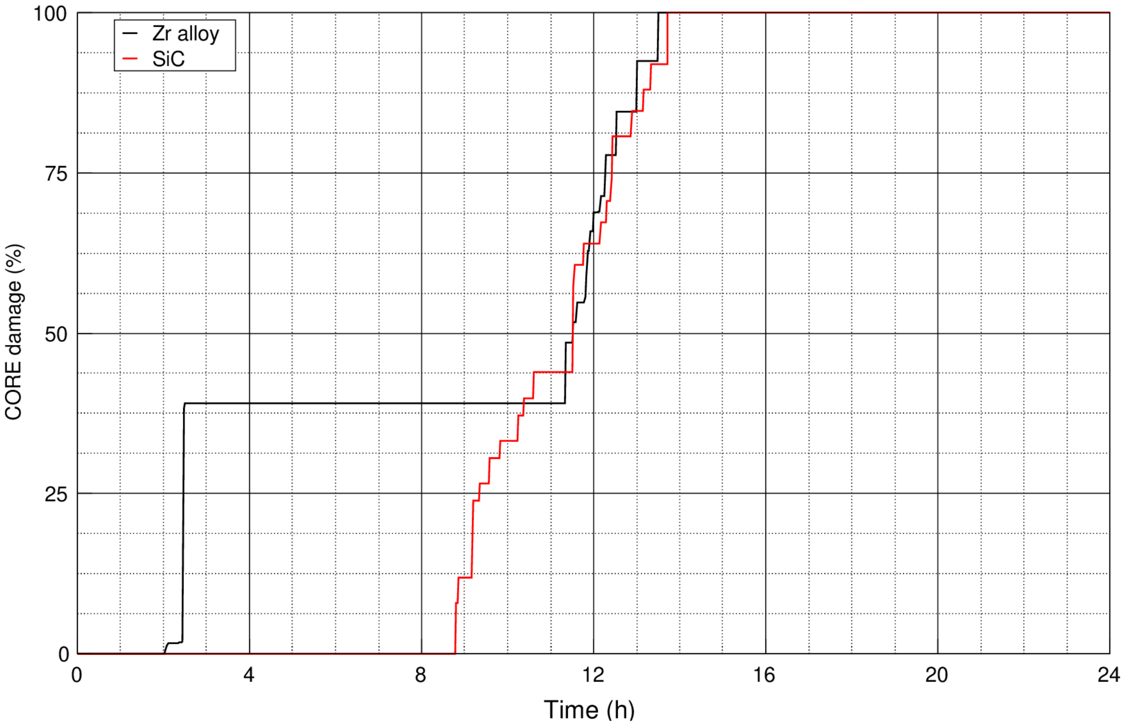

Fig. 7.10: CORE damage - SBO - total loss of power

In fig. 7.10 the percentual core damage is shown. After Zircaloy melting at 2,5 hours, 40 % of the core was damaged. At a time close to 9 hours, the SiC cladding fails by damage function, the fuel pellets have melted due to oxidation and decay heat. In addition, the Zircaloy cladding starts to melt again at over 9 hours to the simulation. At a time about 12 hours for Zircaloy and 13 hours for SiC, the molten corium melts the support plate and relocates to the lower plenum. At about 13,5 hours, the core damage of 100 % is achieved and all of the molten corium has already relocated to the lower plenum. The results of SBO - total loss of power with Zircaloy and SiC are listed in tab. 7.3.1. The total cumulative heat and hydrogen produced as a result of in-vessel oxidation of the components have been reduced by the use of SiC. The time to first cladding failure increased by more than 6 hours, and the RPV failure occurred almost an hour later when SiC was used; SiC maintained its structural integrity during the depressurisation period as a lower amount of oxidation heat was released.

Tab. 7.4: Results of SBO - total loss of power

	Zr alloy	SiC
Total cumulative oxidation heat (GJ)	99,754	33,554
Total cumulative hydrogen mass (kg)	775,128	418,436
Carbon monoxide (kg)	90,562	117,431
Carbon dioxide (kg)	67,731	90,093
Hydrogen by cladding oxidation (kg)	578,179	13,478
Time to first cladding failure (s)	∼8843	∼31618
Time to RPV failure (s)	∼53181	∼56535

7.3.2 Station blackout - loss of AC power

The station blackout with loss of AC power assumes the availability of DC power from batteries for operation of critical systems and some engineered safety features, especially the auxiliary feedwater system. The auxiliary feedwater system supplies the steam generators with feedwater, allowing heat removal from the RCS by feed-and-bleed operation. DC power is available for 8 hours from the initiating event to the scenario. After 10 hours, the steam generators began to dry out and the loss of ultimate heat sink occurs. With the heat sink lost, the pressure and temperature in the RCS increases due to the decay heat from the fuel. The pressure is relieved by the operation of the POSRV. But because there is no making up on the core water level, it decreases, slowly uncovering the core. The decrease in water level due to depressurisation is observable in fig. 7.11, from a time of 10 hours and further.

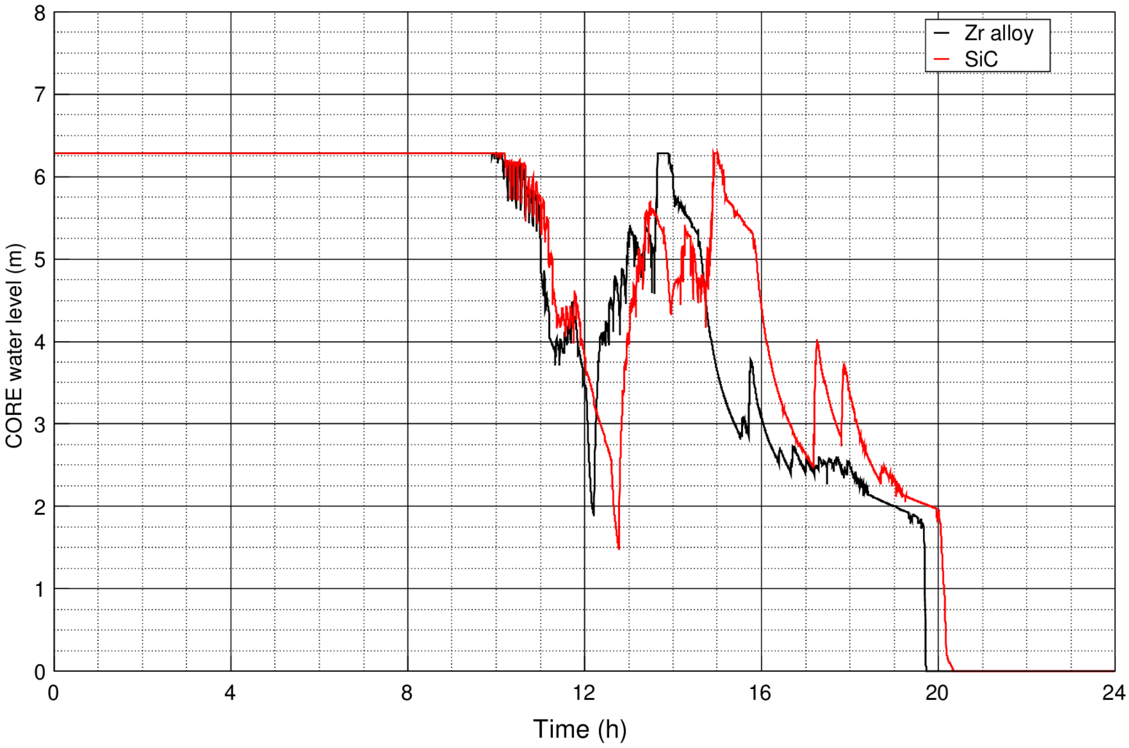

Fig. 7.11: CORE water level - SBO - loss of AC power

The temperature of the coolant increases until it exceeds the setpoint for safety depressurisation of the RCS at about 12 hours after initiating event. When depressurisation is initiated, the pressure is relieved by fully opening the POSRV. Due to pressure relief and as the water remaining in the core still has a high temperature, it evaporates. Due to the uncovery of the core, the cladding oxidises and temperature rapidly rises, temperature rise is observable in fig. 7.12.

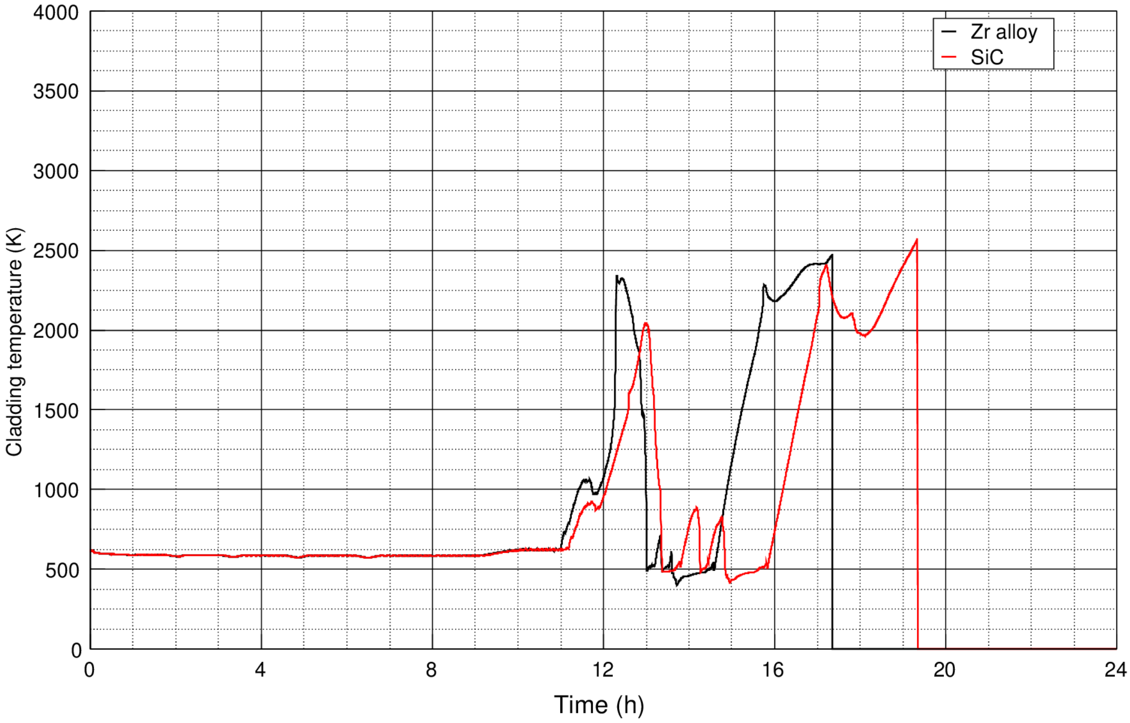

Fig. 7.12: Cladding temperature in cell 213 - SBO - loss of AC power

Heat released due to the oxidation in a short time, after the water evaporated due pressure relief, is apparent in fig. 7.13 at the initial rise. Zircaloy cladding temperature in cell 213 rises to over 2300 K and the cladding begins to candle. The SiC cladding temperature rises to 2000 K while the oxidation is slower. Because of the higher melting point and thermal conductivity, SiC does not start to candle like Zircaloy. Following RCS depressurisation, the SIT check valves have opened and borated water was injected into the core, cooling it down. The decay heat from the fuel, the injected water from SIT absorbs the heat and evaporates, causing the slow decrease in the core water level over time.

At about 15 hours in simulation, the Zircaloy cladding continues to oxidise as the surface temperature exceeded 1100 K; oxidation is also progressing on other structures. The SiC continues to oxidise at 16,5 hours as the surface temperature exceeds 1373,15 K, in both cases releasing heat and hydrogen. At a time about 19,5 hours for Zircaloy and 20 hours for SiC, corium melts through the support plate, the water in lower plenum is immediately evaporated, and the released vapour further oxidises the structures. The total cumulative amount of oxidation heat and hydrogen produced is lower in the case of SiC; the difference between the cases is caused by slower oxidation kinetics of SiC.

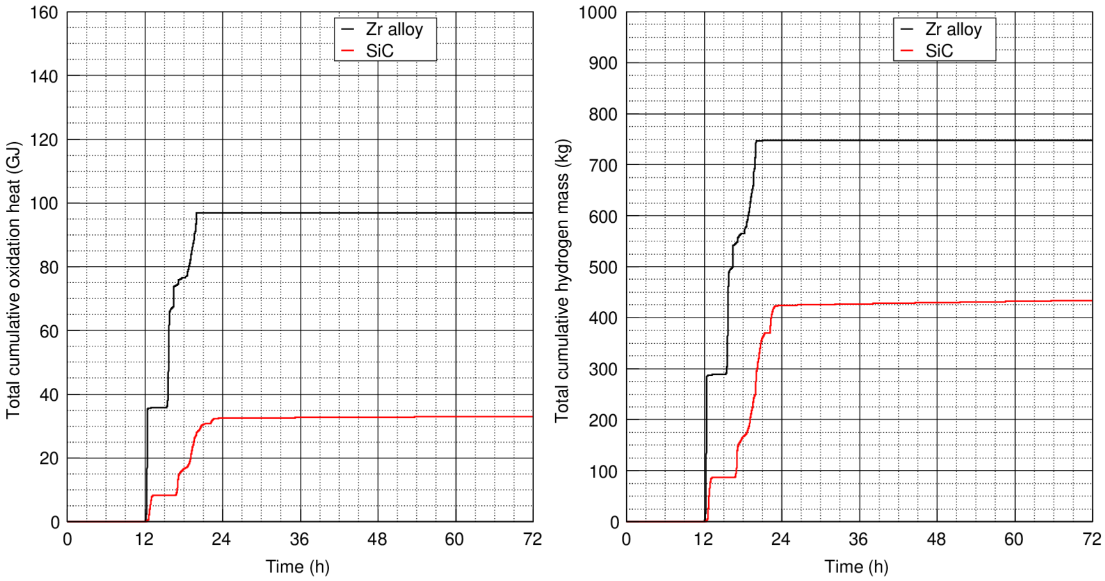

Fig. 7.13: Total cumulative heat and hydrogen produced due to in-vessel oxidation of components - SBO - loss of AC power

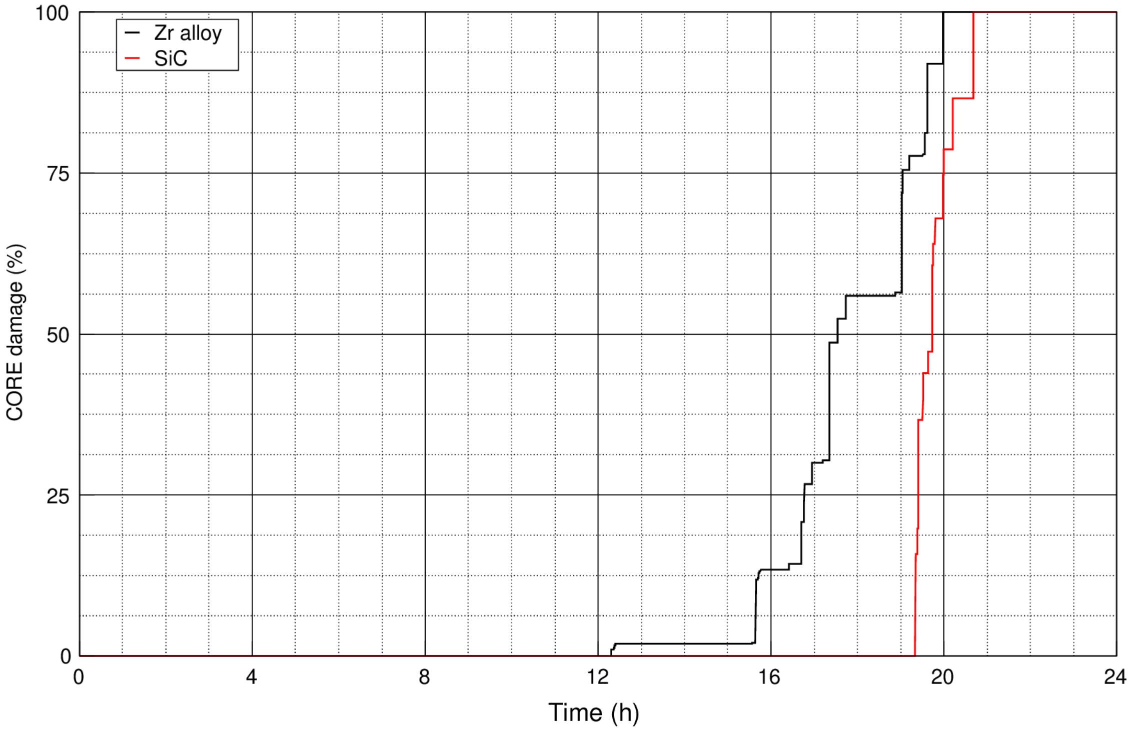

Fig. 7.14: CORE damage - SBO - loss of AC power

In fig. 7.14 the percentual core damage is shown. The core was partially slightly damaged by the candling of Zircaloy at a time of around 12 hours. The Zircaloy begins to melt at a time of 15,5 hours due to prolonged core uncovering and decay heat from the fuel. The first failure of the SiC cladding resulting from the damage function occurred about 19,3 hours due to the released oxidation heat and the decay heat from the fuel. As the fuel is melted before the cladding, and significant amount of heat accumulated in the cladding, the meltdown of the core progresses rapidly, and all cells with active fuel are melted within an hour following the first failure. The total damage to the core in case of Zircaloy occurs approximately at 20 hours, and in case of SiC, the total core damage occurs at 20,6 hours.

The results of SBO - loss of AC power with Zircaloy and SiC are listed in tab. 7.3.2. The total cumulative heat and hydrogen produced as a result of in-vessel oxidation of the components have been significantly reduced by the use of SiC. The first cladding and RPV failures occured over an hour occurred later when SiC was used, SiC maintained its structural integrity for a longer period because of its high melting point and lower amount of oxidation heat released.

Tab. 7.5: Results of SBO - loss of AC power

	Zr alloy	SiC
Total cumulative oxidation heat (GJ)	99,269	32,980
Total cumulative hydrogen mass (kg)	788,702	434,2
Carbon monoxide (kg)	114,548	101,8
Carbon dioxide (kg)	30,716	101
Hydrogen by cladding oxidation (kg)	573,882	15,096
Time to first cladding failure (s)	∼64257	∼69635
Time to RPV failure (s)	∼75319	∼79969

Conclusion

Accident tolerant fuels have a significant potential to improve nuclear plant safety due to their excellent resistance against the conditions that occur in a plant that undergoes an accident. The three ways to make these fuels are by using new cladding materials, by introducing coatings for today's zirconium alloy claddings or by use of new fuel matrix compounds. The research of advanced cladding materials made significant steps after the Fukushima accident; some behaviours of these advanced materials remain unknown, especially the properties of the materials after long-term irradation and oxidation kinetics in high-temperature steam and air environments; some such as FeCrAl alloys have been a point of interest for well-known institutions. The time of deployment could still not be estimated as there are still many questions to answer and the design has to be verified.

In this thesis two advanced cladding materials were recognised for simulations of severe accident scenarios in MELCOR. Although the properties of the materials were not exact for those implemented, estimated properties may give an approximation on how the materials would behave and perform. Three accident sequences were analysed, unmitigated LB LOCA, which was used for the basic configuration of the materials, SBO with total loss of power and SBO with loss of AC power, all set to eventually achieve 100 % core damage and lower head penetration.

In all scenarios, the advanced cladding materials exhibit significantly lower hydrogen and heat production by cladding oxidation due to their slower oxidation kinetics. In the LOCA scenario, the time to first cladding failures and lower head penetration slightly increased. The cladding failure of FeCrAl occurs sooner than that of Zircaloy as a result of its lower melting point. The LOCA scenario was also used to determine the sensitivity of oxide formation and its impact on the time of first cladding failure, hydrogen and heat production. The trend of increasing proportion of aluminium oxide in the generic oxide formed in MELCOR shows that a higher amount of heat is released by oxidation because the standard enthalpy of the formation of aluminium oxide is the highest above the ones considered. In addition, the amount of hydrogen released also increased. The times of first cladding failure and lower head penetration vary among the compositions. The more iron oxide in the oxide scale, the sooner the cladding fails, as a result of the lower thermal conductivity of the oxide, while the time to lower head penetration was extended as the fuel pellets were not melted. However, the oxidation model in MELCOR considers the formation of the so-called generic FeCrAl oxide and does not treat the oxides separately; such an approach may differ from real-world oxidation, where oxide layers are formed.

In SBO with total loss of power, the time period to first cladding failure has been significantly extended from 2,5 hours of Zircaloy to almost 9 hours when SiC was used. The SiC exhibits its higher melting point and enhanced thermal conductivity over Zircaloy. Under conditions of SBO with available DC power, the time to core damage was extended by use of SiC over Zircaloy, from approximately 12 hours to over 19,3 hours.

In general, both implemented materials could improve safety margins of the plant as they exhibit slower oxidation kinetics, resulting in lower amounts of heat and hydrogen released. The lower melting point of FeCrAl results in sooner cladding breakdown, although the oxides formed on the surface could have a great impact on extending the period before the failure occurs; the oxide formation on the FeCrAl is one of its protection mechanisms. Further research on oxide formation is desirable to fully understand the mechanism of protection and its impact on material degradation and performance under severe accident conditions. In general, silicon carbide under severe accident conditions demonstrates its high melting point and high thermal conductivity. However, the cladding design, that was assumed monolithic in this thesis, would have a huge impact on the cladding performance. The design of such cladding would have to be greatly considered to exhibit exclusive thermal properties of silicon carbide, while addressing the issues such as hydrothermal corrosion or brittleness to mechanical stresses.

Bibliography

1. JEON, S. Y. et al. An Investigation on the Fuel Assembly Structural Performance for the PLUS7 Fuel Design. In: 2009. Available also from: `https://api.semanticscholar.org/CorpusID:55739379`.
2. ZHOU, Z.; MA, Z.; JIANG, Y.; PENG, M. Fault Diagnosis Using Bond Graphs in an Expert System. *Energies*. 2022, vol. 15, no. 15, p. 5703. ISSN 1996-1073. Available from DOI: `10.3390/en15155703`.
3. SARKISOV, E. S.; CHEBOTAREV, N. T.; NEVZOROVA, A. A.; ZVERKOV, A. I. Oxidation of zirconium at high temperature and structure of the primary oxide film. *The Soviet Journal of Atomic Energy*. 1958, vol. 5, no. 5, pp. 1465–1470. Available from DOI: `10.1007/bf01498490`.
4. In: *Closed Nuclear Fuel Cycle with Fast Reactors*. Elsevier, 2022, pp. 161–167. Available from DOI: `10.1016/b978-0-323-99308-1.00034-9`.
5. KNIEF, R. A. Nuclear Fuel Cycles. In: *Encyclopedia of Physical Science and Technology*. Elsevier, 2003, pp. 655–670. Available from DOI: `10.1016/b0-12-227410-5/00490-7`.
6. FINK, J. K. Thermophysical properties of uranium dioxide. *Journal of Nuclear Materials*. 2000, vol. 279, no. 1, pp. 1–18. ISSN 0022-3115. Available from DOI: `10.1016/s0022-3115(99)00273-1`.
7. KAVAZAURI, R.; POKROVSKIY, S. A.; BARANOV, V. G.; TENISHEV, A. V. Thermal properties of nonstoichiometry uranium dioxide. *IOP Conference Series: Materials Science and Engineering*. 2016, vol. 130, p. 012025. ISSN 1757-899X. Available from DOI: `10.1088/1757-899x/130/1/012025`.
8. POPOV, S. G.; CARBAJO, J. J.; IVANOV, V. K.; YODER, G. L. *Thermophysical Properties of MOX and UO2 Fuels Including the Effects of Irradiation*. 2000. Tech. rep. Kurchatov Institute, Oak Ridge National Laboratory. Available also from: `https://info.ornl.gov/sites/publications/Files/Pub57523.pdf`.
9. PROPERTIES, Material. Uranium Dioxide – Density – Melting Point – Thermal Conductivity. 2024. Available also from: `https://material-properties.org/uranium-dioxide-density-melting-point-thermal-conductivity`.
10. STEINBRÜCK, M.; BÖTTCHER, M. Air oxidation of Zircaloy-4, M5® and ZIRLO™ cladding alloys at high temperatures. *Journal of Nuclear Materials*. 2011, vol. 414, no. 2, pp. 276–285. ISSN 0022-3115. Available from DOI: `10.1016/j.jnucmat.2011.04.012`.

11. COX, B. Some thoughts on the mechanisms of in-reactor corrosion of zirconium alloys. *Journal of Nuclear Materials*. 2005, vol. 336, no. 2–3, pp. 331–368. ISSN 0022-3115. Available from DOI: `10.1016/j.jnucmat.2004.09.029`.
12. COX, B. The Oxidation and Corrosion of Zirconium and its Alloys. *Journal of The Electrochemical Society*. 1961, vol. 108, no. 1, p. 24. ISSN 0013-4651. Available from DOI: `10.1149/1.2428005`.
13. WANKLYN, J. N.; BRITTON, C. F.; SILVESTER, D. R.; WILKINS, N. J. M. Influence of Environment on the Corrosion of Zirconium and Its Alloys in High-Temperature Steam. *Journal of The Electrochemical Society*. 1963, vol. 110, no. 8, p. 856. ISSN 0013-4651. Available from DOI: `10.1149/1.2425891`.
14. CENTRE., European Commission. Joint Research. *Development of M5 cladding material correlations in the TRANSURANUS code: revision 1.* Publications Office, 2016. Available from DOI: `10.2789/320793`.
15. LUSCHER, W.G.; GEELHOOD, K.J. *Material Property Correlations: Comparisons between FRAPCON-3.4, FRAPTRAN 1.4, and MATPRO.* Pacific Northwest National Laboratory, 2011. Available also from: `https://www.nrc.gov/docs/ML1110/ML11101A012.pdf`.
16. MITCHELL, D.B.; DUNN, B. M. *Evaluation of Advanced Cladding and Structural Material (M5) in PWR Reactor Fuel.* Framatome Cogema Fuels, 2000. Available also from: `https://www.nrc.gov/docs/ML0036/ML003686365.pdf`.
17. STEINBRÜCK, M.; VÉR, N.; GROSSE, M. Oxidation of Advanced Zirconium Cladding Alloys in Steam at Temperatures in the Range of 600–1200 °C. *Oxidation of Metals*. 2011, vol. 76, no. 3–4, pp. 215–232. ISSN 1573-4889. Available from DOI: `10.1007/s11085-011-9249-3`.
18. VAN BRUTZEL, L.; DINGREVILLE, R.; BARTEL, T.J. *Nuclear fuel deformation phenomena.* 1CEA, DEN, DPC, Centre de Saclay, France; Sandia National Laboratories, US, [n.d.]. Available also from: `https://inis.iaea.org/collection/NCLCollectionStore/_Public/47/032/47032408.pdf`.
19. YAGNIK, S.; GARDE, A. Zirconium Alloys for LWR Fuel Cladding and Core Internals. In: *Structural Alloys for Nuclear Energy Applications*. Elsevier, 2019, pp. 247–291. Available from DOI: `10.1016/b978-0-12-397046-6.00007-1`.
20. BENEDICT, A. *Operator Generic Fundamentals Thermodynamics – Thermal Hydraulics* [Web]. 2017. Available also from: `https://slideplayer.com/slide/13568222/`.

21. JERNKVIST, L.; MASSIH, A. *Models for axial relocation of fragmented and pulverized fuel pellets in distending fuel rods and its effects on fuel rod heat load*. 2015-09. Tech. rep. Available also from: `https://www.researchgate.net/publication/281826522_Models_for_axial_relocation_of_fragmented_and_pulverized_fuel_pellets_in_distending_fuel_rods_and_its_effects_on_fuel_rod_heat_load`.

22. NIHAN ONDER, E. Nuclear fuel. In: *Pressurized Heavy Water Reactors*. Elsevier, 2022, pp. 45–68. ISBN 9780128220542. Available from DOI: `10.1016/b978-0-12-822054-2.00008-8`.

23. KARDOULAKI, E.; FRAZER, D.M.; WHITE, J.T.; CARVAJAL, U.; NELSON, A.T.; BYLER, D.D.; SALEH, T.A.; GONG, B.; YAO, T.; LIAN, J.; MCCLELLAN, K.J. Fabrication and thermophysical properties of UO2-UB2 and UO2-UB4 composites sintered via spark plasma sintering. *Journal of Nuclear Materials*. 2021, vol. 544, p. 152690. Available from DOI: `10.1016/j.jnucmat.2020.152690`.

24. TURNER, J.; MARTINI, F.; BUCKLEY, J.; PHILLIPS, G.; MIDDLEBURGH, S.C.; ABRAM, T.J. Synthesis of candidate advanced technology fuel: Uranium diboride (UB2) via carbo/borothermic reduction of UO2. *Journal of Nuclear Materials*. 2020, vol. 540, p. 152388. Available from DOI: `10.1016/j.jnucmat.2020.152388`.

25. YUSHIN, D. I.; SMIRNOV, A. V.; SOLIS PINARGOTE, N. W.; PERETYAGIN, P. Y.; TORRECILLAS SAN MILLAN, R. Modeling Process of Spark Plasma Sintering of Powder Materials by Finite Element Method. *Materials Science Forum*. 2015, vol. 834, pp. 41–50. Available from DOI: `10.4028/www.scientific.net/msf.834.41`.

26. YANG, Y. F.; QIAN, M. Spark plasma sintering and hot pressing of titanium and titanium alloys. In: *Titanium Powder Metallurgy*. Elsevier, 2015, pp. 219–235. Available from DOI: `10.1016/b978-0-12-800054-0.00013-7`.

27. THE MATERIALS PROJECT. *Materials Data on UB4 by Materials Project*. LBNL Materials Project; Lawrence Berkeley National Laboratory (LBNL), Berkeley, CA (United States), 2020. Available from DOI: `10.17188/1277960`.

28. LUPINETTI, A. J.; FIFE, J. L.; GARCIA, E.; DORHOUT, P. K.; ABNEY, K. D. Low-Temperature Synthesis of Uranium Tetraboride by Solid-State Metathesis Reactions. *Inorganic Chemistry*. 2002, vol. 41, no. 9, pp. 2316–2318. Available from DOI: `10.1021/ic015607a`.

29. GUO, H.; WANG, J.; CHEN, D.; TIAN, W.; CAO, S.; CHEN, D.; TAN, C.; DENG, Q.; QIN, Z. Boro/carbothermal reduction synthesis of uranium tetraboride and its oxidation behavior in dry air. *Journal of the American Ceramic Society*. 2018, vol. 102, no. 3, pp. 1049–1056. Available from DOI: `10.1111/jace.15987`.

30. JONES, S.; BOXALL, C.; MAHER, C.; TAYLOR, R. A review of the reprocessability of uranium nitride based fuels. *Progress in Nuclear Energy*. 2023, vol. 165, p. 104917. Available from DOI: `10.1016/j.pnucene.2023.104917`.

31. MOUSTAFA, A. A study on the feasibility of using Uranium Nitride (UN) fuel in Pressurized water reactors (PWR). *Alexandria Engineering Journal*. 2023, vol. 69, pp. 1–8. Available from DOI: `10.1016/j.aej.2023.01.044`.

32. DAVID, M. K.; STEPHEN, T. L. Progress in molecular uranium-nitride chemistry. *Coordination Chemistry Reviews*. 2014, vol. 266-267, pp. 2–15. Available from DOI: `10.1016/j.ccr.2013.06.013`.

33. WAGNER, A. R.; HARP, J. M.; ARCHIBALD, K. E.; ASHBY, S. C.; WATKINS, J. K.; TOLMAN, K. R. Fabrication of stoichiometric U3Si2 fuel pellets. *MethodsX*. 2019, vol. 6, pp. 1252–1260. Available from DOI: `10.1016/j.mex.2019.05.016`.

34. NELSON, A. T.; MIGDISOV, A.; SOOBY WOOD, E.; GROTE, C. J. U3Si2 behavior in H2O environments: Part II, pressurized water with controlled redox chemistry. *Journal of Nuclear Materials*. 2018, vol. 500, pp. 81–91. Available from DOI: `10.1016/j.jnucmat.2017.12.026`.

35. FIELD, K. G.; YAMAMOTO, Y.; PINT, B. A.; GUSSEV, M. N.; TERRANI, K. A. Accident Tolerant FeCrAl Fuel Cladding: Current Status Towards Commercialization. In: *The Minerals, Metals & Materials Series*. Springer International Publishing, 2017, pp. 1381–1389. Available from DOI: `10.1007/978-3-030-04639-2_91`.

36. STOTT, F. H.; WOOD, G. C.; STRINGER, J. The influence of alloying elements on the development and maintenance of protective scales. *Oxidation of Metals*. 1995, vol. 44, no. 1-2, pp. 113–145. Available from DOI: `10.1007/bf01046725`.

37. QU, H. P.; LANG, Y. P.; YAO, C. F.; CHEN, H. T.; YANG, C. Q. The effect of heat treatment on recrystallized microstructure, precipitation and ductility of hot-rolled Fe–Cr–Al–REM ferritic stainless steel sheets. *Materials Science and Engineering: A*. 2013, vol. 562, pp. 9–16. Available from DOI: `10.1016/j.msea.2012.11.008`.

38. CHERUBINI, M.; PASTORE, G.; PENTTILÄ, S.; SEVECEK, M.; STUCKERT, J.; VESHCHUNOV, M.; ZOZULIA, I. *Analysis of Options and Experimental Examination of Fuels for Water Cooled Reactors with Increased Accident Tolerance (ACTOF) IAEA-TECDOC-1921*. 2020-07. Tech. rep.
39. FIELD, K. G. *Handbook on the Material Properties of FeCrAl Alloys for Nuclear Power Production Applications*. 2018. Tech. rep. Oak Ridge National Laboratory.
40. QIU, B.; WANG, J.; DENG, Y.; WANG, M.; WU, Y.; QIU, S. Z. A review on thermohydraulic and mechanical-physical properties of SiC, FeCrAl and Ti3SiC2 for ATF cladding. *Nuclear Engineering and Technology*. 2020, vol. 52, no. 1, pp. 1–13. Available from DOI: `10.1016/j.net.2019.07.030`.
41. KOYANAGI, T.; KATOH, Y.; SINGH, G.; SNEAD, M. SiC/SiC cladding materials properties handbook. *ORNL*. 2017. Available also from: `https://info.ornl.gov/sites/publications/Files/Pub100714.pdf`.
42. LORRETTE, C.; SAUDER, C.; BILLAUD, P.; HOSSEPIED, C.; LOUPIAS, G.; BRAUN, J.; MICHAUX, A.; TORRES, E.; REBILLAT, F.; BISCHOFF, J.; AMBARD, A. SiC/SiC composite behavior in LWR conditions and under high temperature steam environment. *Top Fuel 2015*. 2015. Available also from: `https://cea.hal.science/cea-02492574/`.
43. KIM, W.-J.; HWANG, H. S.; PARK, J. Y. *Journal of Materials Science Letters*. 2002, vol. 21, no. 9, pp. 733–735. Available from DOI: `10.1023/a:1015797324658`.
44. CARPENTER, D. M. *An assessment of silicon carbide as a cladding material for light water reactors*. 2011. Available also from: `https://dspace.mit.edu/handle/1721.1/76975`. PhD thesis. Massachusetts Institute of Technology. Dept. of Nuclear Science and Engineering.
45. TERRANI, K. A.; PINT, B. A.; PARISH, C. M.; SILVA, C. M.; SNEAD, L. L.; KATOH, Y. Silicon Carbide Oxidation in Steam up to 2 MPa. *Journal of the American Ceramic Society*. 2014, vol. 97, no. 8, pp. 2331–2352. Available from DOI: `10.1111/jace.13094`.
46. LIPPMANN, W.; KNORR, J.; NÖRING, R.; UMBREIT, M. Investigation of the use of ceramic materials in innovative light water reactor – fuel rod concepts. *Nuclear Engineering and Design*. 2001, vol. 205, no. 1-2, pp. 13–22. Available from DOI: `10.1016/s0029-5493(00)00369-1`.

47. MARUYAMA, Tadashi; HARAYAMA, Masaaki. Relationship between dimensional changes and the thermal conductivity of neutron-irradiated SiC. *Journal of Nuclear Materials*. 2004, vol. 329-333, pp. 1022–1028. Available from DOI: `10.1016/j.jnucmat.2004.04.128`.

48. SNEAD, L.L. Limits on irradiation-induced thermal conductivity and electrical resistivity in silicon carbide materials. *Journal of Nuclear Materials*. 2004, vol. 329-333, pp. 524–529. Available from DOI: `10.1016/j.jnucmat.2004.04.294`.

49. JONES, R. H.; STEINER, D.; HEINISCH, H. L.; NEWSOME, G. A.; KERCH, H. M. Radiation resistant ceramic matrix composites. *Journal of Nuclear Materials*. 1997, vol. 245, no. 2-3, pp. 87–107. Available from DOI: `10.1016/s0022-3115(97)00022-6`.

50. KATOH, Y.; SNEAD, L. L.; SZLUFARSKA, I.; WEBER, W. J. Radiation effects in SiC for nuclear structural applications. *Current Opinion in Solid State and Materials Science*. 2012, vol. 16, no. 3, pp. 143–152. Available from DOI: `10.1016/j.cossms.2012.03.005`.

51. BARSOUM, M. W.; YOO, H.-I.; POLUSHINA, I. K.; RUD', V. Yu.; RUD', Yu. V.; EL-RAGHY, T. Electrical conductivity, thermopower, and Hall effect of Ti3AlC2, Ti4AlN3, and Ti3SiC2. *Physical Review B*. 2000, vol. 62, no. 15, pp. 10194–10198. ISSN 1095-3795. Available from DOI: `10.1103/physrevb.62.10194`.

52. SNEAD, L. L.; NOZAWA, T.; KATOH, Y.; BYUN, T. -S.; KONDO, S.; PETTI, D. A. Handbook of SiC properties for fuel performance modeling. *Journal of Nuclear Materials*. 2007, vol. 371, no. 1–3, pp. 329–377. ISSN 0022-3115. Available from DOI: `10.1016/j.jnucmat.2007.05.016`.

53. FARLE, A.-S.; KWAKERNAAK, C.; ZWAAG, S. van der; SLOOF, W. G. A conceptual study into the potential of Mn+1AXn-phase ceramics for self-healing of crack damage. *Journal of the European Ceramic Society*. 2015, vol. 35, no. 1, pp. 37–45. ISSN 0955-2219. Available from DOI: `10.1016/j.jeurceramsoc.2014.08.046`.

54. ZHANG, H.; PRESSER, V.; BERTHOLD, C.; NICKEL, K. G.; WANG, X.; RAISCH, C.; CHASSÉ, T.; HE, L.; ZHOU, Y. Mechanisms and Kinetics of the Hydrothermal Oxidation of Bulk Titanium Silicon Carbide. *Journal of the American Ceramic Society*. 2010, vol. 93, no. 4, pp. 1148–1155. ISSN 1551-2916. Available from DOI: `10.1111/j.1551-2916.2009.03570.x`.

55. KASHKAROV, E.; AFORNU, B.; SIDELEV, D.; KRINITCYN, M.; GOUWS, V.; LIDER, A. Recent Advances in Protective Coatings for Accident Tolerant Zr-Based Fuel Claddings. *Coatings*. 2021, vol. 11, no. 5, p. 557. ISSN 2079-6412. Available from DOI: `10.3390/coatings11050557`.

56. ZHONG, W.; MOUCHE, P. A.; HAN, X.; HEUSER, B. J.; MANDAPAKA, K. K.; WAS, G. S. Performance of iron–chromium–aluminum alloy surface coatings on Zircaloy 2 under high-temperature steam and normal BWR operating conditions. *Journal of Nuclear Materials*. 2016, vol. 470, pp. 327–338. ISSN 0022-3115. Available from DOI: `10.1016/j.jnucmat.2015.11.037`.

57. KIM, H. -G.; KIM, I. -H.; JUNG, Y. -I.; PARK, D. -J.; PARK, J. -H.; YANG, J. -H.; KOO, Y. -H. Progress of surface modified Zr cladding development for ATF at KAERI. In: *Proceedings of the 2017 Water Reactor Fuel Performance Meeting, Ramada Plaza Jeju, Jeju Island, Korea*. 2017, pp. 10–14.

58. AYDOGAN, E.; WEAVER, J.S.; MALOY, S.A.; EL-ATWANI, O.; WANG, Y.Q.; MARA, N.A. Microstructure and mechanical properties of FeCrAl alloys under heavy ion irradiations. *Journal of Nuclear Materials*. 2018, vol. 503, pp. 250–262. ISSN 0022-3115. Available from DOI: `10.1016/j.jnucmat.2018.03.002`.

59. DABNEY, T.; JOHNSON, G.; YEOM, H.; MAIER, B.; WALTERS, J.; SRIDHARAN, K. Experimental evaluation of cold spray FeCrAl alloys coated zirconium-alloy for potential accident tolerant fuel cladding. *Nuclear Materials and Energy*. 2019, vol. 21, p. 100715. ISSN 2352-1791. Available from DOI: `10.1016/j.nme.2019.100715`.

60. GIGAX, J. G.; KENNAS, M.; KIM, H.; MAIER, B. R.; YEOM, H.; JOHNSON, G. O.; SRIDHARAN, K.; SHAO, L. Interface reactions and mechanical properties of FeCrAl-coated Zircaloy-4. *Journal of Nuclear Materials*. 2019, vol. 519, pp. 57–63. ISSN 0022-3115. Available from DOI: `10.1016/j.jnucmat.2019.03.004`.

61. XU, M.; LI, Q.; SONG, Y.; XU, Y.; SANSON, A.; SHI, N.; WANG, N.; SUN, Q.; WANG, C.; CHEN, X.; QIAO, Y.; LONG, F.; LIU, H.; ZHANG, Q.; VENIER, A.; REN, Y.; D'ACAPITO, F.; OLIVI, L.; DE SOUZA, D. O.; XING, X.; CHEN, J. Giant uniaxial negative thermal expansion in FeZr2 alloy over a wide temperature range. *Nature Communications*. 2023, vol. 14, no. 1. ISSN 2041-1723. Available from DOI: `10.1038/s41467-023-40074-7`.

62. PARK, D. J.; KIM, H. G.; JUNG, Y. I.; PARK, J. H.; YANG, J. H.; KOO, Y. H. Behavior of an improved Zr fuel cladding with oxidation resistant coating under loss-of-coolant accident conditions. *Journal of Nuclear Materials*.

2016, vol. 482, pp. 75–82. ISSN 0022-3115. Available from DOI: `10.1016/j.jnucmat.2016.10.021`.

63. BISCHOFF, J.; VAUGLIN, C.; DELAFOY, C.; BARBERIS, P.; PERCHE, D.; GUERIN, B.; VASSAULT, J.-P.; BRACHET, J.-C. Development of Cr-coated Zirconium Alloy Cladding for Enhanced Accident Tolerance. In: *Topfuel 2016 - Light Water Reactor (LWR) Fuel Performance Meeting*. Boise, United States, 2016. Available also from: `https://cea.hal.science/cea-02438699`.

64. WAGIH, M.; SPENCER, B.; HALES, J.; SHIRVAN, K. Fuel performance of chromium-coated zirconium alloy and silicon carbide accident tolerant fuel claddings. *Annals of Nuclear Energy*. 2018, vol. 120, pp. 304–318. ISSN 0306-4549. Available from DOI: `10.1016/j.anucene.2018.06.001`.

65. BRACHET, J. -C.; IDARRAGA-TRUJILLO, I.; FLEM, M. L.; SAUX, M. L.; VANDENBERGHE, V.; URVOY, S.; ROUESNE, E.; GUILBERT, T.; TOFFOLON-MASCLET, C.; TUPIN, M.; PHALIPPOU, C.; LOMELLO, F.; SCHUSTER, F.; BILLARD, A.; VELISA, G.; DUCROS, C.; SANCHETTE, F. Early studies on Cr-Coated Zircaloy-4 as enhanced accident tolerant nuclear fuel claddings for light water reactors. *Journal of Nuclear Materials*. 2019, vol. 517, pp. 268–285. ISSN 0022-3115. Available from DOI: `10.1016/j.jnucmat.2019.02.018`.

66. MA, H. -B.; YAN, J.; ZHAO, Y. -H.; LIU, T.; REN, Q. -S.; LIAO, Y. -H.; ZUO, J. -D.; LIU, G.; YAO, M. -Y. Oxidation behavior of Cr-coated zirconium alloy cladding in high-temperature steam above 1200 °C. *npj Materials Degradation*. 2021, vol. 5, no. 1. ISSN 2397-2106. Available from DOI: `10.1038/s41529-021-00155-8`.

67. JIANG, J.; ZHAN, D.; LV, J.; MA, X.; HE, X.; WANG, D.; HU, Y.; ZHAI, H.; TU, J.; ZHANG, W.; WANG, B. Comparative study on the tensile cracking behavior of CrN and Cr coatings for accident-tolerant fuel claddings. *Surface and Coatings Technology*. 2021, vol. 409, p. 126812. ISSN 0257-8972. Available from DOI: `10.1016/j.surfcoat.2020.126812`.

68. WU, A.; RIBIS, J.; BRACHET, J.-C.; CLOUET, E.; LEPRÊTRE, F.; BORDAS, E.; ARNAL, B. HRTEM and chemical study of an ion-irradiated chromium/zircaloy-4 interface. *Journal of Nuclear Materials*. 2018, vol. 504, pp. 289–299. ISSN 0022-3115. Available from DOI: `10.1016/j.jnucmat.2018.01.029`.

69. KUPRIN, A.S.; BELOUS, V.A.; VOYEVODIN, V.N.; VASILENKO, R.L.; OVCHARENKO, V.D.; TOLSTOLUTSKAYA, G.D.; KOPANETS, I.E.; KOLODIY,

I.V. Irradiation resistance of vacuum arc chromium coatings for zirconium alloy fuel claddings. *Journal of Nuclear Materials*. 2018, vol. 510, pp. 163–167. ISSN 0022-3115. Available from DOI: `10.1016/j.jnucmat.2018.07.063`.

70. KIM, J. -M.; HA, T. -H.; KIM, I. -H.; KIM, H. -G. Microstructure and Oxidation Behavior of CrAl Laser-Coated Zircaloy-4 Alloy. *Metals*. 2017, vol. 7, no. 2, p. 59. ISSN 2075-4701. Available from DOI: `10.3390/met7020059`.
71. PARK, D. J.; JUNG, Y. I.; PARK, J. H.; LEE, Y. H.; CHOI, B. K.; KIM, H. G. Microstructural characterization of accident tolerant fuel cladding with Cr–Al alloy coating layer after oxidation at 1200 °C in a steam environment. *Nuclear Engineering and Technology*. 2020, vol. 52, no. 10, pp. 2299–2305. ISSN 1738-5733. Available from DOI: `10.1016/j.net.2020.04.005`.
72. SIDELEV, D. V.; KASHKAROV, E. B.; SYRTANOV, M. S.; KRIVOBOKOV, V. P. Nickel-chromium (Ni–Cr) coatings deposited by magnetron sputtering for accident tolerant nuclear fuel claddings. *Surface and Coatings Technology*. 2019, vol. 369, pp. 69–78. ISSN 0257-8972. Available from DOI: `10.1016/j.surfcoat.2019.04.057`.
73. KHATKHATAY, F.; JIAO, L.; JIAN, J.; ZHANG, W.; JIAO, Z.; GAN, J.; ZHANG, H.; ZHANG, X.; WANG, H. Superior corrosion resistance properties of TiN-based coatings on Zircaloy tubes in supercritical water. *Journal of Nuclear Materials*. 2014, vol. 451, no. 1–3, pp. 346–351. ISSN 0022-3115. Available from DOI: `10.1016/j.jnucmat.2014.04.010`.
74. ALAT, E.; MOTTA, A. T.; COMSTOCK, R. J.; PARTEZANA, J. M.; WOLFE, D. E. Ceramic coating for corrosion (c3) resistance of nuclear fuel cladding. *Surface and Coatings Technology*. 2015, vol. 281, pp. 133–143. ISSN 0257-8972. Available from DOI: `10.1016/j.surfcoat.2015.08.062`.
75. KASHKAROV, E.B.; NIKITENKOV, N.N.; SUTYGINA, A.N.; BEZMATERNYKH, A.O.; KUDIIAROV, V.N.; SYRTANOV, M.S.; PRYAMUSHKO, T.S. Hydrogenation behavior of Ti-implanted Zr-1Nb alloy with TiN films deposited using filtered vacuum arc and magnetron sputtering. *Applied Surface Science*. 2018, vol. 432, pp. 207–213. ISSN 0169-4332. Available from DOI: `10.1016/j.apsusc.2017.04.035`.
76. TUNES, M. A.; SILVA, F. C. da; CAMARA, O.; SCHÖN, C. G.; SAGÁS, J. C.; FONTANA, L. C.; DONNELLY, S. E.; GREAVES, G.; EDMONDSON, P. D. Energetic particle irradiation study of TiN coatings: are these films appropriate for accident tolerant fuels? *Journal of Nuclear Materials*. 2018, vol. 512, pp. 239–245. ISSN 0022-3115. Available from DOI: `10.1016/j.jnucmat.2018.10.013`.

77. XIAO, W.; CHEN, H.; LIU, X.; TANG, D.; DENG, H.; ZOU, S.; REN, Y.; ZHOU, X.; LEI, M. Thermal shock resistance of TiN-, Cr-, and TiN/Cr-coated zirconium alloy. *Journal of Nuclear Materials*. 2019, vol. 526, p. 151777. ISSN 0022-3115. Available from DOI: `10.1016/j.jnucmat.2019.151777`.

78. LEE, K.; KIM, D.; YOON, Y. S. SiC/Si thin film deposited on zircaloy to improved accident tolerant fuel cladding. *Thin Solid Films*. 2018, vol. 660, pp. 221–230. ISSN 0040-6090. Available from DOI: `10.1016/j.tsf.2018.06.006`.

79. KASHKAROV, E. B.; SYRTANOV, M. S.; MURASHKINA, T. L.; KUROCHKIN, A. V.; SHANENKOVA, Y.; OBROSOV, A. Hydrogen Sorption Kinetics of SiC-Coated Zr-1Nb Alloy. *Coatings*. 2019, vol. 9, no. 1, p. 31. ISSN 2079-6412. Available from DOI: `10.3390/coatings9010031`.

80. LI, W.; WANG, Z.; SHUAI, J.; XU, B.; WANG, A.; KE, P. A high oxidation resistance Ti2AlC coating on Zirlo substrates for loss-of-coolant accident conditions. *Ceramics International*. 2019, vol. 45, no. 11, pp. 13912–13922. ISSN 0272-8842. Available from DOI: `10.1016/j.ceramint.2019.04.089`.

81. MAIER, B. R.; GARCIA-DIAZ, B. L.; HAUCH, B.; OLSON, L. C.; SINDELAR, R. L.; SRIDHARAN, K. Cold spray deposition of Ti2AlC coatings for improved nuclear fuel cladding. *Journal of Nuclear Materials*. 2015, vol. 466, pp. 712–717. ISSN 0022-3115. Available from DOI: `10.1016/j.jnucmat.2015.06.028`.

82. TANG, C.; STEINBRUECK, M.; STUEBER, M.; GROSSE, M.; YU, X.; ULRICH, S.; SEIFERT, H. J. Deposition, characterization and high-temperature steam oxidation behavior of single-phase Ti2AlC-coated Zircaloy-4. *Corrosion Science*. 2018, vol. 135, pp. 87–98. ISSN 0010-938X. Available from DOI: `10.1016/j.corsci.2018.02.035`.

83. *APR1400 Status Report*. 2020. Tech. rep. IAEA. Available also from: `https://aris.iaea.org/PDF/APR1400_2020May.pdf`.

84. ORHAN, M. F.; KAHRAMAN, H.; BABU, B. S. Approaches for integrated hydrogen production based on nuclear and renewable energy sources: Energy and exergy assessments of nuclear and solar energy sources in the United Arab Emirates. *International Journal of Hydrogen Energy*. 2017, vol. 42, no. 4, pp. 2601–2616. ISSN 0360-3199. Available from DOI: `10.1016/j.ijhydene.2016.05.044`.

85. MA, W.; YUAN, Y.; SEHGAL, B. R. In-Vessel Melt Retention of Pressurized Water Reactors: Historical Review and Future Research Needs. *Engineering*. 2016, vol. 2, no. 1, pp. 103–111. ISSN 2095-8099. Available from DOI: `10.1016/j.eng.2016.01.019`.

86. *Glossary: Design-basis accident*. 2021. Tech. rep. United States Nuclear Regulatory Commision. Available also from: `https://www.nrc.gov/reading-rm/basic-ref/glossary/design-basis-accident.html`.

87. *10 CFR Part 50* [online]. United States Nuclear Regulatory Commission, 2024. [cit. 2024-05-18]. Available from: `https://www.ecfr.gov/current/title-10/part-50`.

88. *DIS-14-01: Design Extension Conditions for Nuclear Power Plants*. 2013. Tech. rep. Canadian Nuclear Safety Commision. Available also from: `https://www.cnsc-ccsn.gc.ca/eng/acts-and-regulations/consultation/comment/d-14-01/`.

89. *Realistic Large Break LOCA Methodology for Pressurized Water Reactors*. 2010. Tech. rep. AREVA NP Inc. Available also from: `https://www.nrc.gov/docs/ML1102/ML110200553.pdf`.

90. LEE, S.; HONG, T. H.; SEO, M.; LEE, Y.; KIM, H. Extended Station Blackout Coping Capabilities of APR1400. *Science and Technology of Nuclear Installations*. 2014, vol. 2014, pp. 1–10. ISSN 1687-6083. Available from DOI: `10.1155/2014/980418`.

91. *DIVERSE AND FLEXIBLE COPING STRATEGIES (FLEX) IMPLEMENTATION GUIDE*. 2012. Tech. rep. Nuclear Energy Institute. Available also from: `https://www.nrc.gov/docs/ML1222/ML12221A205.pdf`.

92. PETRANGELI, G. Safety Analysis. In: *Nuclear Safety*. Elsevier, 2020, pp. 121–136. Available from DOI: `10.1016/b978-0-12-818326-7.00011-1`.

93. HUMPHRIES, L.L. *MELCOR Computer Code Manuals, Vol. 2: Reference Manual: SAND2023-10994 O*. 2.2 r2023.0. Washington: U.S.NRC, 2023.

94. CERNY, T.; MICIAN, P.; KATOVSKY, K.; PTACEK, M. Impact of External Injection from FLEX Equipment during LOCA in APR1400. In: *2023 23rd International Scientific Conference on Electric Power Engineering (EPE)*. IEEE, 2023. Available from DOI: `10.1109/epe58302.2023.10149246`.

95. *Hi-Nicalon Type S datasheet* [online]. COI Ceramics, Inc. [cit. 2024-05-07]. Available from: `https://www.coiceramics.com/assets/docs/fiber/nicalon/Hi-NICALON-Type-S.pdf`.

96. HAYNES, W. M.; LIDE, D. R. (eds.). *CRC Handbook of Chemistry and Physics: A ready-reference book of chemical and physical data*. 92nd ed., 2011 - 2012. London: Taylor & Francis, 2011. ISBN 9781439855126. Includes bibliographical references and index.

97. *Reaction Bonded Silicon Carbide* [online]. AZO Materials. [cit. 2024-05-07]. Available from: `https://www.azom.com/properties.aspx?ArticleID=147`.

98. MERRILL, B. J.; BRAGG-SITTON, S. M.; HUMRICKHOUSE, P. W. Modification of MELCOR for severe accident analysis of candidate accident tolerant cladding materials. *Nuclear Engineering and Design*. 2017, vol. 315, pp. 170–178. ISSN 0029-5493. Available from DOI: `10.1016/j.nucengdes.2017.02.021`.

99. HOFMEISTER, A. M. HEAT TRANSPORT PROPERTIES OF CRISTOBALITE AND DISCUSSION OF "SNOWFLAKE" FORMATION. *The Canadian Mineralogist*. 2013, vol. 51, no. 5, pp. 705–714. ISSN 1499-1276. Available from DOI: `10.3749/canmin.51.5.705`.

100. *PubChem Compound Summary for CID 24261, Silicon Dioxide* [online]. National Center for Biotechnology Information, 2024. [cit. 2024-05-08]. Available from: `https://pubchem.ncbi.nlm.nih.gov/compound/Silicon-Dioxide`.

101. *KANTHAL® APMT datasheet* [online]. KANTHAL®, 2021. [cit. 2024-05-03]. Available from: `https://www.kanthal.com/en/products/material-datasheets/tube/kanthal-apmt/`.

102. *Metals - Latent Heat of Melting* [online]. The Engineering ToolBox. [cit. 2024-05-10]. Available from: `https://www.engineeringtoolbox.com/fusion-heat-metals-d_1266.html`.

103. BADINI, C.; LAURELLA, F. Oxidation of FeCrAl alloy: influence of temperature and atmosphere on scale growth rate and mechanism. *Surface and Coatings Technology*. 2001, vol. 135, no. 2–3, pp. 291–298. ISSN 0257-8972. Available from DOI: `10.1016/s0257-8972(00)00989-0`.

104. LI, M.; AKOSHIMA, M.; ENDO, R.; UEDA, M.; TANEI, H.; SUSA, M. Thermal Diffusivity and Conductivity of Fe3O4 Scale Provided by Oxidation of Iron. *ISIJ International*. 2022, vol. 62, no. 1, pp. 275–277. ISSN 1347-5460. Available from DOI: `10.2355/isijinternational.isijint-2021-326`.

105. *Iron (II, III) Oxide, Fe3O4* [online]. MatWeb, 2024. [cit. 2024-05-13]. Available from: `https://www.matweb.com/search/datasheet.aspx?matguid=d9822b7b17204f34b8dd34803ae728b1`.

106. *Chromium (III) Oxide, Cr2O3* [online]. MatWeb, 2024. [cit. 2024-05-13]. Available from: `https://www.matweb.com/search/DataSheet.aspx?MatGUID=3a9a44124b9f46c584d916e7fcab60dc`.

107. BODIŠOVÁ, K.; PACH, L.; KOVÁR, V.; ČERŇANSKÝ, A. Alumina ceramics prepared by pressure filtration of alumina powder dispersed in boehmite sol. *Ceramics - Silikaty*. 2006, vol. 50, pp. 239–244. Available also from: `https://www.ceramics-silikaty.cz/2006/pdf/2006_04_239.pdf`.

108. *Corundum, Aluminum Oxide, Alumina, 99.9%, Al2O3* [online]. MatWeb, 2024. [cit. 2024-05-13]. Available from: `https://www.matweb.com/search/datasheet.aspx?matguid=c8c56ad547ae4cfabad15977bfb537f1&n=1`.

109. PASTORE, G.; GAMBLE, K. A.; HALES, J. D. *Modeling Benchmark for FeCrAl Cladding in the IAEA CRP ACTOF: FeCrAl-C35M Material Models and Benchmark Cases Specifications*. 2017. Available from DOI: `10.2172/1468589`.

110. SHACKELFORD, J. F.; ALEXANDER, W. *MATERIALS SCIENCE AND ENGINEERING HANDBOOK*. CRC Press LLC, 2001.

111. FRANO, R. L.; AQUARO, D.; SCALETTI, L.; OLIVI, N. Characterization of the thermal conductivity for ceramic pebble beds. *Journal of Physics: Conference Series*. 2015, vol. 655, p. 012057. ISSN 1742-6596. Available from DOI: `10.1088/1742-6596/655/1/012057`.

Symbols and abbreviations

KEPCO	Korea Electric Power Corporation
KNF	KEPCO Nuclear Fuel
LWR	Canada Deuterium Uranium
LWR	Light Water Reactor
MOX	Mixed Oxide fuel
LWR	Pressurised Water Reactor
ZIRLO	Zirconium Low Oxide
US NRC	United States Nuclear Regulatory Commission
LOCA	Loss Of Coolant Accident
RIA	Reactivity Initiated Accident
RCS	Reactor Coolant System
RPV	Reactor Pressure Vessel
PCI	Pellet Cladding Interaction
SCC	Stress Corrosion Cracking
SPS	Spark Plasma Sintering
LWR	Boiling Water Reactor
ATF	Accident Tolerant Fuel, Advanced Technology Fuel
ORNL	Oak Ridge National Laboratory
CVD	Chemical Vapour Deposition
CVI	Chemical Vapour Infiltration
KAERI	Korea Atomic Energy Research Institute
SEM	Scanning Electron Microscopy
DEC	Design Extension Consitions
CA-PVD	Cathodic Arc Physical Vapour Deposition

RIS	Radiation Induced Segregation
HEA	High Entropy Alloys
FEEC BUT	Faculty of Electrical Engineering and Communication, Brno University of Technology
HEA	In-containment Refuelling Water Storage Tank
TG	Turbine Generator
SG	Steam Generator
RCP	Reactor Coolant Pump
CEA	Control Element Assembly
PPS	Plant Protection System
SIS	Safety Injection System
SIT	Safety Injection Tank
SCS	Shutdown Cooling System
SDVS	Safety Depressurisation and Vent System
POSRV	Pilot-operated Safety Relief Valve
AFWS	Auxiliary Feedwater System
DC	Direct Current
DBA	Design Basis Accident
HMS	Hydrogen Management System
PAR	Passive Autocatalytic Recombiner
NPP	Nuclear Power Plant
BDBE	Beyond Design Basis Event
SA	Severe Accident
LB LOCA	Large Break Loss of Coolant Accident
FLEX	Flexible and Diverse Coping Strategies

ESF	Engineered Safety Features
PCT	Peak Cladding Temperature
ECC	Emergency Core Coolant
DVI	Direct Vessel Injection
SBO	Station Black-out
LOOP	Loss of Offsite Power
EDG	Emergency Diesel Generators
AC	Alternating Current
AAC	Alternative Alternating Current power sources
SAMG	Severe Accident Management Guidelines
DSA	Deterministic Safety Analysis
AOO	Anticipated Operational Occurrences
ALARA	As Low As Reasonably Achievable principle
DNBR	Departure from Nucleate Boiling Ratio
PRA	Probabilistic Risk Analysis
MCCI	Molten Corium Concrete Interaction
UHS	Ultimate Heat Sink
CV	Control Volume
FL	Flow Path
MP	Material Package
COR	CORE Package
CF	Control Function
TF	Tabular Function
NIST	National Institute of Standards and Technology
SIP	Safety Injection Pump

k	Thermal conductivity (W/m.K)
x	Deviation from stoichiometric coefficient (-)
T	Temperature (K)
ρ	Density (kg/m^{-3})
c_p	Specific heat capacity (J/kg.K)
α	Coefficient of thermal expansion (10^{-6}/K)
DPA	Displacement per atom (-)
$x_{CL,CELL}$	Weight of cladding in cell multiplier (-)
W	Mass of metal oxidised per unit surface area
$k_{p,H2O}$	Pre-exponential factor for water/steam containing environment in (kg^{2}.m^{-4}.s^{-1})
E_a	Activation energy for reaction to occur (J.mol^{-1}.K^{-1})
R	Molar gas constant (J.mol^{-1}.K^{-1})
QOX	Heat of reaction (kJ.mol^{-1})(J.kg^{-1})
ΔH^0	Standart enthalpy of formation (kJ.mol^{-1})
M	Molar weight (g.mol^{-1})
ϕ	Weight percentage (%)
H	Enthalpy (J.kg^{-1})
LHF	Latent heat of fusion (J.kg^{-1})
δ	Cladding thickness (mm)
S_{FP}	Fuel pellet cross-sectional area (mm^{2})
r_{FP}	Fuel pellet radius (mm)
$S_{FP,surface}$	Fuel pellet surface area (mm^{2})
l	Fuel rod length (mm)
S_{CL}	Cladding cross-sectional area (mm^{2})

r_{CL}	Cladding inner radius (mm)
R_{CL}	Cladding outer radius (mm)
x_{FU}	Weight of fuel multiplier (-)
m_{FU}	Weight of fuel (kg)
ρ_{FU}	Density of fuel (kg.m^{-3})
V_{FU}	Volume of fuel (m^{3})
$x_{FU,surface}$	Fuel surface area multiplier (-)
x_{CL}	Weight of cladding multiplier (-)
m_{CL}	Weight of cladding (kg)
ρ_{CL}	Density of cladding (kg.m^{-3})
V_{CL}	Volume of cladding (m^{3})